

Design and Optimization of an MHD Energy Harvester for Intelligent Pipe Systems

by

Xiaotong Zhang

Submitted to the Department of Mechanical Engineering
in partial fulfillment of the requirements for the degree of

Master of Science in Mechanical Engineering

at the

MASSACHUSETTS INSTITUTE OF TECHNOLOGY

June 2019

© Massachusetts Institute of Technology 2019. All rights reserved.

Signature redacted

Author
.....

Department of Mechanical Engineering
May 17, 2019

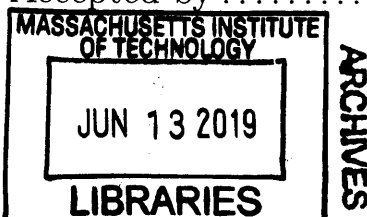
Signature redacted

Certified by
.....

Kamal Youcef-Toumi
Professor
Thesis Supervisor

Signature redacted

Accepted by
.....



Nicolas Hadjiconstantinou
Chairman, Committee on Graduate Students

Design and Optimization of an MHD Energy Harvester for Intelligent Pipe Systems

by

Xiaotong Zhang

Submitted to the Department of Mechanical Engineering
on May 17, 2019, in partial fulfillment of the
requirements for the degree of
Master of Science in Mechanical Engineering

Abstract

In this thesis, an innovative Magnetohydrodynamic (MHD) energy harvester with the use of the magnetic concentrator is designed and optimized. A theoretical model relating the conductivity of water, magnetic flux density B , flow velocity u and the channel volume to the power output is first established. This leads to the decoupled analysis and simulations of magnetic field and flow field. The prototyped energy harvester without the concentrator achieves a power output of 442 nW, while the power output of the final design with the concentrator is expected to be 718.5 nW. The concept of another MHD energy harvester with a spiral flow diverter is also established with hollow space in the middle of the energy harvester for flow and robots to pass through. It is validated by CFD simulations that the flow velocity in the channel surrounding the hollow area is greatly amplified with the spiral flow diverter. The MHD energy harvester with the concentrators and spiral flow diverter is expected to produce power output of 238.3 nW.

Thesis Supervisor: Kamal Youcef-Toumi

Title: Professor

Acknowledgments

First of all, I would like to thank my advisor Prof. Kamal Youcef-Toumi for his guidance and support through my two-year study at MIT. Without his help and guidance, my successful transition from my undergraduate focus Computational Fluid Dynamics to mechatronics and robotics would not have been possible. The spirits of persistence and seeking the truth he conveyed are also great treasures for my career and professional development.

I also would like to thank Dr. You Wu, Steven Yip Fun Yeung, Tyler Takeo Okamoto, and Elizabeth R Mittmann, who work together with me in the same project and offer me valuable advice and assistance. I am also thankful to the other members of the MIT Mechatronics Research Laboratory. They are great engineers and researchers. I learned a lot of knowledge and obtained some fabulous inspiration from discussions with them.

I am also thankful to MathEarth Inc., who sponsors the project kindly. The staffs there, including Dr. Haoping Yang and Mr. Honghai Bi, provide deep industrial insights and experiment supports, which are significant for the results in this thesis and are also gratefully appreciated.

Last but not least, I must sincerely and especially thank my parents, Mr. Hongda Zhang and Ms. Fenghua Zhu, for their constant encouragement and support from China. And I am also thankful to all my friends, who accompany me and make my life fun every day.

Contents

1	Introduction	17
1.1	Background and Motivations	17
1.2	Previous Studies on Smart Pipe Systems	18
1.3	Previous Studies on Energy Harvesting	19
1.3.1	Turbine	19
1.3.2	Direct electromagnetic induction	20
1.3.3	Piezoelectric effect	20
1.3.4	Magnetohydrodynamics	21
1.4	Contribution and Thesis Outline	22
2	MHD Energy Harvester Modelling	25
2.1	Generalized Ohm's Law	26
2.2	Power Extracted	26
2.3	Power Generated	27
2.4	Hall Effect	28
2.5	Discussion	30
2.6	Summary	31
3	Magnetic Field Analysis and Optimization	33
3.1	Problem Description	33
3.2	Magnet Layout Design	34
3.2.1	Theoretical modeling	34
3.2.2	Three-layer magnet layout design	36

3.2.3	Simulation setup	36
3.2.4	Simulation results	37
3.3	Magnetic Concentrator	38
3.3.1	Concentrator design	39
3.3.2	Validation and parameter study	39
3.4	Summary	49
4	Flow Field Analysis and Optimization	51
4.1	Problem Description and Assumption	51
4.2	CFD Model and Setup	53
4.3	CFD Results and Analysis	54
4.3.1	Simulation with square channels	54
4.3.2	Simulation with various channel widths	57
4.4	Other Concerns	58
4.4.1	Channel entrance and exit geometry	60
4.4.2	Surface friction	60
4.5	Summary	62
5	The Optimized Design and Experiments	63
5.1	Summary of the Analysis	63
5.2	Final Design	64
5.3	Fabrication	66
5.4	Experimental Setup	66
5.5	Experimental Results	69
5.6	Discussion	70
5.7	New Concept with a Spiral Flow Diverter	72
5.7.1	Problem description	72
5.7.2	Design of the spiral flow diverter	73
5.7.3	Validation of the design	74
5.8	Summary	78

6 Conclusion and Recommendations	79
6.1 Conclusion	79
6.2 Recommendations	80
A Effect of the Inner Concentrator	81
A.1 Relevant Parameters	81
A.2 Simulation setup	82
A.3 Simulation results and discussions	84
A.4 Summary	90
B Concept and Validation of the New Microchannel Detector	93
B.1 Previous Methods for Pipe Leak Detection	93
B.1.1 Acoustics Sensing	94
B.1.2 Pressure Gradient Sensing	95
B.1.3 Some Other Methods	95
B.2 Problem Description	96
B.3 Theoretical Analysis	97
B.4 Numerical Simulation and Validation	98
B.4.1 Concept validation	99
B.4.2 Gap between the channel and the wall	100
B.4.3 Channel size	101
B.4.4 Relative position of the channel	101
B.4.5 Orientation angle of the channel	104
B.4.6 Overset moving part simulation	104
B.5 Conceptual Design	107
B.6 Problems of the Design	109
B.7 Summary	109
C Materials and Components	111
C.1 Conductive Coating	111
C.2 Smooth-on XTC-3D Coating	113

List of Figures

2-1	Schematic of a simplified MHD energy harvester.	25
3-1	The relationship between the averaged B within the channel and the distance between two magnets with $d = 0.002m$, and unit $m = 1A \cdot m^2$.	35
3-2	Magnetic flux induced by two strong Neodymium magnets.	37
3-3	Magnetic flux with an additional three-layer magnet structure.	38
3-4	Front view of the concentrator design.	40
3-5	Demagnetization curve for N42 grade Neodymium magnets.	41
3-6	Magnetic flux vector plot. (a) only magnets; (b) magnets and inner concentrator; (c) magnets, inner concentrator, and loop with width $w=0.005$ m.	41
3-7	Contour of magnetic flux density in y-direction. (a) only magnets; (b) magnets and inner concentrator; (c) magnets, inner concentrator, and loop with width $w=0.005$ m.	42
3-8	B-H curve of mu-metal and Metglas. (a) overview; (b) detailed view.	43
3-9	Contour of magnetic flux density in y-direction. (a) metglas; (b) mu-metal.	44
3-10	Magnetic flux vector plot. (a) metglas; (b) mu-metal.	44
3-11	Contour of magnetic flux density magnitude. (a) metglas; (b) mu-metal.	45
3-12	Average B_y in the channel with various loop widths.	46
3-13	Magnetic flux density contour for the cases with loop size of (a) 0.002 m; (b) 0.015 m.	46
3-14	Average B_y in the channel with and without two big magnets outside.	48

3-15 Magnetic flux vector with and without two big magnets outside.	48
4-1 Working curve of a typical centrifugal pump.	52
4-2 Computational region schematic and mesh.	54
4-3 The contour of u_x in the case with 7 mm channel and 10,000 pa inlet pressure on the slice $z=0$	55
4-4 Static pressure contour in the case with 7 mm channel and 10,000 pa inlet pressure on the slice $z=0$	56
4-5 Force acting on the energy harvester in the x-direction.	56
4-6 Averaged u_x within the channel.	57
4-7 Contour of u_x with fixed $h=7$ mm and 20,000 Pa inlet pressur inlet. (a) $b=30$ mm, (b) $b=25$ mm, (c) $b=20$ mm, (d) $b=15$ mm, (e) $b= 10$ mm, (f) $b=5$ mm.	59
4-8 Averaged u_x within the channel with various channel width b	60
4-9 Moody chart for pipes covered with sands.	61
5-1 Final design. (a) overall view; (b) side view; (c) front view; (d) magnets and concentrators.	64
5-2 Material test of the conductive coating.	65
5-3 Fabrication of components and assembled prototype.	67
5-4 Experimental setup. (a) top view of the tank, pump and test segment; (b) front view of the tank, pump and test segment; (c) flow meter 2 m after the pipe elbow.	68
5-5 Experimental and theoretical power output with various load resistance.	70
5-6 Preliminary design of the energy harvester with a hollow area in the center.	73
5-7 Design of the spiral flow diverter and cross section of the turbulence inducer.	74
5-8 Mesh for spiral flow diverter case. (a) overview; (b) zoom-in view on slice of $y=0$ m (middle plane).	75

5-9 Pressure contour at $x=0.39$ m from the energy harvester inlet for the case (a) with spiral flow diverter; (b) without spiral flow diverter.	75
5-10 Streamline for the case (a) without spiral flow diverter; (b) with spiral flow diverter.	76
5-11 Velocity contour at the slice $x=0.39$ m from the energy harvester inlet for the case (a) with spiral flow diverter; (b) without spiral flow diverter.	76
5-12 Velocity contour at the slice $y=0$ m (middle plane) for the case (a) with spiral flow diverter; (b) without spiral flow diverter.	77
A-1 Concentrator geometry and parameters.	82
A-2 B-H curve of the metarial.	83
A-3 Demagnetization curve for N42 grade Neodymium magnets.	83
A-4 Contour of B magnitude. (a) mu-metal concentrator; (b) without concentrator (material in the trapezoidal concentrator region assigned as air).	84
A-5 Contour of directional B. (a) mu-metal concentrator; (b) without concentrator (material in the trapezoidal concentrator region assigned as air).	85
A-6 Averaged B_y in the channel with the concentrator of (a) mu-metal with 2 mm height; (b) mu-metal with 8.5 mm height; (c) permalloy with 2 mm height; (d) permalloy with 8.5 mm height; (e) annealed pure iron with 2 mm height; (f) annealed pure iron with 8.5 mm height.	86
A-7 Difference of averaged B_y between mu-metal and (a) permalloy with 2 mm height; (b) annealed pure iron with 2 mm height; (c) permalloy with 8.5 mm height; (d) annealed pure iron with 8.5 mm height.	88
A-8 Max averaged B_y for concentrators with height of (a) 2 mm; (b) 8.5 mm.	89
A-9 Difference of averaged B_y between 2 mm and 8.5 mm height concentrators.	89
A-10 Averaged B_y for 2 mm height concentrator with mu-metal.	90
A-11 Max B_y with various channel widths.	90

B-1	Working principle and prototype of previously designed leak detection robot.	96
B-2	Simulation setup. (a) geometry setup. (b) mesh setup and refinement. (c) geometry zoom-in at the leak and the channel.	98
B-3	Simulation result for validation. (a) streamline without channel. (b) streamline with channel. (c) pressure contour without channel. (d) pressure contour with channel. (e) pressure distribution along the center line of the channel. (f) velocity distribution along the center line of the channel.	99
B-4	4 mm channel simulation result with various gaps. (a) no gap. (b) 1 mm gap. (c) 2 mm gap. (d) pressure distribution on the center lines of the channels.	100
B-5	2 mm and 8 mm channel simulation result with various gaps. (a) 2 mm channel no gap . (b) 2 mm channel with 1 mm gap. (c) 2 mm channel with 2 mm gap. (d)8 mm channel with no gap. (e) 8 mm channel with 1 mm gap. (f) 8 mm channel with 2 mm gap.	102
B-6	1 mm gap simulation result with various channel sizes of (a) 2 mm channel; (b) 4 mm channel; (c) 8 mm channel size; (d) 16 mm channel size. (e)plot of the pressure on center line.	103
B-7	Simulation results of cases with a 8 mm leak and 2 mm channel at different position of (a) 1/4 of the leak; (b) 2/4 of the leak; (c) 3/4 of the leak; (d) 4/4 of the leak.	104
B-8	Simulation results of cases with a 8 mm leak and 2 mm channel skewing 45° to the right at different position of (a) 1/4 of the leak; (b) 2/4 of the leak; (c) 3/4 of the leak; (d) 4/4 of the leak.	105
B-9	Working Principle of the Overset Mesh Method.	106
B-10	Simulation results of moving channels using Overset Mesh Method. .	106
B-11	Proposed conceptual design.	107
B-12	Simulation validation of the design	108

List of Tables

3.1	Permeability of typical materials.	39
3.2	Simulation results for effect validation.	42
C.1	Properties of the silver conductive coating material.	111
C.2	Properties of the nickel conductive coating material.	112
C.3	Properties of the carbon conductive coating material.	112
C.4	Properties of the Smooth-on XTC-3D coating material.	113

Chapter 1

Introduction

Sufficient and sanitary water supply is crucial for life, industrial production and economic development. But a huge amount of water is wasted due to leak every day around the world. Although some technologies have been developed to alleviate this problem, there's still a long way to achieve a much more sustainable, environmentally friendly, and resource conservative water distribution system. And this system can be a significant part or a good start point of a smart city, monitoring the working condition of assets with IoT (Internet of Things) sensors and data transmission.

1.1 Background and Motivations

20% of water in the distributing pipe system is wasted every day around the world due to underground leaks, which are even hard to find [1]. The problem in developing countries are even worse. In 2016, it was reported by the World Bank that about 45 million cubic meters of water are lost daily in developing countries, which is worth an economic value of over 3 billion USD per year [2]. On the other hand, those countries need to face tremendous water demand brought by the large-scale population and widespread heavy industry. Besides water resource loss, the pipe leaks might also cause severe damage to private properties and public infrastructures, which is estimated to cost billions of dollars within the US [3].

Facing such severe consequences, smart pipe systems are proposed to be good

possible solutions to settle the problems by realizing real-time monitoring or even prognostics of the pipe working condition. And the water quality can even be monitored. The smart pipe systems not only can conserve water resource for the earth, but also means dramatically reduced economic loss and more profit for the water authorities. Thus great interest in this area has been aroused in the past few years.

Such a system can be composed by several components, including sensors, data transmission, working condition recognition, system failure alarm, and energy harvesting. And the energy harvesting component can be the bottleneck for most of such systems since it is sophisticated to supply power for the sensors widely spread everywhere under the ground around the cities with conventional methods, like batteries or wires. And those methods also demand a lot of manpower to maintain. Thus a device to harvest energy from environment continuously for a long time, and providing power for the sensor, is desired. And it attracts more and more focus and attention from both academia and industry.

Thus, in this thesis, we will focus on the design and performance optimization of an energy harvester extracting power from the water flow and providing power for leak detection sensors along the instrumented pipes.

1.2 Previous Studies on Smart Pipe Systems

The working principles and characteristics of sensors detecting leaks based on acoustics, pressure gradient, Ground Penetrating Radar, fiber optic sensing, and force sensitive resistors are discussed in Section B.1. The development of these sensors and the algorithm to process their data makes it feasible to realize real-time monitoring in practice.

And then, a bigger goal is raised for such systems to achieve monitoring with ultra-low power consumption. It is found that most asset failure takes days, weeks, or even months to happen. Thus it is useless to monitor and run all the functions continuously all the time [4]. It is calculated that a continuous monitoring system (including ZigBee communication, sensors, and local microprocessors) can consume

power as low as 20 mW for one node, and if the system only works 100 ms per day, it will give a power requirement of only 20 nW [5]. In 2014, based on this idea, a novel sensor using force sensitive resistors is developed by Ali M. Sadeghioon, Nicole Metje, David N. Chapman and Carl J. Anthony from University of Birmingham. After converting the flow pressure into strain of the pipe, the sensor measures the flow pressure fluctuation every 6 hours with a minimal $2.2 \mu\text{W}$ power consumption. And the pressure information can also be used to locate the leaks [6]. This work validated the feasibility to monitor the pipe working condition with a low-frequency sampling. And it also promises the practical use of the energy harvester developed in this thesis in real scenario. With the advancement of MEMs and researches on the ultra-low power consumption sensors, this power requirement can be even lower in the future and the sacrifice on the sample rate can be eliminated.

The existence of these sensors provides a lot of space for novel energy harvester design that may be trivial in the past.

1.3 Previous Studies on Energy Harvesting

The energy source of the sensors used are batteries. But the cost to replace the underground batteries at a regular schedule is unaffordable for most water companies, which forces the research related to energy harvesters converting the flow kinetic energy to electrical energy. These previous researches can be sorted out into four categories based on the working principles.

1.3.1 Turbine

The first kind of energy harvesters implements conventional water turbines or impeller wheels. The turbines can convert the directional velocity of the flow to rotational motion of the turbine. And this rotational motion will result in the relative motion between the magnets and coils, which can be seen as the prerequisite of electromagnetic induction.

This method usually produces a large amount of power, far beyond the require-

ment of a sensor node. But this methods can also face some disadvantages. Firstly, the turbines rotate all the times, which means regular maintenance is inevitable. This may not be a problem for wind turbine or dam turbine which works above ground, but is extremely difficult for underground pipe systems. Secondly, the turbine blades can be damaged by the sudden pressure fluctuation within the pipeline or foreign objects moving together with flow. Thirdly, it can also bring in vibrations, causing rapid fatigue on pipe structure or unacceptable noise to the sensing data [7, 8].

1.3.2 Direct electromagnetic induction

The second category of energy harvesters for wireless sensor networks adopts direct electromagnetic induction principle by driving permanent magnets or coils to vibrate among or next to coils or permanent magnets. The vibrations can come from the locomotion of vehicles or humans, or the pressure ripple within pipe flow. The power output is usually optimized by tuning spring constant and mass to harmonic [9, 10, 11]. A good design can usually achieve tens or hundreds of microwatts only on one PCB board.

But these methods also introduce extra vibrations into the system. And the device after deployment only corresponds to one optimal vibrational frequency, which greatly limits the range of flow velocity and pressure within the pipeline.

1.3.3 Piezoelectric effect

Piezoelectric effect is the phenomenon and ability of some materials that electric charges can be generated on the material surface in response to mechanical stress. To extract the charges continuously, vibrational motion is usually loaded on the material. And then positive and negative charges are generated on the surface alternately, which can produce alternating current out from the materials.

The vibration can come from a wide source, including human stepping on shoes or vehicle locomotion. When used in pipe systems, it can also come from the dynamic pressure ripple or the artificial vibration induced by specially designed fluid-structure

interaction and asymmetrical vortex shedding. Using the pressure ripples, a piezoelectric material stack together with its housing, which can be mounted on the pipe, is already designed and prototyped. And this prototype finally achieves a 1.2 mW max power output [12]. As for the source of the induced vibration, an energy harvesting eel, composed of flexible piezoelectric membrane PVDF and a bluff body acting as the excitation of the Karman vortex street, is proposed in 2001 [13, 14]. But the eel has not been prototyped, and thus there's no experimental demonstration of the concept.

This method can also introduce vibrations to the structure and noise to the data recorded by sensors. Moreover, since the vibrational frequency of the wake behind the bluff body is regulated by Strouhal number and flow velocity, the tuning of design parameters also highly depends on the flow velocity, which means one device can only work best for one specific velocity and the power output may be trivial under other velocities. However, it is hard to set the flow velocity fixed as most water distribution systems have peak and valley time. Also, design with piezoelectric material also needs to deal with off-resonance, as the pressure fluctuation frequency is usually much smaller than the fundamental resonance of the piezoelectric material.

1.3.4 Magnetohydrodynamics

No matter which concept is adopted to harvest energy, the basic principle is that moving charged particles, in the presence of magnetic field, experience a force in the direction perpendicular to both magnetic flux density B and the charge velocity u . One way that is more direct to produce electricity than the above three methods is to induce electric field by the fact that positive and negative charges tend to move in opposite directions in the influence of B field, which is referred to as MHD (Magneto hydro dynamics) effect.

This phenomenon is first observed by Faraday in 1831, when he placed two large electrodes in the Thames river and connected them to a galvanometer. The conducting water flowed between electrodes and through earth's magnetic field. An irregular and small signal is observed [15]. Years later, the same principle started to be used in

large power plants, but with stronger magnetic field and highly conductive conductors. In 1961, a liquid fossil fuel “seed” with a potassium compound was utilized and the equipment successfully achieved power levels more than 10 kW [16]. After that, MHD power generators have been widely studied, and the MHD/Steam binary cycle power plant can even reach an efficiency of 60% [17].

Conversely, MHD principle can also be used for ship propulsion in seawater with high conductivity and salinity [18]. In 2000, a one-ton ship model in China is propelled by MHD propulsion to a speed of 0.61-0.68 m/s [19].

However, large power output or propulsion force usually requires superconducting coils to provide stronger B and conductors with high conductivity, such as plasma or sea water. These two factors both limit the use of MHD. However, with the advancement of electronic engineering and leak detection algorithm, the power demand for each sensor node on smart pipes can achieve as low as $2.2 \mu\text{W}$ [6], which makes MHD power generation for wireless sensor networks feasible after careful design and optimization.

There are no moving parts in a working MHD energy harvester except for the conductors, and the power output does not depend on the flow condition in frequency domain. These two characteristics overcome the shortcomings of the above three methods of frequent maintenance, additional vibrations, off-resonance of piezoelectric material, and high dependence on the vibrational frequency. Thus MHD shows a great potential in energy harvesting than other methods in the applications where high reliability and automatic adaptation to different flow conditions are desired.

1.4 Contribution and Thesis Outline

In this thesis, a novel MHD energy harvester working with tape water and permanent magnets in room temperature is proposed, prototyped, and tested. And this is the first ever prototyped and tested MHD energy harvester for smart sensor networks, to the best of our knowledge.

To increase the magnetic field and the power output, a three-layer magnet struc-

ture and magnetic concentrators with high permeability are added in the design. A methodology to optimize the overall performance of such an energy harvester under different pipe sizes and flow condition is also proposed and validated.

Moreover, a new concept design is also proposed. In this design, the energy harvester has a hollow area at its center to allow the flow and robots to go through without any interruption. And the flow diverter used in this concept design can also be used in other applications, where flow needs to be diverted from its original flow pattern.

The thesis starts from the theoretical model governing the MHD phenomenon in Chapter 2. And it is found that the power output is proportional to the square of both the magnetic flux density and the flow velocity. Based on this, magnetic field and flow field are optimized in Chapter 3 and 4 using theoretical analysis and numerical simulations. In Chapter 5, an MHD energy harvester with the novel design after optimization is proposed. And its simplified version is prototyped, and tested in the experimental setup built at MRL. Methods to further improve the results from the prototype in practical use are analyzed and suggested using the model established in Chapter 2. The new flow diverter and the energy harvester with hollow center are also described and analyzed in Chapter 5.

Chapter 2

MHD Energy Harvester Modelling

MHD is the macroscopic behavior of Lorentz force acting on charged particles. Even in ultrapure water, the existence of the self-ionization balance reducing water molecules into hydroxide ions and hydrogen ions results in a conductivity about $0.055 \mu\text{S}/\text{cm}$. Daily tap water can even reach a conductivity of $50\text{-}800 \mu\text{S}/\text{cm}$ due to impurities.

A simplified Faraday energy harvester is shown in Figure 2-1, with two electrodes perpendicular to the z-axis, conductor flowing in the x-direction, and B in $-y$ -direction. The geometric parameters illustrated in the figure are also used in the following system modelling and analysis.

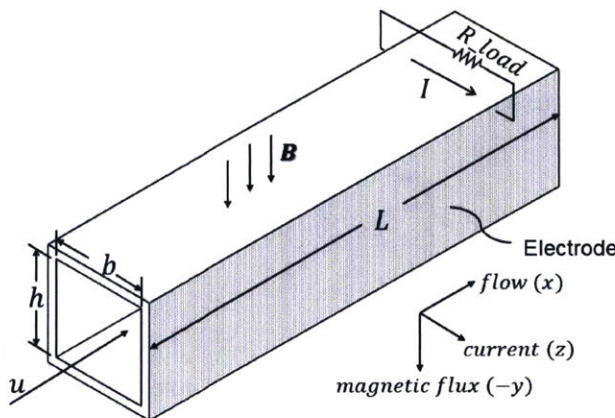


Figure 2-1: Schematic of a simplified MHD energy harvester.

2.1 Generalized Ohm's Law

Under the assumption that Hall effect of the induced current is neglected, the induced current density vector can be described using the generalized Ohm's law as in Equation (2.1), that

$$\mathbf{J} = \sigma(\mathbf{E} + \mathbf{u} \times \mathbf{B}) \quad (2.1)$$

where σ (S/m) is the conductivity, \mathbf{J} (A/m²) is the current density vector, \mathbf{E} (V/m) is the electric field intensity, \mathbf{u} (m/s) is the velocity of the conductor, and \mathbf{B} (Wb/m²) is the magnetic flux density vector. The term $\mathbf{u} \times \mathbf{B}$ represents the additional Lorentz force in the direction perpendicular to both \mathbf{u} and \mathbf{B} , or the additional induced electric field in the fixed coordinate system after coordinate transformation from the moving coordinate system. And the term \mathbf{E} comes from the potential difference between the two electrodes. In our following discussion, we will assume that all the parameters are uniform and their values are averaged among the region.

In this particular problem, the current density in the z-direction, which can be collected by electrodes, can be deduced to a scalar expression in Equation (2.2).

$$J_z = \sigma(E_z - uB) \quad (2.2)$$

where subscript z represents the component in the z-direction of a vector. Thus the open circuit electric field should be uB for open circuit, where $J_z = 0$. While for the short circuit circumstance $E_z = 0$, the short circuit current density should be $-\sigma uB$.

2.2 Power Extracted

The geometric parameters of a conductor channel are shown in Figure 2-1. h and b represents the height and width of the channel respectively, and L is the length of electrodes in the direction of flow.

The harvester can not work when the circuit is open or short. Thus a load re-

sistor R_{load} is installed in the circuit to extract power out of the generator. With simple manipulation, the total power output can be deduced by using $I = J_z \cdot h \cdot L$ (conservation of charge), and $V_z = E_z \cdot b = I(R_{load} + R_i)$ (definition of electric field and Ohm's law for external circuit), where R_i is the internal resistance, and I and V_z are the current and voltage output from the generator. Then the current output and power extracted by the load resistor can be derived in Equation (2.3) and Equation (2.4).

$$I = \frac{\sigma h L b u B}{2b + \sigma h L R_{load}} \quad (2.3)$$

$$P_{out} = \left[\frac{\sigma h L b u B}{2b + \sigma h L R_{load}} \right]^2 R_{load} \quad (2.4)$$

with a maximized power output expressed by (2.5)

$$P_{max} = \sigma \frac{bhL}{8} u^2 B^2 \quad (2.5)$$

when

$$R_{load} = \frac{2b}{\sigma h L} \quad (2.6)$$

And it also should be noticed that the power extracted is proportional to the channel volume. This allows the power output to be magnified in real scenario where the sizes of pipes and harvesters are way bigger than the ones in the lab. But this also increases the difficulty to balance all the parameters, since large volume may result in a smaller B.

2.3 Power Generated

The power extracted is different from the power that is generated in the whole system. Due to the existence of the internal resistance, there must be parts of the power dissipated. And in this case, the current and the power generated can be deduced as

in the Equation (2.7) an Equation (2.8)

$$I = \frac{\sigma h L b u B}{2b + \sigma h L R_{load}} \quad (2.7)$$

$$P_{gen} = \left[\frac{\sigma h L b u B}{2b + \sigma h L R_{load}} \right]^2 (R_{load} + R_i) \quad (2.8)$$

where R_i is the internal resistance, which can be written as

$$R_i = \frac{1}{\sigma} \frac{b}{hL} \quad (2.9)$$

And then the maximized power generated can be derived and expressed by Equation (2.10)

$$P_{maxgen} = \sigma \frac{bhL}{4} u^2 B^2 \quad (2.10)$$

when

$$R_{load} = 0 \quad (2.11)$$

The max power generated by the harvester is double of the max power extracted by the load resistors. But the problem to use power generated as the result parameter is that this parameter is hard to be measured and thus compared with the theoretical model. And the power consumed by the internal resistance is useless for practical use. Thus the power extracted in Section 2.2 will be the parameter we focus on and optimized in the following chapters.

2.4 Hall Effect

Another factor which may influence the result is the hall effect caused by the induced current in the direction of z-axis. This hall effect can cause another induced current in the direction of x-axis, which can reduce the flow velocity. After considering this effect, the current density in z-direction can be deduced to be

$$J_z = \frac{\sigma}{1 + \beta^2} (E_z - uB + \beta E_x) \quad (2.12)$$

$$J_x = \frac{\sigma}{1 + \beta^2} (E_x - \beta(E_z - uB)) \quad (2.13)$$

And then the max power output can be calculated as

$$P_{maxout} = \frac{\sigma b h L u^2 B^2}{8 + 4\beta^2} \quad (2.14)$$

where β is the hall parameter of the conductor flow defined as

$$\beta = \frac{eB}{m_e \nu} \quad (2.15)$$

where e is the atomic unit of charge; m_e is the electron mass; ν is the collision frequency within the conductor.

The existence of the hall effect makes a change in the expression of the current and the power output. And it has to be considered in conventional MHD power generator working with “seeded” plasma, as the hall parameter in plasma can easily reach to 6 or 7.

However, in our design and optimization analysis with the conductor of water, this effect is neglected, and Equation (2.5) and (2.6) are adopted according to the following two reasons:

1) The hall effect for water is not so observable. In other words, the hall parameter for water is very low.

2) Hall effect can be eliminated if the electrodes are segmented into pieces. In this case, the electrodes in x-direction are taken as open, and thus $J_x = 0$. And then it is derived that

$$E_x = \beta(E_z - uB) \quad (2.16)$$

If the Equation (2.16) is substituted into Equation (2.12), the current density in z-direction will turn out to be the one in Equation (2.2) without hall effect. Thus, it is

proved that the utilization of segmented electrodes will greatly eliminate this effect, although this kind of electrodes is not prototyped in this thesis due to fabrication limitation.

2.5 Discussion

Equation (2.5) shows that the result can be decoupled into velocity field u and magnetic flux density field B , which both have a quadratic contribution on the power output. Thus, the power output can be dramatically magnified if B and u are optimized. And the optimal load resistor can be determined with Equation (2.6). However, since the smart pipe system will deliver water for drinking and other daily use, it is very difficult to add seeds to increase water conductivity, like what other MHD power generators do. Thus, only u , B , and the channel geometry can be played with and optimized.

We can further represent u in the channel in Equation (2.5) with far-field velocity u_0 and far-field cross-sectional area A_0 , using mass conservation $A_0 u_0 = ubh$, and get Equation (2.17)

$$P_{max} = \frac{\sigma A_0^2 u_0^2}{8} \frac{L}{bh} B^2 \quad (2.17)$$

which means that smaller b , smaller h , and longer L will maximize the power output under the assumption that the flow is incompressible and the geometry doesn't influence far-field flow velocity. However, the second assumption is not always true as most pumps provide pressure, and the same far-field velocity u_0 is hard to maintain with high block aspect ratio and smaller size channel according to Poiseuille's law. In this case, theoretical analysis and CFD (Computational Fluid Dynamics) simulation with the controlled same inlet pressure is performed and discussed in the following chapter.

2.6 Summary

In this chapter, generalized Ohm's law is adopted first to describe the macroscopic behavior of the charged particles within water and the phenomenon of MHD. Based on that, the power that can be extracted by external resistors are deduced and it is found that B and u are two decoupled fields which both have a second order contribution on the power. Thus B and u are two fields to be specially analyzed and optimized in the following chapters. And it is also noticed that the power generated is proportional to the channel volume, which can't be ignored.

Hall effect of the induced current is also discussed. But this effect is not necessary to be taken into consideration at this stage since the hall effect of water is not very observable and it can be eliminated by segmented electrodes in the future.

Chapter 3

Magnetic Field Analysis and Optimization

Based on the analysis in the above chapter, magnetic field B must be carefully discussed and analyzed, since it can cause a significant difference in the power output.

3.1 Problem Description

To get the optimal B , key factors influencing B should be analyzed with both theoretical and simulational methods. And some special designs, like magnetic concentrators, can also be assembled in the design to achieve an overall best optimization.

The magnetic field B is first built by two N52 degree Neodymium magnets with the size of $0.0762 \text{ m} \times 0.0762 \text{ m} \times 0.0127 \text{ m}$ (3 inches \times 3 inches \times 0.5 inches), placing out of the pipe, which is the simplest magnet layout. Both magnets are very strong with a residual induction of 14,800 Gauss and a max surface induction of 2,125 Gauss when measured with a Gauss meter. The problem is that although the magnets are strong enough, the magnetic induction within the pipe is still measured to be small. The reason and solution to this problem should be discussed and proposed.

Moreover, a magnetic concentrator made of some materials with high magnetic permeability is commonly used in the design of transformers or sensors to concentrate or guide the magnetic flux, and thus to achieve a lower power dissipation or noise

level. But several factors, including the shape and the material of the concentrator, and the size of the flow channel, can all influence the effect. Thus a careful and systematical analysis of these parameters should be carried out.

3.2 Magnet Layout Design

In this section, a better design of magnet layout is proposed and validated after theoretical analysis and simulations.

3.2.1 Theoretical modeling

The theoretical modeling part is to model the magnetic field distribution amongst the channel and the whole space. Since the relative permeability of air, water, and PVC is very close to 1, all the materials, except for the magnets, are treated as vacuum with a relative permeability of 1.

According to the Gilbert model, a magnet can be modeled by a magnetic dipole, whose two poles are the magnetic sources with the same magnitude, but opposite signs. The magnetic vector potential in vacuum and the induced magnetic induction can be expressed by Equation (3.1) and (3.2) in polar coordinates.

$$\mathbf{A}(\mathbf{r}) = \frac{\mu_0}{2\pi r^2} \frac{\mathbf{m} \times \mathbf{r}}{r} = \frac{\mu_0}{4\pi} \frac{\mathbf{m} \times \mathbf{r}}{r^3} \quad (3.1)$$

$$\mathbf{B}(\mathbf{r}) = \nabla \times \mathbf{A} = \frac{\mu_0}{4\pi} \left(\frac{3\mathbf{r}(\mathbf{m} \cdot \mathbf{r})}{r^5} - \frac{\mathbf{m}}{r^3} \right) \quad (3.2)$$

where \mathbf{A} is the magnetic vector potential, \mathbf{B} is the magnetic flux density, \mathbf{m} is the magnetic moment, \mathbf{r} is the displacement vector of a point in the space relative to the dipole, and μ_0 is the vacuum permeability constant. To further simplify the model for our analysis, we assume that the size of the magnets is much larger than the flow channel. The B at the same height is represented by the value of B on the center line connecting two magnets, which is shown in Equation (3.3):

$$B(y) = \frac{\mu_0 m}{2\pi y^3} + \frac{\mu_0 m}{2\pi (R-y)^3} \quad (3.3)$$

where R is the distance between two dipoles, and y is the relative height of the point we concern from the lower magnet.

And then the averaged B in the vertical direction along the center line can be calculated, which is the parameter directly related to the power output. Since Equation (3.3) shows two singularity point at $y = 0$ and $y = R$, we have to avoid calculation on these two points. Thus, B is integrated and averaged from $y = 0.002m$ to $y = R - 0.002m$, where the distance 0.002 m can be considered as the wall thickness. The relationship between the averaged B within the channel and the distance between two dipoles R is then obtained and shown in Figure 3-1.

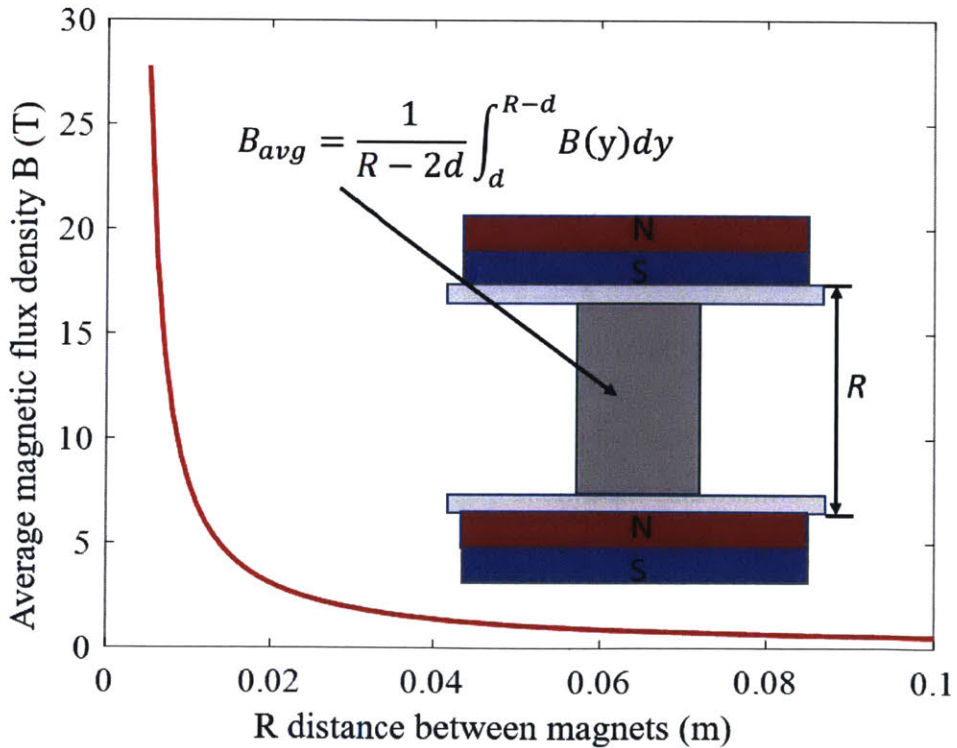


Figure 3-1: The relationship between the averaged B within the channel and the distance between two magnets with $d = 0.002m$, and unit $m = 1A \cdot m^2$.

In the figure, it is clearly shown that the theoretical averaged B decays dramatically with distance R .

3.2.2 Three-layer magnet layout design

Since the distance between the two magnets has a significant effect on B, two magnets should be kept as close as possible. However, such two big magnets are very difficult or impossible to be placed in a 2-inch pipe.

To achieve such a close distance and the thereby higher B field, a novel design is proposed that three layers of thin magnet plates are placed within the channel. And the three layers of magnets will form two separate water channels for the flow to run through. To make the design feasible for prototyping, every thin magnet plate is replaced by two thin magnet bars, which can be purchased easily online. Limited by the round shape of the pipe, the bottom and top magnet plates are smaller than the middle one. Thus the two kinds of magnet bars are with the size of $0.0508\text{ m} \times 0.0127\text{ m} \times 0.0032\text{ m}$ (2 inch \times 0.5 inch \times 0.125 inch), and $0.0508\text{ m} \times 0.0095\text{ m} \times 0.0032\text{ m}$ (2 inch \times 0.375 inch \times 0.125 inch), respectively. The material of all the magnets is Neodymium.

As the geometry of such a layout is too complicated for the theoretical calculation, the effect of such a design will be verified by magnetostatic simulation.

3.2.3 Simulation setup

The simulations in this part are performed on ANSYS AIM R19.2, with a built-in permanent magnet simulation module.

Since the simulations here are only to verify the design, only two 3D cases are carried out. The first case contains only two big magnets outsides the pipe, while the second case also includes the three-layer magnet within the pipe. The sizes of all the magnets in the simulation are the same as the real magnets. And the distance between two adjacent magnet layers is set to be 11 mm, which is composed by one 7 mm water channel and two 2 mm wall thicknesses. Although the B field can be further improved without the wall between the magnets and the water channel, a gap between them is still retained to avoid the damage to the magnets, and maintain the magnetic field in a long time.

Since the electromagnetic permeability of air, water, PVC, and ABS is very close, only the physical model of the magnets is established in the simulation. And all the other parts are set to be filled with air.

3.2.4 Simulation results

The magnetic flux density distribution in the space is simulated. After the simulations, B field and magnetic flux between the two strong magnets are shown in Figure 3-2. In the figure, it is observed that almost all the magnetic flux surrounds the magnets, and B between two magnets are relatively small. B at the center point (shown as the red dot in Figure 3-2) of this case is calculated to be 0.115 T.

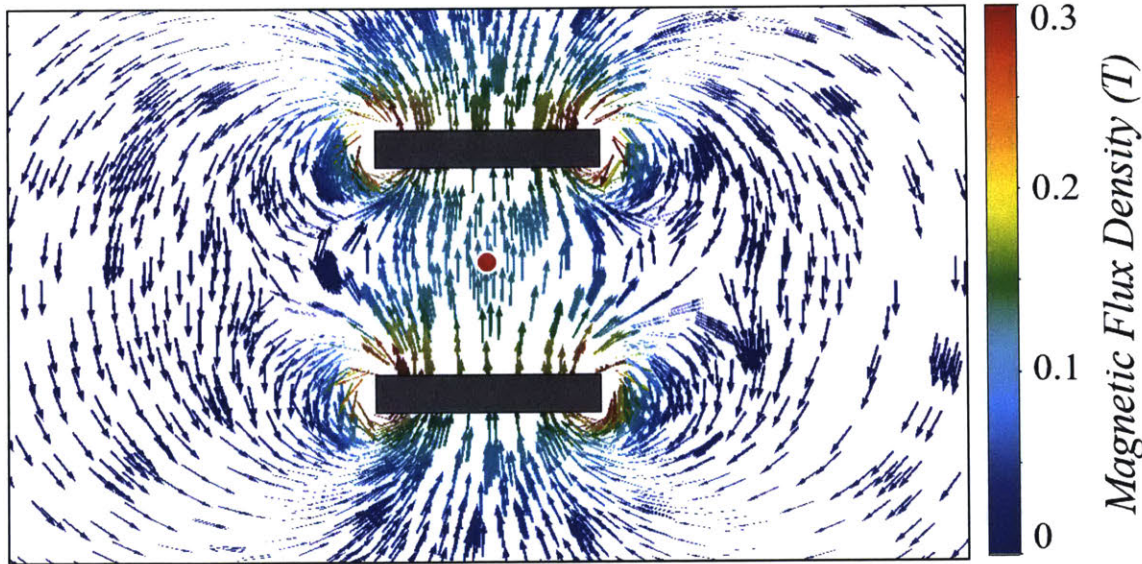


Figure 3-2: Magnetic flux induced by two strong Neodymium magnets.

The result of the second design with small magnets are shown in Figure 3-3. It is clearly shown that B in the region not close to the small magnets, is very similar to that in the first case. But B between the small magnets is dramatically amplified, indicated by both the more intensive flux and the red color. From the vector plot, it is also verified that the B field is very sensitive to the distance. And the changes far away from the magnets is difficult to function.

The magnetic flux density at the center point between two adjacent layers (shown

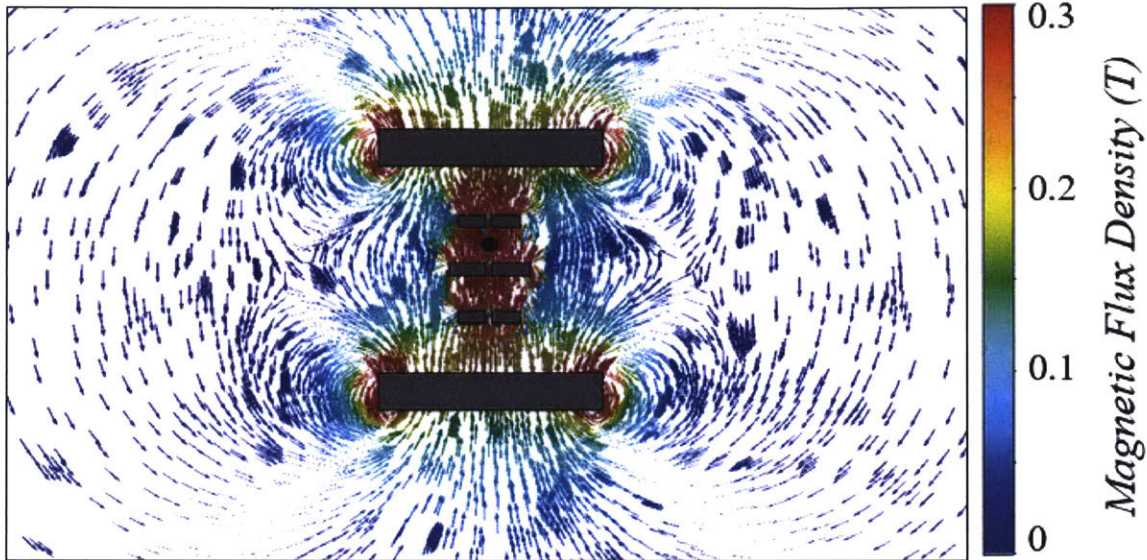


Figure 3-3: Magnetic flux with an additional three-layer magnet structure.

as the black dot in Figure 3-3) is calculated to be 0.27 T, which is increased by 2.45 times, resulting in a magnification of 6.00 times on the power output.

Thus the magnification effect of such a design on the B field is validated and this magnet layout will be used in the following discussion and the final design. Although only two cases are simulated here, the results and the conclusions should be generic for the cases with a reasonable variation of the parameters in the cases.

3.3 Magnetic Concentrator

The B field can be further optimized by a magnetic concentrator with the shape of trapezoid, which can concentrate the flux by adopting a gradually shrinking profile and material with high magnetic permeability. Material, such as Metglas, can achieve a relative permeability up to 1,000,000 at 0.5 T magnetic field. And the permeability of some typical materials are listed in Table 3-1.

With material like this, the magnetic flux can be guided and thus its density distribution within the space can be controlled. In this section, a magnetic concentrator to enlarge the average magnetic flux density B in the channel is proposed and several parameters are analyzed for a better performance.

Table 3.1: Permeability of typical materials [20].

Material	Max Relative Permeability	Magnetic Flux Density
Metglas 2714A	1,000,000	At 0.5 T
NANOPERM	200,000	At 0.5 T
Mu-metal	150,000	
Cobalt-iron	18,000	
Permalloy	8000	At 0.002 T
Iron (99.8% pure)	5000	
Air	1.00000037	

3.3.1 Concentrator design

The design comes from the trapezoid described above, where the magnetic flux can be concentrated by a factor equal to the area ratio of the two surfaces, where the flux enters and exits ideally. Although such an ideal result is hard to get since the flux can also be leaked into the surroundings from the side surface of the concentrators, the trapezoid should still work and the magnification of magnetic flux density B can be expected. Thus, the wall between the flow channel and the magnets can be replaced by this concentrator, which is denoted as the inner concentrator in the following discussion.

Moreover, a loop made of high permeability material surrounding the magnets and the inner concentrator is also proposed to gather the flux with opposite direction in the loop. Without it, the vector with the opposite direction will be distributed everywhere spatially in the space, including the water channel. The proposed concentrator design together with the magnets is shown in Figure 3-4.

The loop directly contacts the two surfaces of two magnets to capture more opposite flux. Except for the part contacting the magnets, the shape of the loop is designed to be a half ellipse to reduce the flux leak at the sharp turn, while it can also minimize the concentrator size.

3.3.2 Validation and parameter study

In this case, the shape of the materials with different permeability is too complex and the effect of the concentrator is also greatly limited by the saturation of the

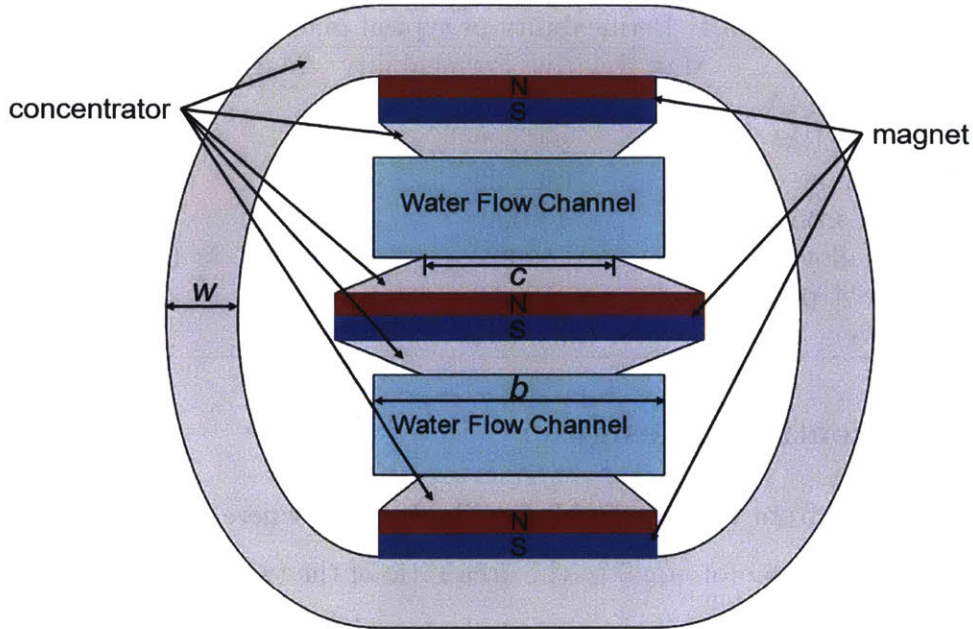


Figure 3-4: Front view of the concentrator design.

material since the flux density within the material can easily saturate if the size of the concentrator is confined. Thus, magnetostatic simulations are adopted in this part to get more accurate results. The magnet property in the simulation is described by a demagnetization curve shown in Figure 3-5.

To generalize the results and reduce computational power consumption, 2D simulation is selected. The geometry parameters used in this part are also shown in Figure 3-4. The channel width b and the concentrator size c are both fixed to be 0.02 m and 0.013 m. The channel width is almost the same as the magnet width, while the concentrator width should be smaller than the channel width since the width an inner concentrator can influence is wider than c , as discussed in Appendix A. In all the cases, the inner ellipse of the loop does not change and only the outside edge is changed according to the loop width w .

Validation

Firstly, the function of the inner concentrator and the loop is validated. Here, three cases are discussed about to validate the function of the inner concentrator and the

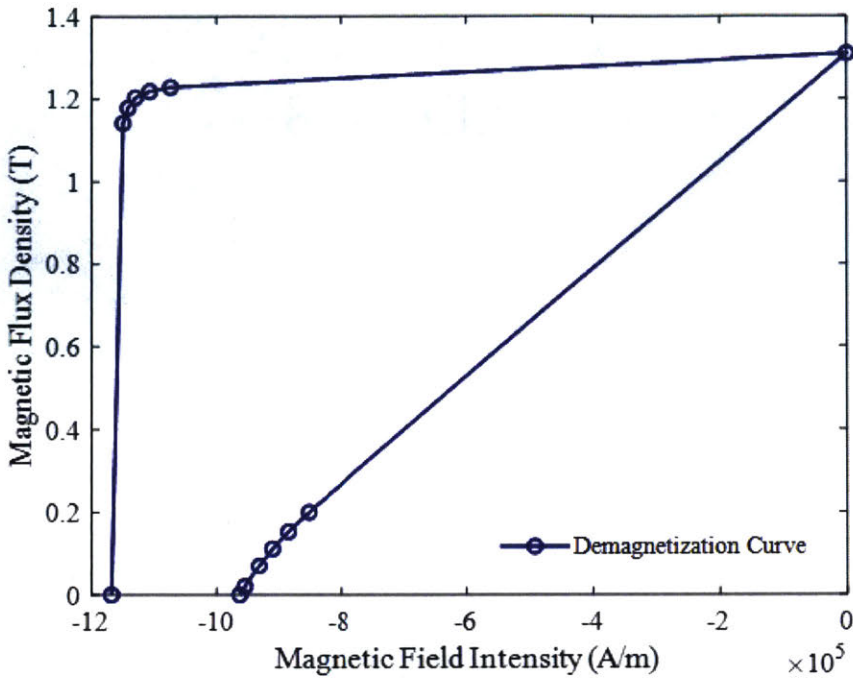


Figure 3-5: Demagnetization curve for N42 grade Neodymium magnets.

loop respectively. The first case is only the three-layer magnets, while the second one adds the inner concentrator, and the third one adds the loop. The material used for the concentrator here is mu-metal. And the loop width w is set to 0.005 m. The magnetic flux vector plot and y-directional magnetic flux density contour are shown in Figure 3-6 and Figure 3-7 respectively.

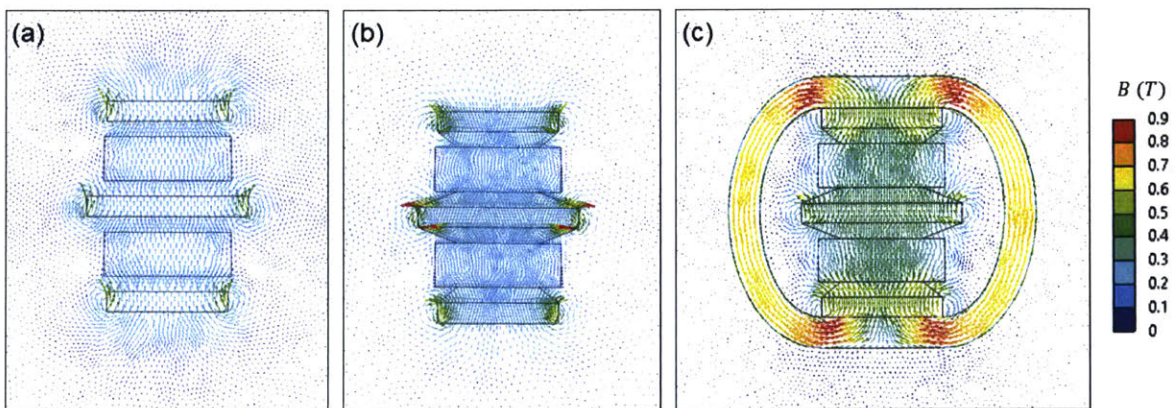


Figure 3-6: Magnetic flux vector plot. (a) only magnets; (b) magnets and inner concentrator; (c) magnets, inner concentrator, and loop with width $w=0.005$ m.

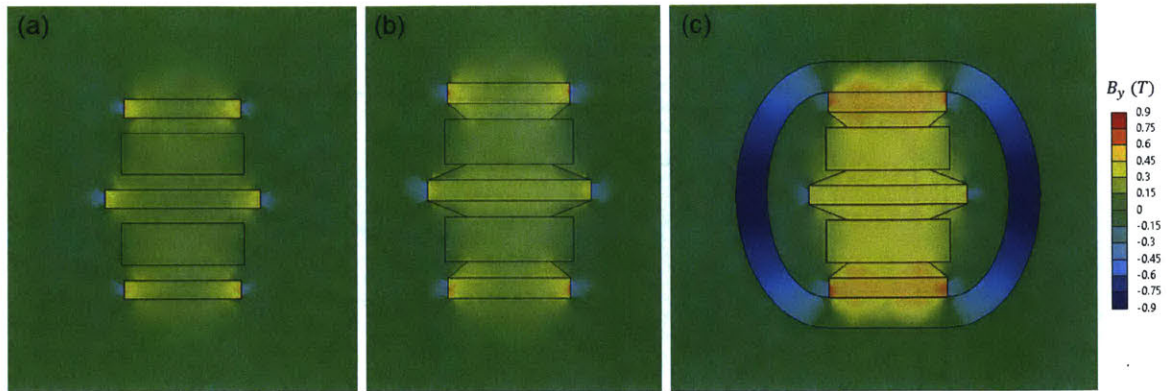


Figure 3-7: Contour of magnetic flux density in y-direction. (a) only magnets; (b) magnets and inner concentrator; (c) magnets, inner concentrator, and loop with width $w=0.005$ m.

From the contour and the vector plot, it is clearly shown that the flux is guided by the high-permeability material. And in Figure 3-6 (c), the loop collects almost all of the flux with opposite direction starting from the top side of the top magnet to the bottom side of the bottom magnet. And the magnetic flux density in the loop can even reach 0.9 T at the ends of the ellipses where the loop just collects most of the flux out of the magnets. And when the flux travels in the loop, some flux leaks into the surroundings. From the contour comparison, it is shown that with the inner concentrator and the loop, the directional magnetic flux density is greatly amplified. The average y-directional magnetic flux density B_y in the channel is also calculated, and shown in Table 3-2.

Table 3.2: Simulation results for effect validation.

Case Number	Case Description	Average B_y	Comments
1	Figure 3-6 (a)	0.156 T	
2	Figure 3-6 (b)	0.176 T	12.8% more than case 1.
3	Figure 3-6 (c)	0.342 T	119.2% more than case 1.

The effect of the inner concentrator is limited by its size and it can also concentrate the flux with opposite direction. After adding the loop, flux with both directions are guided. And most of the flux with the undesired direction is constrained in the loop, thus the Average B_y is dramatically amplified.

Material

The effect of the concentrator highly depends on the magnetic permeability of the material. The concentrator role is to attract more flux within this material to rearrange the magnetic flux distribution. But this effect may be also limited by other properties, such as the induction saturation, which constrains the maximum flux density in the concentrator.

The two typical materials discussed here are mu-metal and Metglas 2417A, whose B-H curves are shown in Figure 3-8. Metglas has a much higher permeability, but lower saturation induction at only 0.6 T.

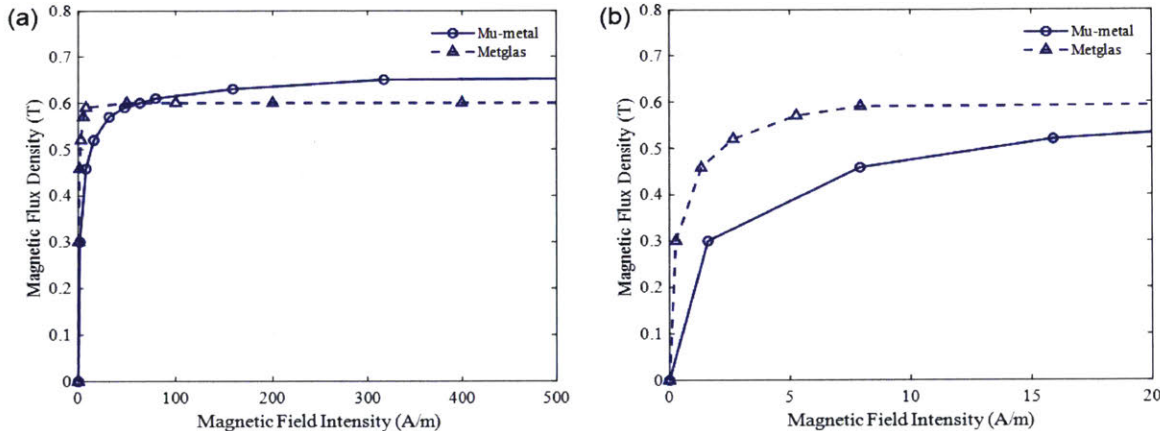


Figure 3-8: B-H curve of mu-metal and Metglas. (a) overview; (b) detailed view.

The contour of magnetic flux density in y-direction, magnetic flux vector plot, and the contour of magnetic flux density magnitude of the cases with 5 mm loop width are shown in Figure 3-9, Figure 3-10, and Figure 3-11, respectively.

In Figure 3-9, the contour of the two cases are almost the same, except for that, with mu-metal concentrators, B_y is stronger in the area of magnets. The average B_y in the channel are calculated to be 0.329 T and 0.342 T for the Metglas concentrator and the mu-metal concentrator.

In Figure 3-10 and Figure 3-11, the magnetic flux density in the loop of mu-metal is much higher than that in the Metglas loop. And thus more flux with opposite direction is constrained by the mu-metal loop, resulting in a higher magnetic flux

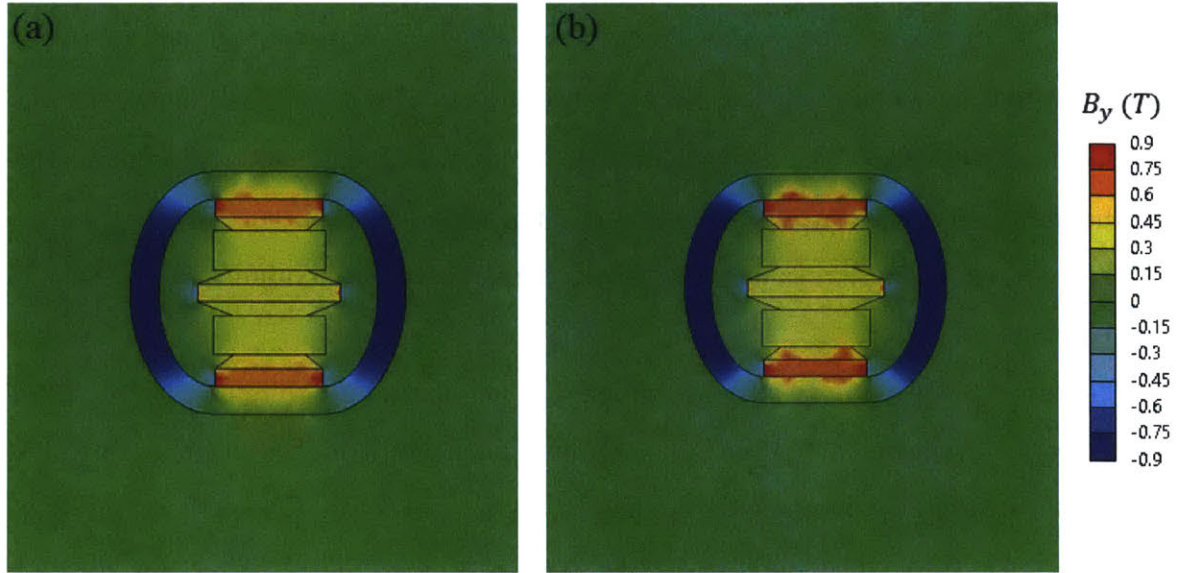


Figure 3-9: Contour of magnetic flux density in y-direction. (a) metglas; (b) mu-metal.

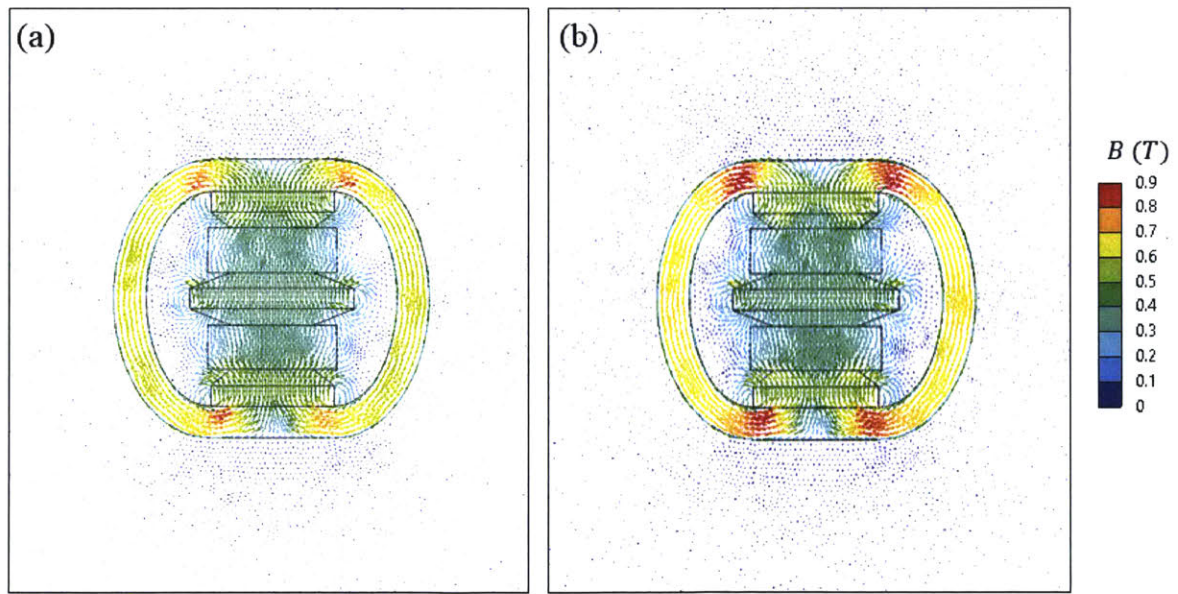


Figure 3-10: Magnetic flux vector plot. (a) metglas; (b) mu-metal.

density in the water channel. The similar difference between the materials happens almost in all different loop widths. The average B_y in the channel is 0.249 T and 0.255 T for Metglas and mu-metal at loop width of 0.002 m, while 0.417 T and 0.422 T for Metglas and mu-metal at loop width of 0.015 m.

Thus the saturation induction of the concentrator material is the key property

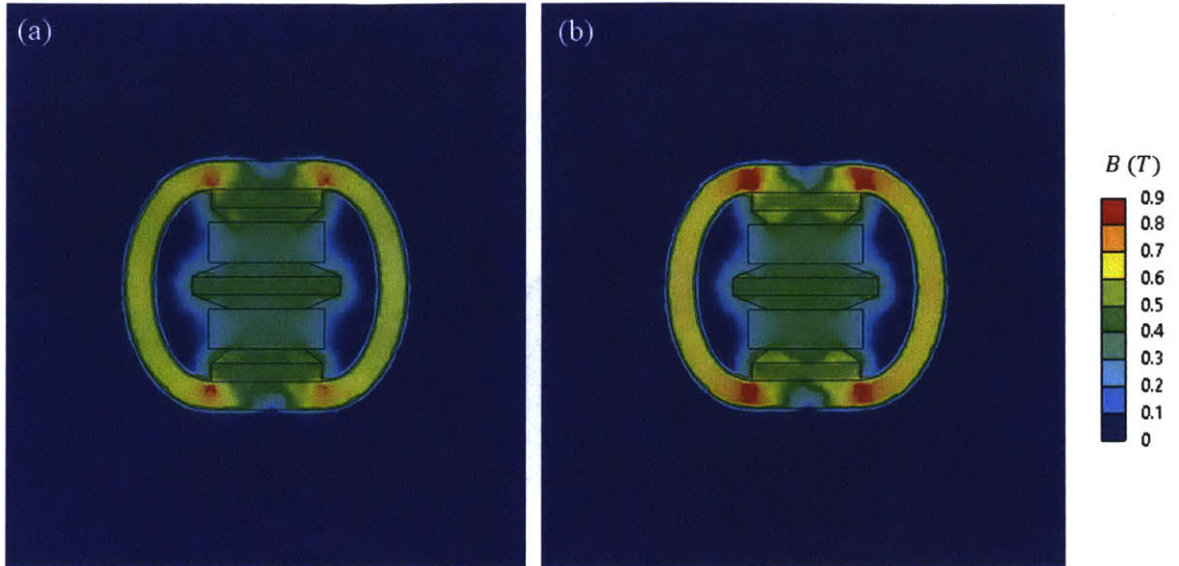


Figure 3-11: Contour of magnetic flux density magnitude. (a) metglas; (b) mu-metal.

in this concentrator design. Although Metglas owns a much higher magnetic permeability than mu-metal, it is still desirable to choose mu-metal because of its much higher induction saturation value. And in the following discussion, only material of mu-metal will be focused on.

Loop width

The loop width is another important parameter influencing the effect of the concentrator, as it determines the max amount of flux the loop can contain and guide. To systematically discuss the effect of the loop width, a series of simulations are run with various loop widths from 1 mm to 15 mm. And the average B_y are calculated and plotted in Figure 3-12.

The average B_y increases with the loop width before 0.01 m, where the relationship is almost linear. In this period, the magnetic flux density in the material is saturated and thus the magnetic flux with opposite direction the material contains is linear with the loop width. When the loop width exceeds 0.01 m, the material induction saturation stops. Thus, it does not change with the loop width any more, as almost all the magnetic flux with opposite direction is constrained in the loop already. The

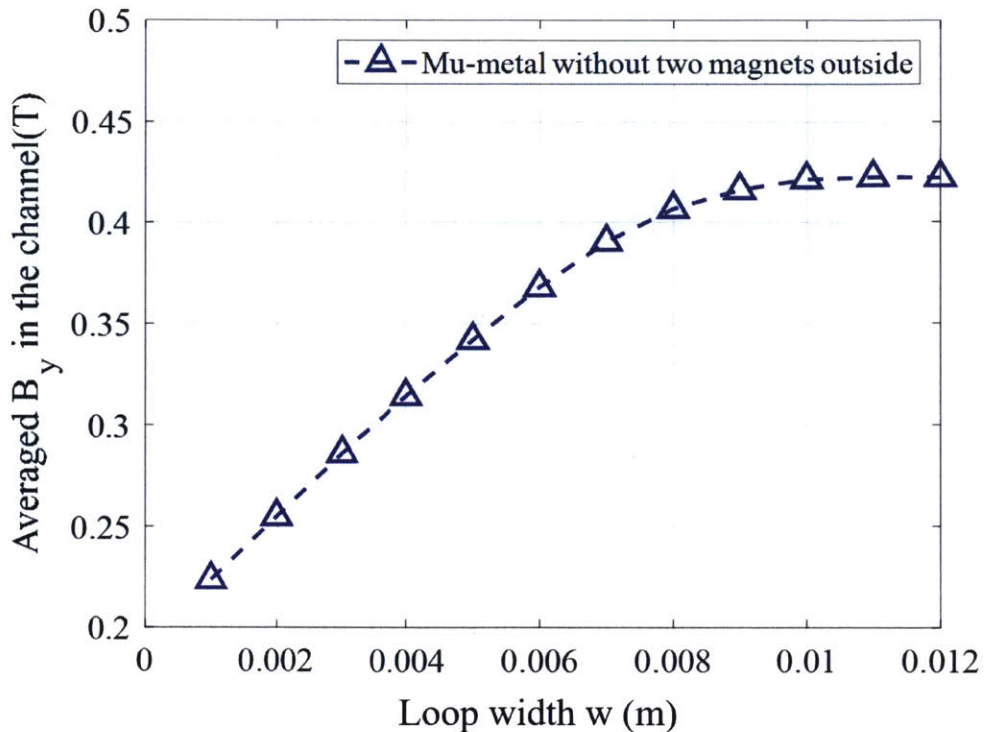


Figure 3-12: Average B_y in the channel with various loop widths.

magnetic flux density contour of the case with loop width of 0.002 m, and 0.015 m are shown in Figure 3-13.

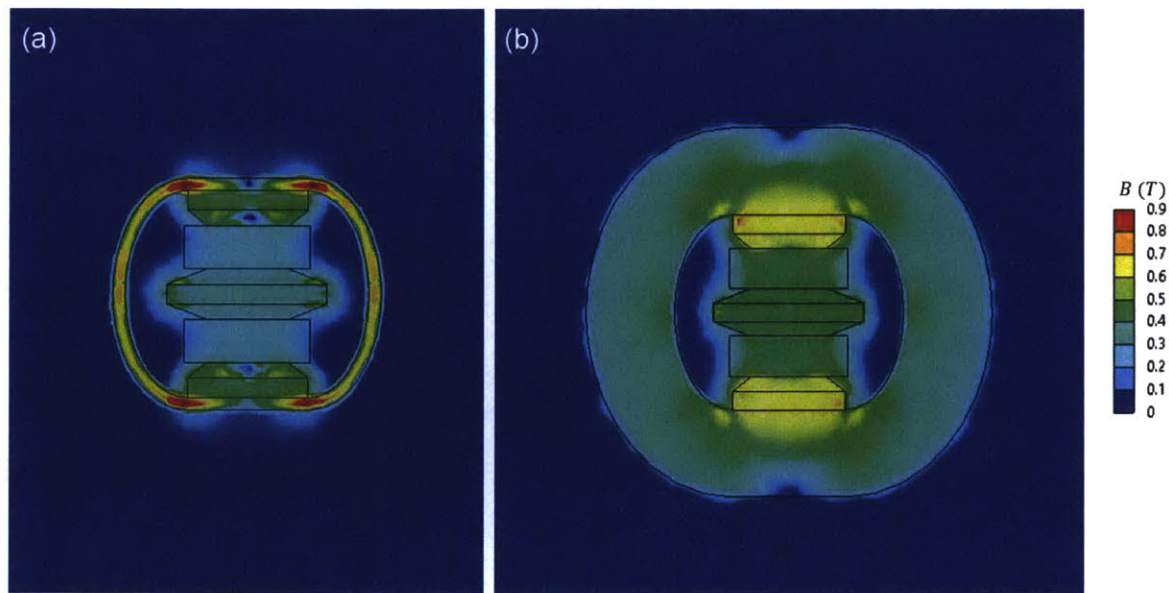


Figure 3-13: Magnetic flux density contour for the cases with loop size of (a) 0.002 m; (b) 0.015 m.

After comparing with Figure 3-11 (b) and Figure 3-13, it is found that the magnetic flux density in the loop with the size of 0.002 m and 0.005m are almost the same, while the magnetic flux density of the 0.015 m width loop is much weaker. Thus the above analysis is validated. When determining the optimal loop size, simulations should be performed first and then the optimal loop width can be decided according to the results. Moreover, it's useless to further increase the loop size after the average B_y does not increase any more.

Magnets outside

It can be validated by the results in Section 3-2 that additional stronger magnets placed outside the pipe can strengthen the magnetic flux density in the channel. But the loop with high permeability can make a difference on this results because the loop may contain and block the flux generated by the strong magnets. This effect can occupy part of the material capability to guide the opposite flux density from the three-layer magnet.

In this part, the loop width changes from 1 mm to 12 mm, where 12 mm is the max loop size we can place in this setting. And the material selected in the simulations is mu-metal with the B-H curves shown in Figure 3-8. The average B_y in the channel of these cases are plotted in Figure 3-14.

At small loop widths, the two strong magnets outside can help build a stronger magnetic flux density field. But when the loop width exceeds 0.008 m, the effect of the two magnets outside can even reduce the magnetic flux density.

From the vector plot with 0.01 m width loop, it is clearly shown that with the two big magnets, the loop uses too much of its capability to contain and guide the flux generated by the big magnets. And thus more flux with opposite direction generated by the three-layer magnet is distributed in the water channel, resulting in a weaker magnetic flux density within the flow channel. After removing the big magnets, the magnetic flux density increases from 0.408 T to 0.422 T by 3.4%. Moreover, the existence of the two strong magnets generates magnetic field everywhere in the space, which may cause severe noise and damage to the sensors along the pipe.

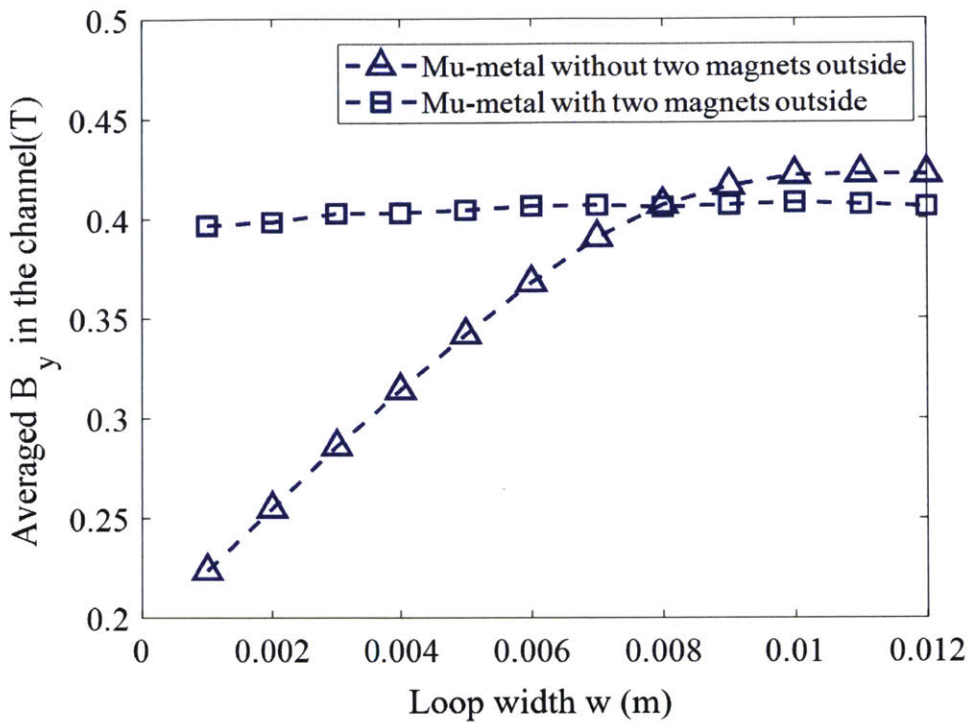


Figure 3-14: Average B_y in the channel with and without two big magnets outside.

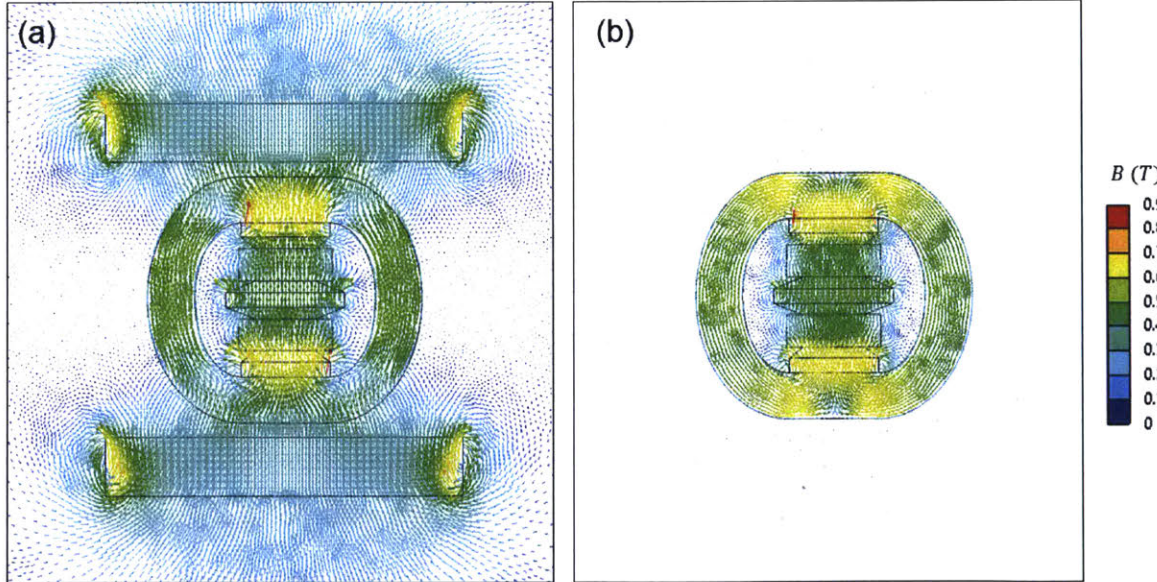


Figure 3-15: Magnetic flux vector with and without two big magnets outside.

Thus, a 0.01 m width loop with only the three-layer magnet is the best results in the analysis of this part. With pipes and magnets of other sizes, similar analysis can be conducted and then the optimal parameters can be determined.

3.4 Summary

In this chapter, the magnetic field is analyzed theoretically and simulated to investigate the possible modification to enlarge the averaged B_y in the channel.

Firstly, it is found that the magnetic field is very sensitive to the distance between magnets. In this case, a special design with an additional three-layer magnet sandwich is proposed. And its effect is validated with magnetostatic simulations.

Secondly, a magnetic concentrator composed by inner concentrators and a loop with high magnetic permeability is proposed to be assembled into the design to further improve the results. Several parameters, including material, loop width w , the existence of big magnets outside, are discussed systematically based on simulation results. And finally a 0.01 m width loop concentrator with mu-metal is determined to be the best in this application. The analysis approach can be generalized to other applications easily.

Chapter 4

Flow Field Analysis and Optimization

The flow field is another field that will dramatically influence the power output. With proper and careful design, it will greatly benefit the final results.

4.1 Problem Description and Assumption

The problem with fixed far field inlet velocity is much easier to analyze using mass conservation relationship for incompressible flow. Under this assumption, a smaller size channel always contains higher velocity flow.

But this is not always the case in real water distribution system. It is very easy to imagine that flow velocity will be dramatically reduced if the channel is shrunk to a very small size. Some pumps, like the piston pumps, can provide nearly fixed far field flow velocity within a reasonable range of the channel sizes since the piston working cycle and the piston volume are both almost fixed after starting to work. But this kind of pumps is not widely used since it costs too much manpower and money to maintain, given its complex structure.

On the contrary, centrifugal pumps are widely used in a real scenario. But it introduces a new problem to our analysis that pressure and velocity are always coupled. And it is very difficult to set velocity or pressure fixed if we change the size and geometry of the flow channel. However, for most centrifugal pumps, pressure is much more consistent when compared with the flow velocity. The working curve for a

typical centrifugal pump (Barmesa IA3H-40-2 OPD End-Suction Centrifugal Pump) is shown in Figure 4-1. In the figure, the flow rate varies from 0 to 850 gallons per minute, and different curves represent different RPMs. However, all the curves show a similar trend that the pressure output of the pump at a reasonable range of flow rates is nearly consistent. This conclusion can be drawn for most of the pumps on the market.

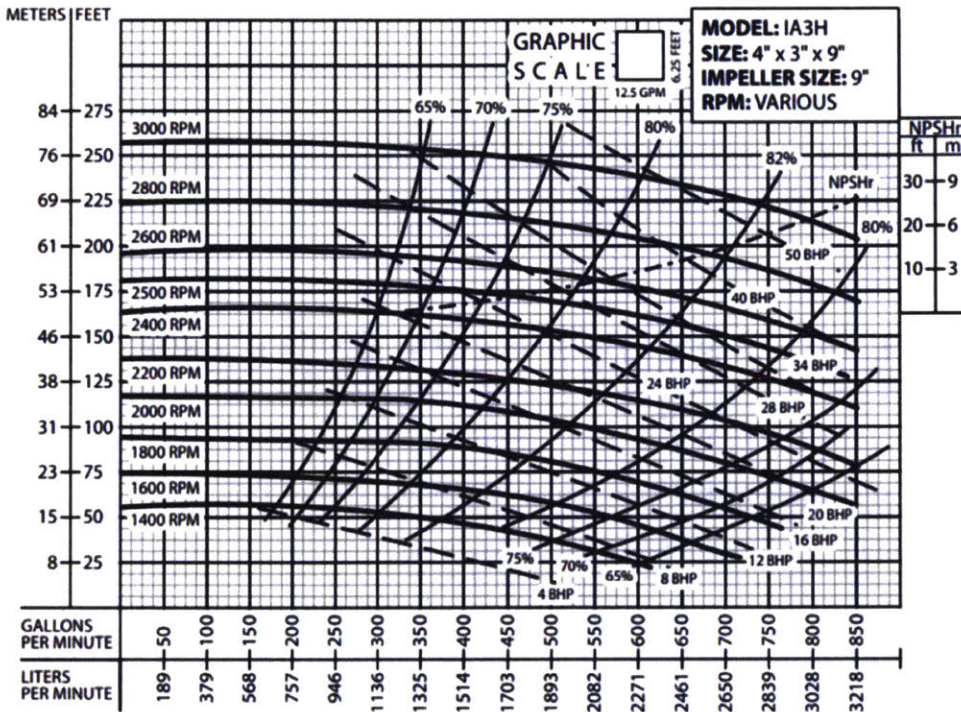


Figure 4-1: Working curve of a typical centrifugal pump [21].

Thus, to simplify the analysis and the simulation setup, it is reasonable to set the inlet boundary as pressure inlet and assume that the geometry and size change of the energy harvester will not affect inlet pressure markedly. Although this assumption can be trivial if a turbine can be involved in the simulation, it will dramatically increase the computation complexity and power consumption. Thus in this thesis, we will stick to the assumption of relatively constant inlet pressure.

4.2 CFD Model and Setup

Theoretical model and analysis can be difficult to obtain accurate flow information for the design. As the flow velocity has a quadratic contribution on the power output, the error may cause a huge difference. In this case, 3D transient CFD simulation is performed to help provide much more accurate flow field information and improve the design of the flow channel. The simulation is executed on the platform of ANSYS Fluent R19.2.

Given the experimental setup limitation in the lab, the length of the prototyped energy harvester is controlled to be 0.09 m, although longer harvester can enlarge the power output. To better generalize the discussion, eliminate the wall effect within the channel, and simplify the simulation setup, a square channel with the same h and b is modelled first in the simulation. This series of simulations determine the primary size of the channel. Later, another series of simulation with the same determined h , but with various b are performed to determine the width b of the channel.

The length of computational region concerns the full development of the pipe flow and wake after the inlet and the energy harvester, resulting in a length of 2L and 5L in front of and behind the harvester respectively, as shown in Figure 4-2. The standard $k-\omega$ turbulence model is adopted in the simulation to better recover the turbulence characteristics near the wall of the channel. The transport equation of the turbulence model is shown in Equation (4-1) and (4-2):

$$\frac{\partial}{\partial t}(\rho k) + \frac{\partial}{\partial x_i}(\rho k u_i) = \frac{\partial}{\partial x_j}(\Gamma_k \frac{\partial k}{\partial x_j}) + G_k - Y_k + S_k \quad (4.1)$$

$$\frac{\partial}{\partial t}(\rho \omega) + \frac{\partial}{\partial x_i}(\rho \omega u_i) = \frac{\partial}{\partial x_j}(\Gamma_\omega \frac{\partial \omega}{\partial x_j}) + G_\omega - Y_\omega + S_\omega \quad (4.2)$$

where t is the time, ρ is the fluid density, u_i is the Favre-averaged velocity vector, x_i and x_j are the position vectors, k is the turbulence kinetic energy, ω is the dissipation rate, G_k and G_ω represent the generation of turbulence kinetic energy and ω ; Γ_k and Γ_ω represent effective diffusivity of k and ω ; Y_k and Y_ω represent dissipation of k and

ω ; and S_k and S_ω represent the source terms. Double precision is also selected to increase accuracy and avoid unnatural eddy dissipation.

The non-structural mesh is created by the Meshing component within ANSYS Workbench and is also shown in Figure 4-2. Mesh near the pipe wall and channel wall is specifically refined to capture more details and guarantee simulation accuracy. In the serial simulation, the square channel edge lengths are set to be 1 mm, 3 mm, 5 mm, 7 mm, 9 mm, 11 mm and 13 mm. And in the second series of simulation, h is set to be 7 mm, while b is set to be 5 mm, 10 mm, 15 mm, 20 mm, 25 mm, and 30mm. And the inlet boundary is a pressure inlet boundary with the pressure of 10,000 and 20,000 pa, and the outlet is pressure outlet.

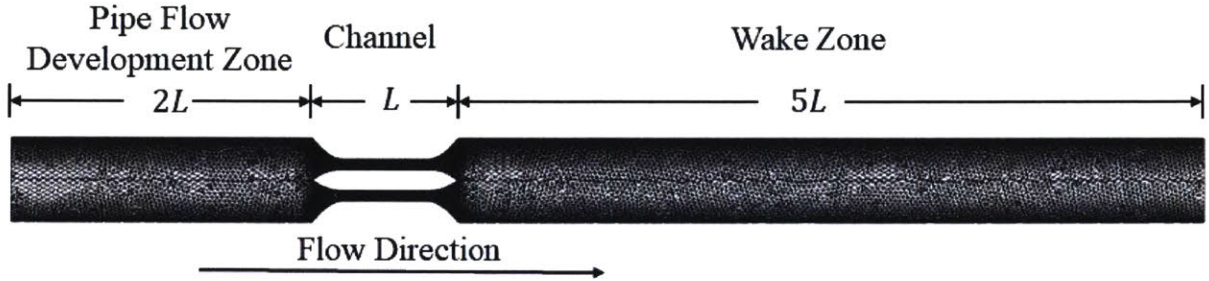


Figure 4-2: Computational region schematic and mesh.

The flow time in the computation is set to be 4 s with a time step of 0.002 s, guaranteeing convergence of all the parameters, which shows up even before flow time of 1 s.

4.3 CFD Results and Analysis

4.3.1 Simulation with square channels

The most important output parameter, which is directly reflected in the final power output, is the flow velocity in x-direction u_x . The contour of u_x , in the case, with 7 mm channel and 10,000 pa inlet pressure is shown in Figure 4-3. It is clearly shown that the flow in the channel is much faster than that in the pipe. And the max u_x in this case reaches 5.33 m/s, while the averaged u_x on the outlet surface is only

0.16 m/s, which is magnified by 33.3 times. Thus, the magnification on the flow velocity of the channel when compared with the far-field flow is verified. Wakes out of two channels tend to move close and merge to each other, and finally form a new asymmetric wake with a vortex core dissipated quickly. The asymmetric wake can also be found in other researches. And all the 14 cases show similar results.

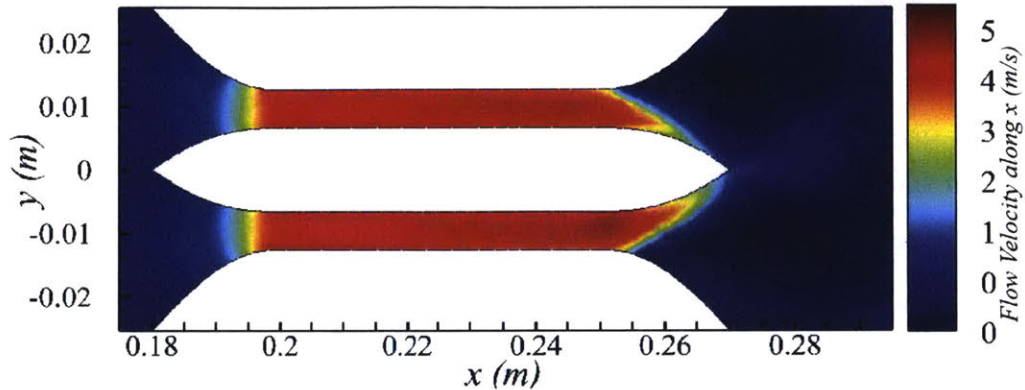


Figure 4-3: The contour of u_x in the case with 7 mm channel and 10,000 pa inlet pressure on the slice $z=0$.

However, since most pipe systems are pressure driven, which means the inlet pressure is almost constant, but not inlet velocity, we should also study the influence of the harvester on the flow field. The pressure contour of the above case is shown in Figure 4-4. It is clearly shown that the pressure in front of the harvester is much higher than the pressure behind, which may cause a large force on the harvester and significant head loss on the flow.

The force acting on the energy harvester and the averaged u_x within the channel are shown in Figure 4-5 and 4-6, respectively.

The force decreases with the channel size. But the change is relatively small, which gives out a much similar value for all the channel sizes. The u_x within the channel increases if the channel becomes bigger. This is reasonable since the block on the flow counts in this problem. But it is also found that the slope becomes much smaller at large channel sizes. The change between the 1 mm and 3 mm cases are much more observable than all the other intervals. The reason is that the block effect on the flow tends to be trivial when the channel is big enough, and the resultant

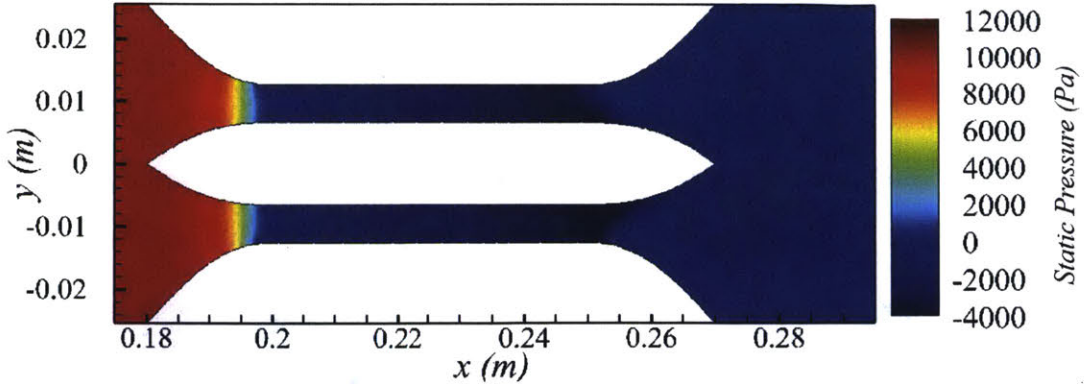


Figure 4-4: Static pressure contour in the case with 7 mm channel and 10,000 pa inlet pressure on the slice $z=0$.

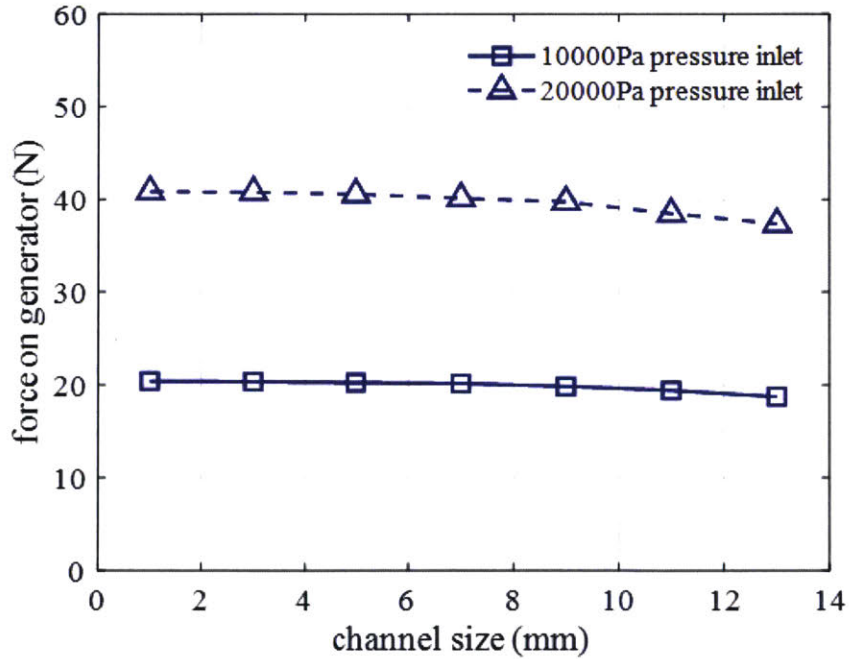


Figure 4-5: Force acting on the energy harvester in the x-direction.

velocity difference is further eliminated by the larger channel size according to mass conservation principle. Thus, if other design parameters require the channel size to be small, the channel size is still better to be in the region of relatively large values, which can partially eliminate the effect of channel size on the flow velocity.

Based on the above preliminary analysis, the channel height h is set to be 7 mm in the following analysis and the final design. And here are three reasons:

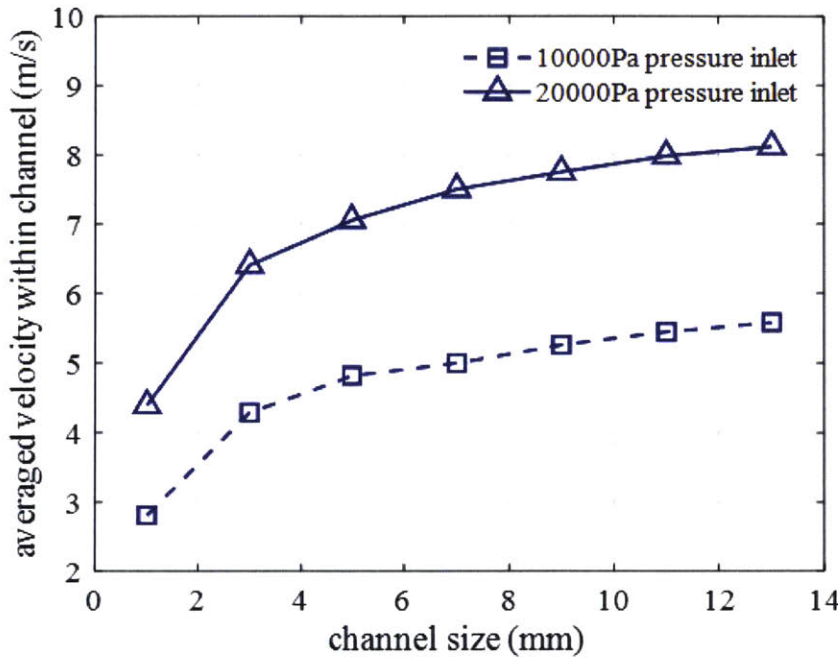


Figure 4-6: Averaged u_x within the channel.

- 1) The averaged u_x within the channel does not change too much if the channel size is increased from 7 mm;
- 2) Although magnetic field requires the distance between magnets, and the channel height to be small with a higher order contribution on the power output, the resultant enlarged channel volume and the flow velocity with a larger h both mitigate the effect and requirement of the magnetic field.
- 3) If the channel height is too small, it will dramatically influence the flow field and the water distribution capability in the system. Moreover, it will also introduce a much stronger force on the harvester. And the height 7 mm is very difficult to be further enlarged in a 51 mm inner-diameter pipe together with three layers of magnets inside.

4.3.2 Simulation with various channel widths

After the channel height h is determined to be 7 mm, the influence of the channel width on the flow field and the power output is investigated in this subsection with

the second series of CFD simulations. The u_x contours of the six cases are shown in Figure 4-7.

In the figure, it is clearly shown that, the flow velocity before the channel and in the channel both increases with b , which means the influence of b on the far field flow velocity is more than the first order. The wakes after the channel in Figure 4-7 (a), (b) and (c) are quite similar that the two wakes out from two channels tend to separate and move to the pipe wall. But the wakes in (a) and (c) are the most symmetric ones. When b decreases below 20 mm, the wakes become very messy. Moreover, it is clearly shown that the wake in (f) is so weak, when b equals to 5 mm, that the turbulence is almost dissipated near the pipe wall.

The averaged u_x within the channel in every case are plotted in Figure 4-8.

Higher pressure can dramatically increase flow velocity. But the relationship between the pressure and velocity is not proportional since higher pressure and velocity bring in more energy dissipation. And it is also observed that the average u_x is very consistent that it does not change too much with the variation of b . It is because that the block effect on the pipe flow is almost the first order of b , thus the effect of b on u_x is eliminated after manipulation of dividing pipe flow velocity by b to get the channel flow velocity. But increasing b can still benefit the u_x to some extent.

4.4 Other Concerns

Influence of the harvester on the flow velocity can be modeled by the energy equation for steady, incompressible one-dimensional flow and horizontal pipes in terms of hydraulic heads, as shown in Equation (4.3)

$$\frac{P_0}{\rho g} + \alpha_0 \frac{u_0^2}{2g} = \frac{P_1}{\rho g} + \alpha_1 \frac{u_1^2}{2g} + h_L \quad (4.3)$$

where P_0 and P_1 are the far-field static pressure and the static pressure at the point we concern; u_0 and u_1 are the far-field velocity and the velocity at the point we concern; α_0 and α_1 represents the far-field kinetic energy correction factors and the kinetic energy correction factor at the point we concern; g is the gravitational

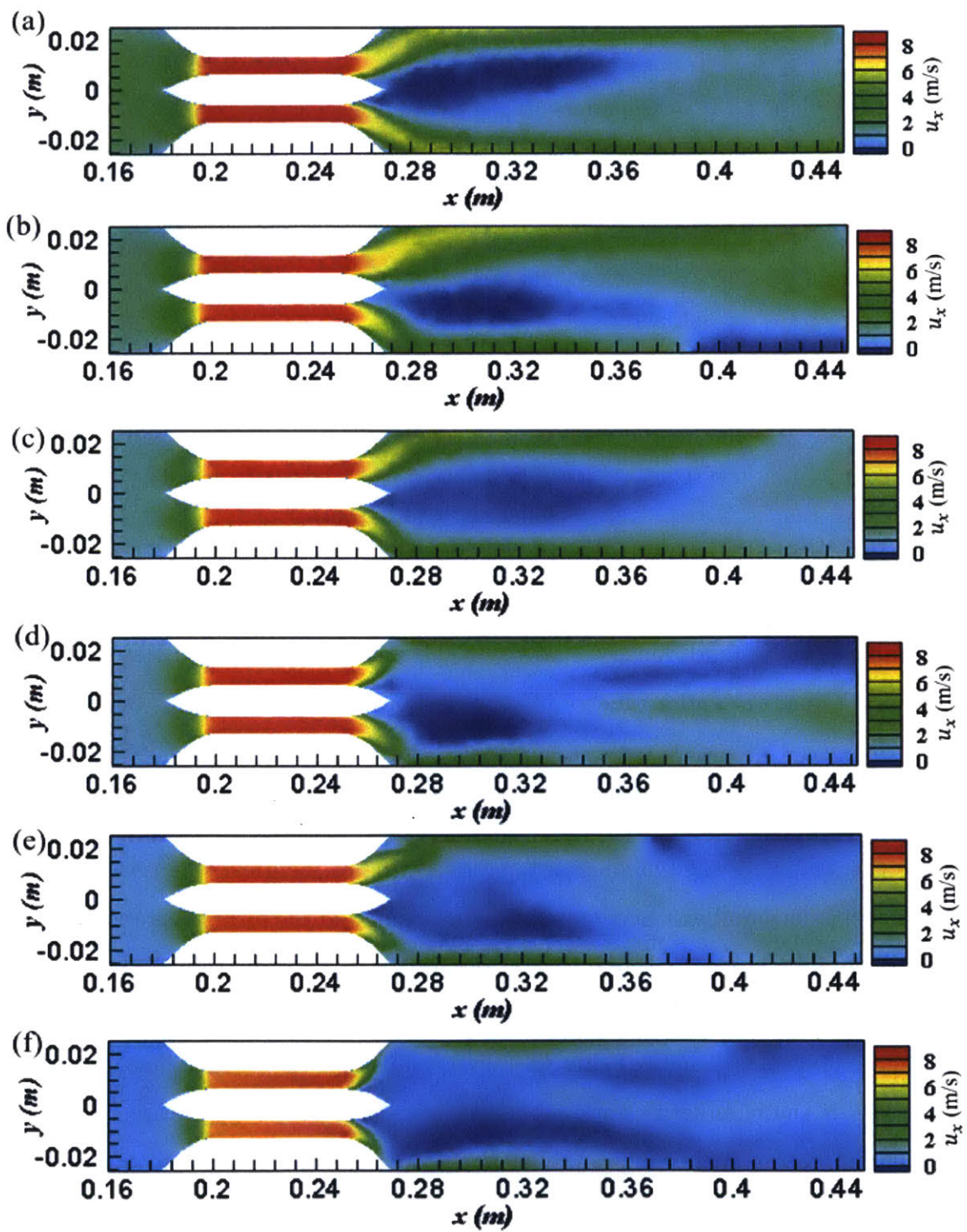


Figure 4-7: Contour of u_x with fixed $h=7$ mm and 20,000 Pa inlet pressur inlet. (a) $b=30$ mm, (b) $b=25$ mm, (c) $b=20$ mm, (d) $b=15$ mm, (e) $b=10$ mm, (f) $b=5$ mm.

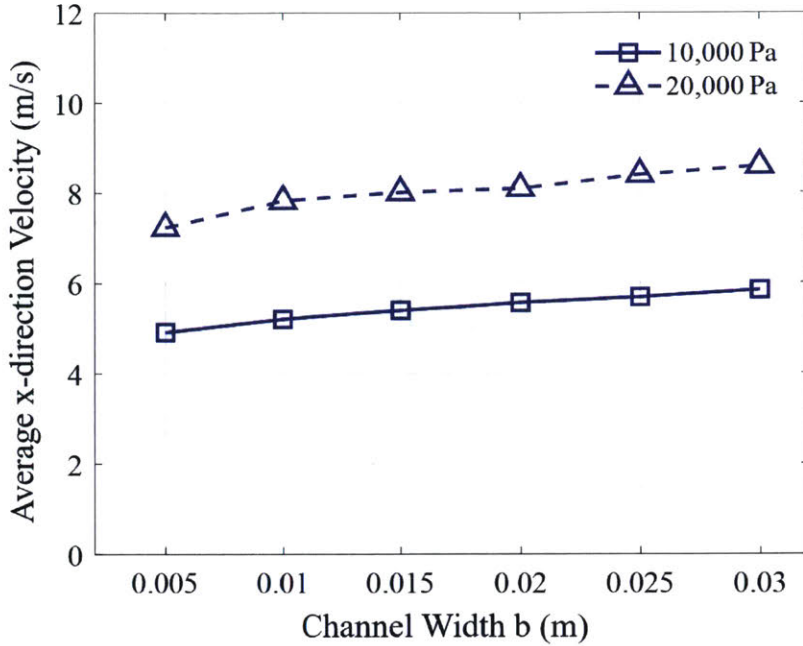


Figure 4-8: Averaged u_x within the channel with various channel width b .

constant; ρ is the fluid density; and h_L is the total hydraulic head loss due to both friction dissipation, and geometry of inlet and outlet of the channel.

4.4.1 Channel entrance and exit geometry

Since the shapes of the channel and the pipe are not identical, the geometry of the channel entrance and exit becomes very significant, and the form resistance coefficient can be dominant once without careful design. It is already studied that head loss caused by geometry can be made very small by using an appropriate rounded entrance geometry [18]. Thus, a gradually shrinking transition should be adopted to reduce head loss if the channel is not with the same shape as the pipe wall. And it can also eliminate the vortex development and associated energy dissipation at the flow entrance.

4.4.2 Surface friction

Friction is another main source of energy dissipation between flow and the pipe wall in our application. The head loss caused by friction dissipation can be illustrated by

the Darcy Weisbach equation, i.e. Equation (4.2),

$$h_f = f \frac{L}{D} \frac{V_{avg}^2}{2g} \quad (4.4)$$

where h_f is the head loss caused by friction; f is the Darcy friction factor, L is the length of the pipe; D is the hydraulic diameter of the pipe or the channel, and V_{avg} is the averaged velocity, and g is the gravitational constant.

There are various methods to determine f . However, the most famous and popular one is to use the Moody chart, which is shown in Figure 4-9. In the figure, the shaded area corresponds to the hydraulic smooth area where $k_s^+ < 5$.

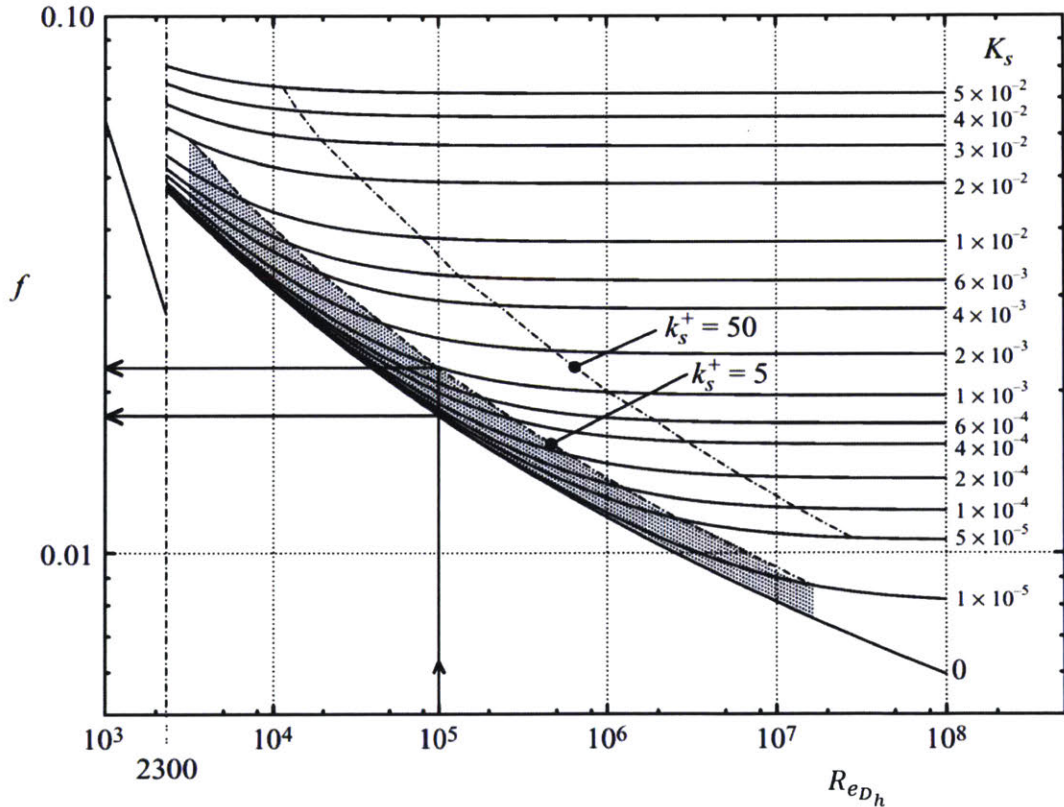


Figure 4-9: Moody chart for pipes covered with sands [22].

In the figure, K and Re_{D_h} are the roughness number and the Reynolds number defined by:

$$Re_{D_h} = \frac{\rho u D_h}{\mu} \quad (4.5)$$

$$K = \frac{k}{D_h} \quad (4.6)$$

where D_h is the hydraulic diameter, while k is the mean height of pipe roughness.

The flow regime is divided into three zones based on the Reynolds number. When the Reynolds number is below 2300, the wall roughness does not contribute to f according to Figure 4-9. When the Reynolds number reaches 2300, the flow becomes a turbulent flow, and the roughness has a significant influence on f . When the Reynolds number increases further to fully developed turbulent flow region, f will only depend on the wall roughness, regardless of Reynolds number [22].

The energy harvester designed in this thesis will work with turbulent flow most of the time. And the designed energy harvester is prototyped by 3D printing, whose working principle introduces a high wall roughness on the channel wall.

Thus in the design and fabrication process, special consideration should be taken, such as a smooth coating on the channel walls.

4.5 Summary

In this chapter, all the analysis about the flow field is carried out. First, an assumption, that the pressure at the pipe inlet is almost consistent, is discussed and adopted. Next, simulations with square channels are performed to determine the channel height to be 7 mm after careful investigation. And then, series of simulation with various channel width b and fixed channel height h are carried out to provide data of the average u_x . Finally, the influence of the channel entrance and exit geometry, and surface friction is also discussed. This chapter is an overall description and discussion of the key factors to the flow field, which provides detailed information and comprehensive guidance to the design and optimization.

Chapter 5

The Optimized Design and Experiments

Based on the analysis in the above chapters on both magnetic field and flow field, an optimized design is derived, prototyped with 3D printing, and tested at the MIT Mechatronics Research Laboratory.

5.1 Summary of the Analysis

The analysis is summarized below:

- (1) Since the magnetic field distribution around the magnets is very sensitive to distance, a three-layer magnet sandwich added inside the pipe is proposed. And its effect is validated with simulation studies. The height of the two flow channels are set to be 7 mm to balance the block effect of the generator on the flow field.
- (2) Series CFD simulations with the same channel height 7 mm are carried out, and the averaged flow velocity within the channel for every channel width is obtained. The flow velocity increases with b .
- (3) A magnetic concentrator is proposed to be assembled into the design to further improve the magnetic field B without interfering with the flow field. And the loop width is determined to be 0.01 m to contain most of the flux with opposite direction, but still with a very low volume.

5.2 Final Design

The CAD of the final design is shown in Figure 5-1, where magnets are labeled red; inner concentrators are yellow; the water channel wall is light grey; and the loop is black. In the design, the energy harvester is composed of two flow channels with the size of 7 mm × 20 mm. The three layers of magnets are placed between the two channels. The thickness of the concentrators between the magnets and the flow channel is 2.5 mm, which provides support for the structural load and protection for the magnets. A round transition between the pipe wall and the flow channel is extruded to reduce form drag on the flow.

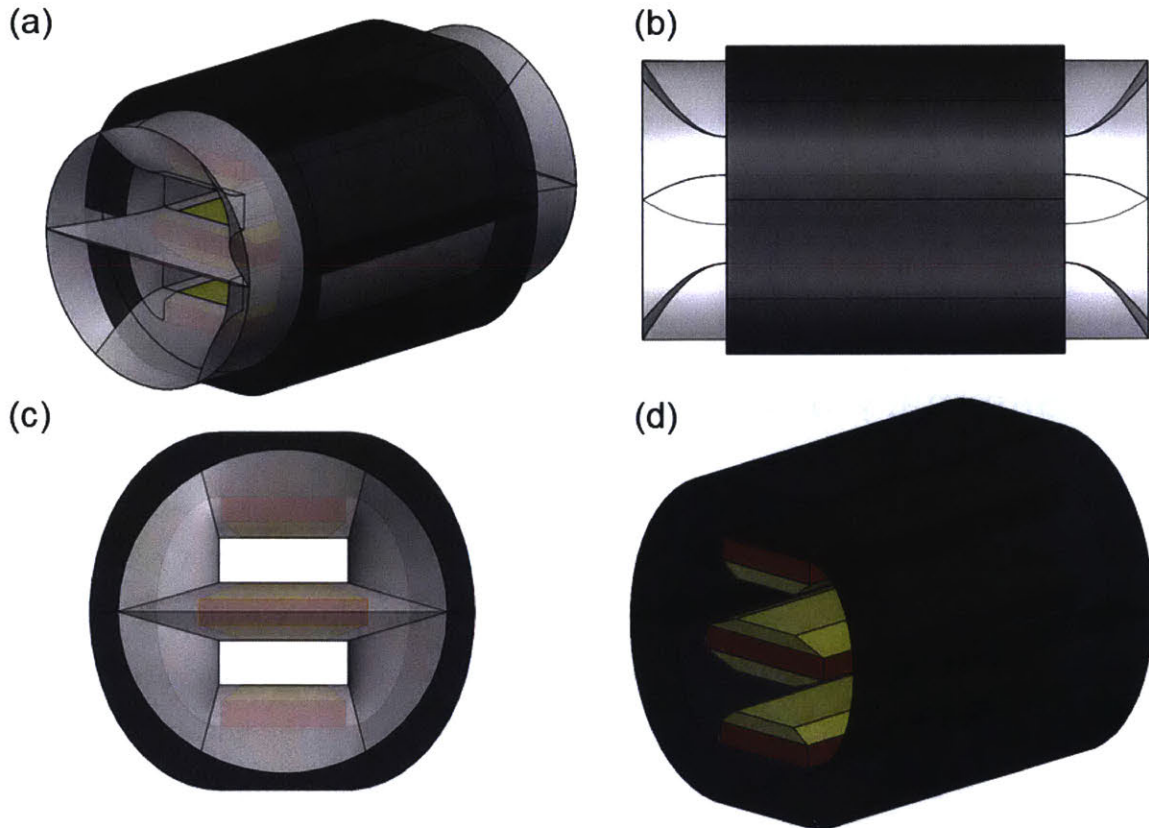


Figure 5-1: Final design. (a) overall view; (b) side view; (c) front view; (d) magnets and concentrators.

Given the large size of the loop proposed, the method to install the energy harvester into the water distribution system is also well considered. The maximum diameter of the channel wall (the light grey part in Figure 5-1) is exactly the same

as the pipe. Thus, the part of the channel wall out of the concentrator loop can be inserted into the pipe and sealed with pipe glue. In this way, the size of the loop is not constrained by the pipe size, and the optimizational performance can be achieved.

Due to the existence of surface curvature, the electrodes are replaced by conductive coating to better fit and cover the curved surface. Three materials from MG Chemicals, namely silver, carbon and nickel, are tested on a 3D printed test plate, which is shown in Figure 5-2. The details of the three materials are shown in Appendix C.

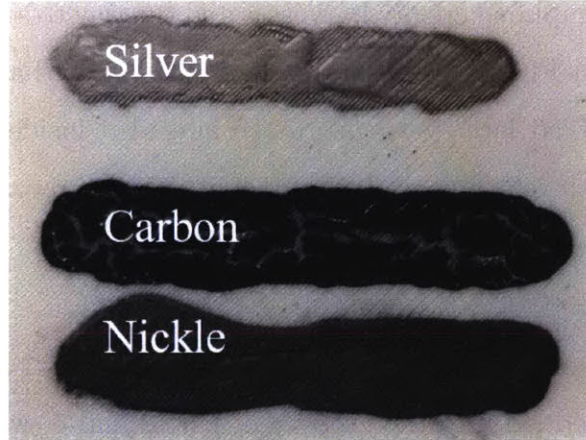


Figure 5-2: Material test of the conductive coating.

After the test, the silver coating is the only suitable material for this application. The carbon coating cracks after drying, and the nickel coating is water-based, which will be dissolved in high pressure and high velocity flow. Moreover, the silver coating can achieve a much lower resistance when measured from two ends of the channel, which makes the error of load resistance smaller. Thus, the silver coating is adopted.

The other two surfaces of each channel are coated with Smooth-on XTC-3D coating to reduce the wall roughness caused by the inherent characteristics of 3D printing. The information of the coating material is shown in Appendix C. In the future, other advanced material like hydrogel can replace the coating to achieve even lower friction on the water flow [23].

5.3 Fabrication

Given that the high permeability property of mu-metal requires the material to be annealed after machining and the shape of the concentrator is very complex, the proposed concentrator is not fabricated yet. Thus, a simplified version of the energy harvester without the inner concentrators and the loop is fabricated and tested here first.

The magnets are embedded inside the energy harvester, and the surfaces of the channel need to be specially coated, which both raise challenge on the fabrication process design. The simplified energy harvester and the way to segment it for an easier assembly are shown in Figure 5-2. Each part of the energy harvester is 3D printed separately and assembled later with magnets embedded insides. And all the parts are connected with screws, which allows magnet change, repair, and maintenance. The nickel coating on the magnets is rustproof in the water. Thus the rust-proof treatment on the magnets is not required.

Four magnets with size of $50.8 \text{ mm} \times 12.7 \text{ mm} \times 3.2 \text{ mm}$ (2 inches \times 0.5 inches \times 0.125 inches) are embedded into the grooves of part 2 and 6, which fits the magnets perfectly. Next, part 1 and 2, and part 6 and 7 are screwed up with eight M2.5 screws. Then the Smooth-on material is coated on the channel of part 2, 3, 5 and 6; while the silver conductive coating is coated on part 2 and 6. After the coating dries out, two $50.8 \text{ mm} \times 9.5 \text{ mm} \times 3.2 \text{ mm}$ (2 inches \times 0.375 inches \times 0.125 inches) magnets are embedded into the grooves of part 4. And then all the parts are screwed together with four M2.5 screws traveling through the small tubes on part 2 and 6, which clamps part 3, 4 and 5. With the above procedures, the energy harvester is fabricated and assembled without any glue.

5.4 Experimental Setup

The energy harvester is tested at MIT Mechatronics Research Lab. The experimental setup is shown in Figure 5-4.

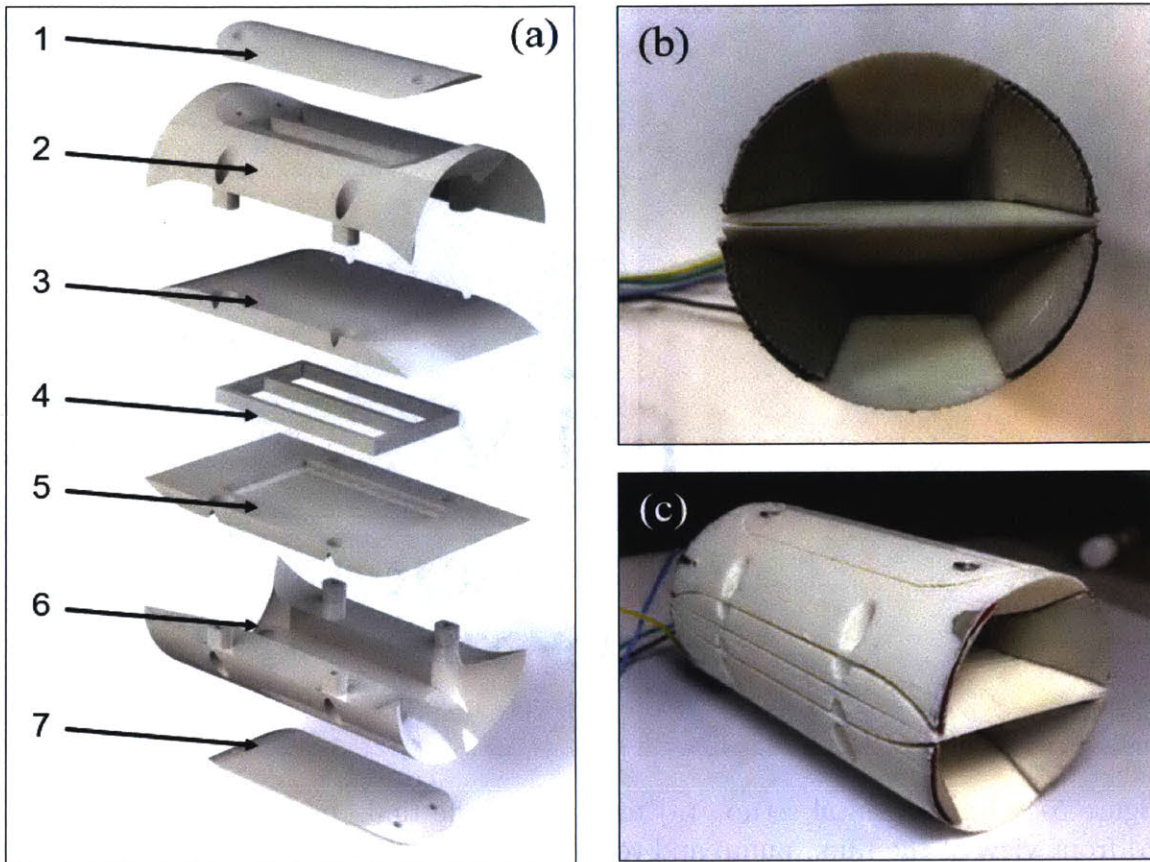


Figure 5-3: Fabrication of components and assembled prototype.

The water tank is made of polyethylene to increase the structural strength and guarantee the experiment safety. The water is pumped directly into the 2-inch pipe loop by a pump fully immersed to avoid air bubbles. And two ends of the test segment are attached with a union socket to make it easier to be removed from the loop and add the energy harvester into the segment. There is also a removable cap before the test segment to release the air bubble out of the pipe loop. Only if the water is fully filled in the pipe, the flow meter can work accurately.

The power output is very sensitive to the flow velocity, thus a flow sensor is installed. The sensor can map its wheel velocity to the flow velocity with careful calibration. But this mapping relationship only works for the fully developed turbulence. The flow within the pipe is required to meet the standard that the Reynolds number is greater than 4000. Moreover, the sensor also requires the turbulence to fully develop and this progress is prolonged by the 2 90° elbows, thus the sensor requires the

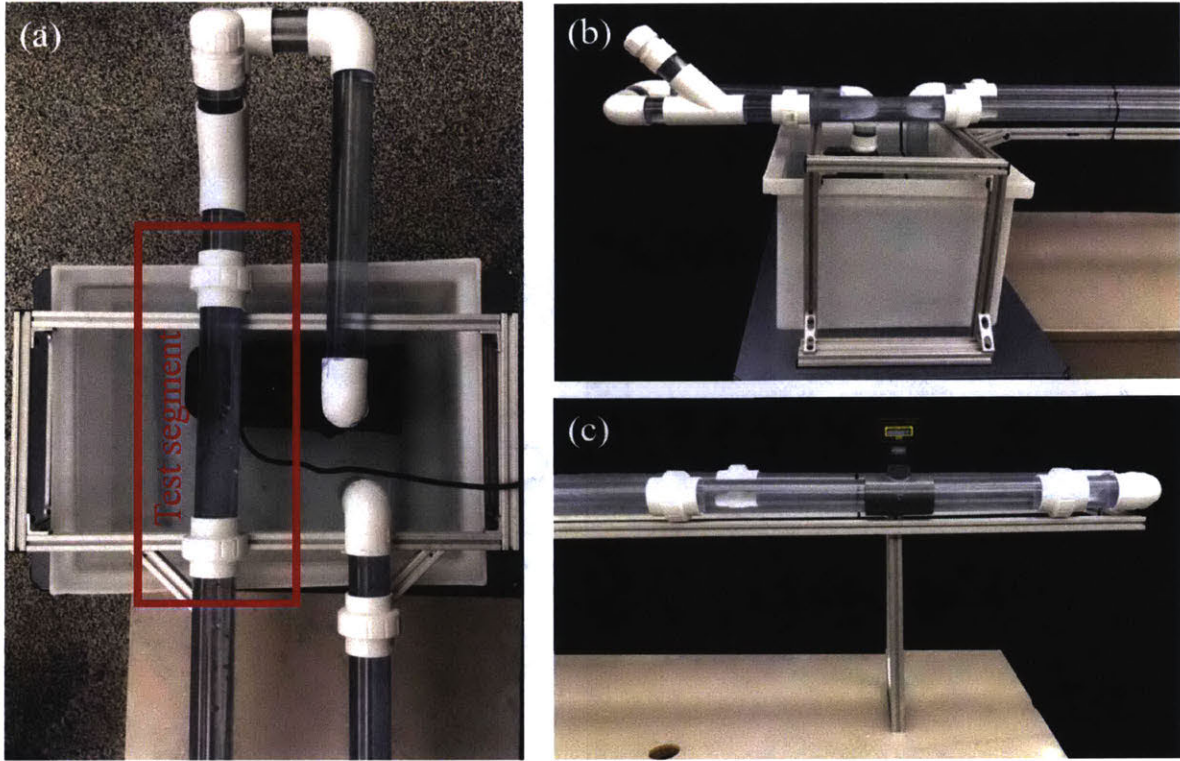


Figure 5-4: Experimental setup. (a) top view of the tank, pump and test segment; (b) front view of the tank, pump and test segment; (c) flow meter 2 m after the pipe elbow.

length of the straight pipes before and after the sensor to be 40 times and 5 times of the pipe inside diameter, respectively. Thus, the distance between the flow sensor and the upstream 90° elbow is 2 m. And the sensor is 0.3 m before the downstream elbow. The conductivity of water is measured with a conductimeter. The magnetic flux density is measured with a Gauss meter.

Since the force from the flow acting on the energy harvester is very strong, eight holes on the pipe are drilled. And eight 6mm M2.5 screws are screwed into the holes and form eight small obstacles to stop the energy harvester at its position. And the two strong magnets are placed outsides the pipe after all the above procedures are finished to strengthen the magnetic flux density and the power output for better measurement. The magnetic amplification factor between the tested case and the final design is 1.275 according to the simulation results, which can be used to calculate the expected power output with the concentrators.

The electrodes are connected to an outer load resistor. And the voltage between the resistor is measured by an oscilloscope to calculate the power output. The pump is turned on first. After the flow is steady and there's no bubble inside, the power is turned off. The voltage jump, after the pump is turned off, is the voltage produced by the energy harvester and extracted by the load resistor. Thus the voltage difference is obtained and the power output under various load resistance can be calculated.

5.5 Experimental Results

The flow rate during the experiments under different load resistance is constant, with a value of $0.00278 \text{ m}^3/\text{s}$ (44.0 gallons per minute), corresponding to the flow velocity of 9.93 m/s in the channel and 1.36 m/s in the pipe, respectively. The conductivity of water is measured at the temperature of 23.1°C after three times of pre-rinse with the sample water. The conductivity of water from the experiment tank is 0.0810 S/m. The magnetic flux density within the channel is measured with a Gauss meter to be 0.229 T. When measuring B , 7 positions along the x-axis from one end of the channel to the center of the channel, and three positions along y-direction for each x are chosen. The 21 points are measured for three times each, and the results are averaged to get the magnetic flux density within the channel.

The theoretical power output can also be calculated using Equation (2.4) with the value of $B=0.229 \text{ T}$, $u=9.93 \text{ m/s}$, $L=0.0508 \text{ m}$, $b=0.020 \text{ m}$, and $h=0.014 \text{ m}$ for two channels in total. The experimental results and the calculated results are shown in Figure 5-5.

The theoretical maximum power output occurs at the resistance of 637Ω according to Equation (2.4), and the optimal resistance in the experiments is around 700Ω , which are very close. The maximum experimental output is 442 nW, while the maximum theoretical output without hall effect is 586 nW.

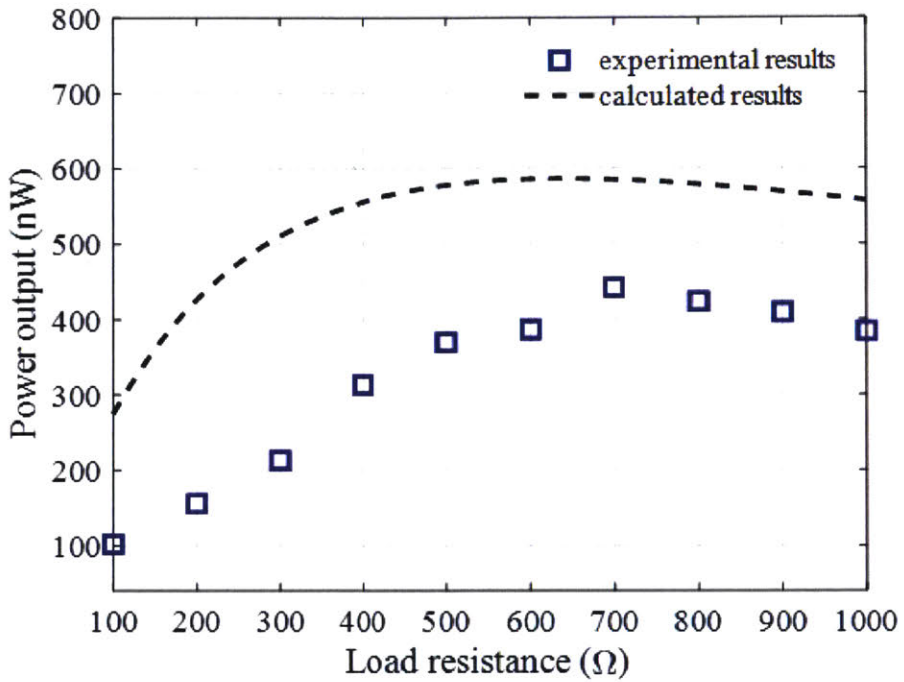


Figure 5-5: Experimental and theoretical power output with various load resistance.

5.6 Discussion

The experimental results and the theoretical results show the same trend that the power output decreases when the resistance increases from the optimal resistance. The voltage output in the measurement always increases with the resistance; however, the large resistance eliminates the power output during manipulations. Based on the discussion above, the theoretical model using the generalized Ohm's law in the Chapter 2 is validated, and the design methodology based on that in the following chapters is also verified.

The difference between the two results may come from 3 sources:

- 1) Hall effect. The hall effect described in Chapter 2 is not considered in the whole design process. Although it may not shift the results too much and can be neglected to simplify the design analysis, it can still cause a difference in the results to some extent.
- 2) Measurement error. Since both flow velocity and magnetic field B have a quadratic contribution to the final results, the measurement error of these two pa-

rameters can cause a huge error. The flow velocity is measured with a flow meter, and the results are quite consistent during all the experiments. But the magnetic field can be more complicated. Several points along x-axis and y-axis are chosen to be measured, but the z value of these points does not vary. Moreover, the magnetic field distribution is not linear itself, which means the average of the measurement results can't reflect the mean value of B among the space.

3) System nonlinearity. The relationship described in Equation (2.5) is non-linear. Thus, the average manipulation of the parameters may cause an additional error. Moreover, the surfaces of the electrodes are curved, which also introduce the non-linearity to the system. Since u and B at the transition period are both much lower than the value in the water channel part, the transition part is excluded from the calculation to eliminate the non-linearity. But this still introduces errors caused by the simplification.

After considering the amplification factor of the magnetic field with the concentrator, the magnetic flux density in the channel can reach 0.292 T, which will increase the power output to 718.5 nW. However, the power output can be further improved by the following methods:

1) Stronger magnets. The permanent magnets used in the prototype are already very strong, but even stronger magnets can be found and adopted on the market or in some labs. However, these magnets are not adopted in this thesis considering the safety issue. And they will not help with the design methodology.

2) Segmented electrodes. Although hall effect may not influence the energy harvester tested in this thesis dramatically, the Faraday energy harvester may still suffer from the Hall effect when the lengths of the electrodes are very long. However, the Hall effect can be eliminated by replacing the long electrodes with segmented electrodes along the flow direction, based on the discussion in Chapter 2. However, this requires a much more complicated fabrication process, which may be easy for industrial production after commercialization, but not in the lab.

3) larger dimension. According to Equation (2.5), the power output is proportional to the channel volume. The size of the prototyped energy harvester is limited by the

experimental setup. But it can become much larger in the real scenario, and it will increase the power output dramatically.

After considering these factors, the energy output can be easily increased to microwatt level or even milliwatt level.

5.7 New Concept with a Spiral Flow Diverter

5.7.1 Problem description

After the energy harvester with a three-layer magnet is prototyped and tested in lab, a new and higher requirement is raised that the energy harvester does not block the flow any more and there's a hollow area with the same size as the pipe on the harvester to allow the robot and/or the flow to pass through. The basic idea is that the energy harvester can be designed as an add-in section between two pipes, just like a joint. And thus the size of the energy harvester is not limited by the pipe, and it only requires that the ends of the energy harvester can be connected to the pipe system. In this case, a hollow area in the middle can be made and the channel to harvest energy can be placed outsides this hollow area. And the round channel can be separated into four sections, each with two electrodes to collect charges. With some careful analysis, the transition part between the pipe and the section with much larger diameter should be very gradual to allow the flow to fully expand to a larger diameter. The transition between the channel exit and the downstream pipe also should have a gradual change of the diameter to reduce the resistance of the wall to the flow. This preliminary design is shown in Figure 5-6. The gold parts are the electrodes, the blue parts are the magnets inside and outside to generate a magnetic field perpendicular to the flow velocity. And the four parts surrounded by the electrodes and magnets are the four flow channels.

However, with this design, the flow will tend to flow through the hollow area smoothly, and thus only a small part of the flow will go through the channel around the hollow area.

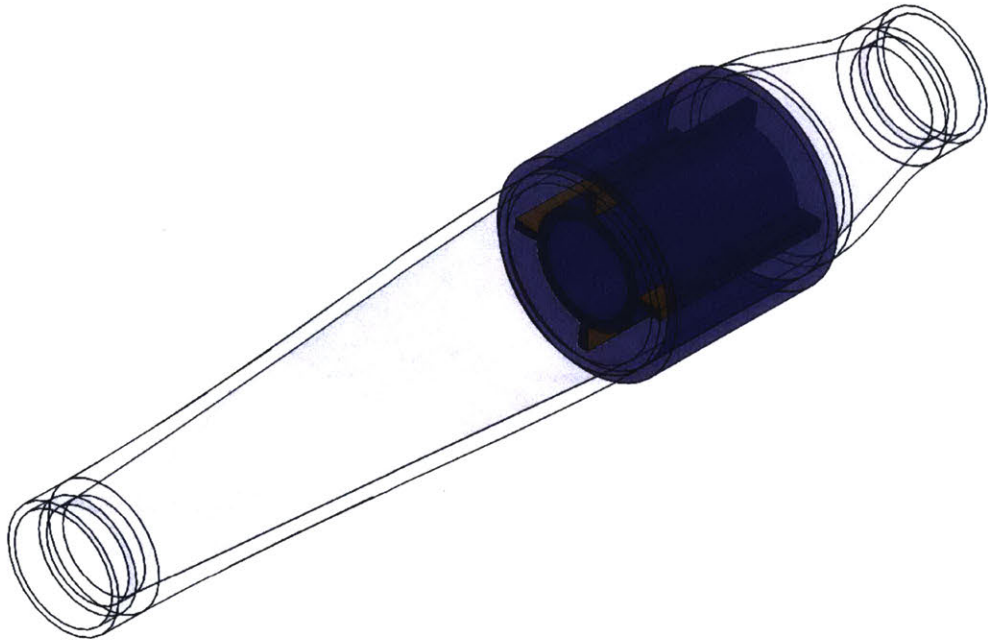


Figure 5-6: Preliminary design of the energy harvester with a hollow area in the center.

5.7.2 Design of the spiral flow diverter

To solve this problem and increase the flow velocity within the channel, a new spiral flow diverter composed of four spiral flow guides, one ring turbulence inducer, and a twist flow channel is proposed. And the design is shown in Figure 5-7.

In the figure, the red component is the spiral flow guide, which is to induce a cyclone within the energy harvester which can dramatically increase the pressure at larger diameter and this pressure can push the flow into the channel. Moreover, this cyclone can destroy the original flow pattern and help reform a new flow pattern to better adapt to the geometry change. The spiral guide should also adopt a gradual increasing pitch to reduce the resistance and block of the spiral guide onto the flow. In the figure, the pitch changes from 400 mm to 1,600 mm.

The blue components are the magnets, while the gold parts are the electrodes. The magnets and the electrodes form four spiral water channels, where the energy harvester functions and generates power output. With this design, the magnets are the same as the ones in the preliminary design, since the magnetic field required in

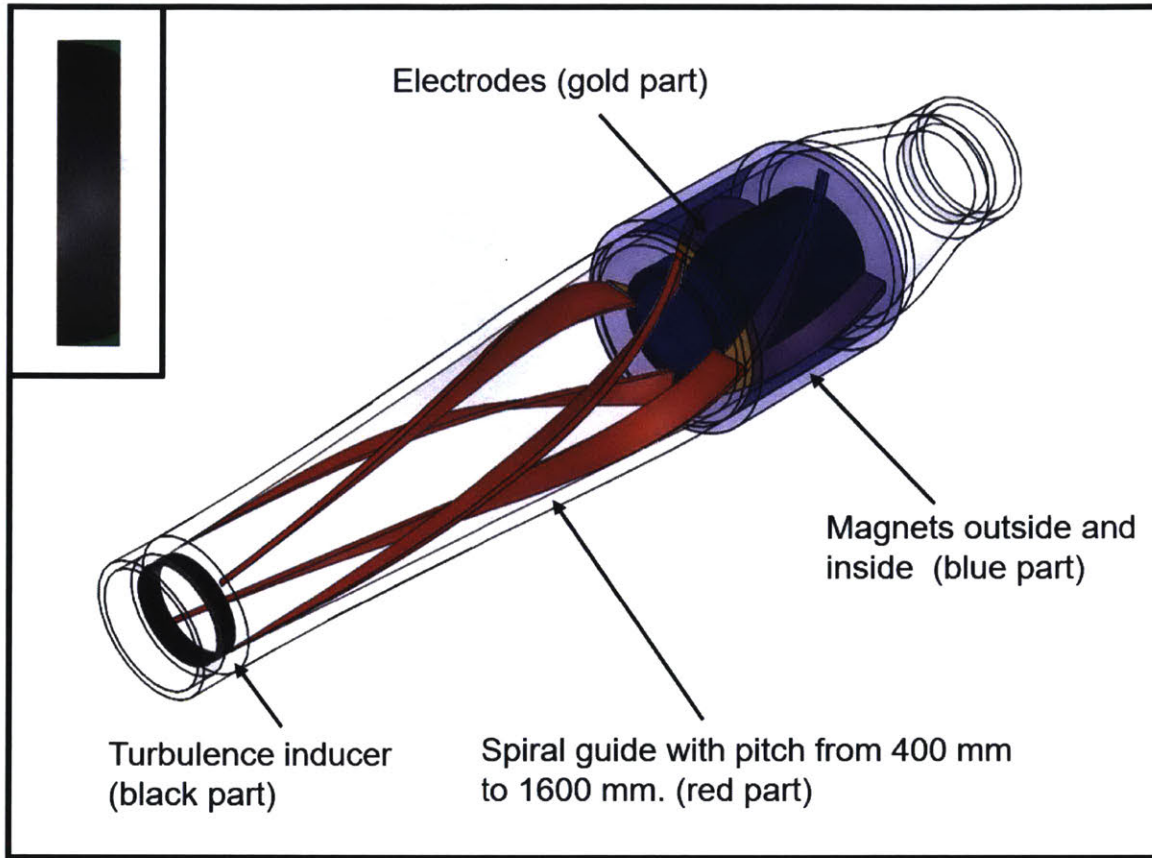


Figure 5-7: Design of the spiral flow diverter and cross section of the turbulence inducer.

these two designs is the same. The spiral channel can reduce the energy loss when the flow entering the channel and keep the flow rotating within the channel. And when the flow is to exit the channel and be shrunk into the normal pipes, the resistance introduced by the spiral flow on the flow behind is much lower than the straight flow.

And a small turbulence inducer, which is shown as the black component in Figure 5-7, should also be installed at the energy harvester inlet to help break the original flow pattern and reform a new one which quickly adapts to the new geometry.

5.7.3 Validation of the design

To validate the effect of the spiral flow diverter, the preliminary design and the spiral flow diverter are both simulated with ANSYS Workbench R19.2. The length of the pipe before and after the energy harvesters are set to be 0.2 m and 0.5 m to allow

the flow to fully develop. And the meshes established are shown in Figure 5-8. The inlet boundary condition is set to be 20,000 Pa pressure inlet, while the outlet is set as 0 Pa pressure outlet.

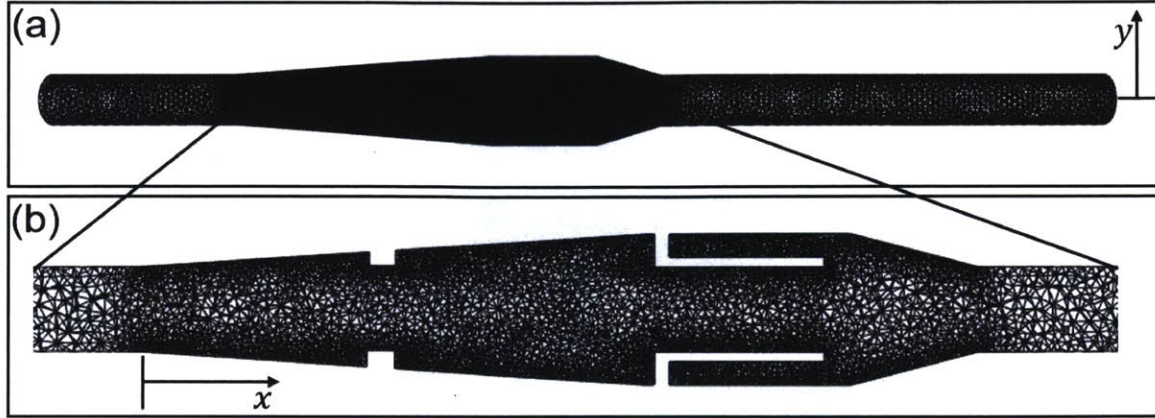


Figure 5-8: Mesh for spiral flow diverter case. (a) overview; (b) zoom-in view on slice of $y=0$ m (middle plane).

The pressure contour of the two cases are shown in Figure 5-9.

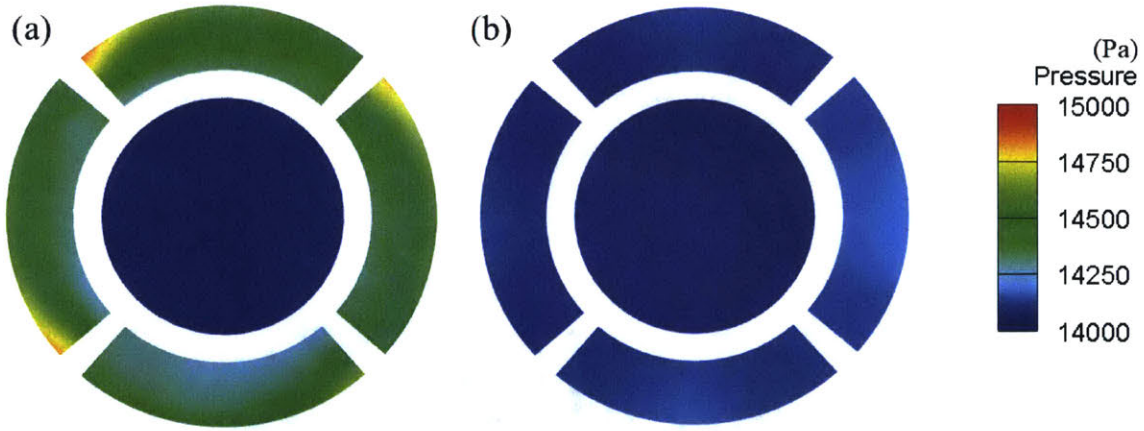


Figure 5-9: Pressure contour at $x=0.39$ m from the energy harvester inlet for the case (a) with spiral flow diverter; (b) without spiral flow diverter.

In Figure 5-9 (a), the pressure within the channel outside the 2-inch hollow area is much higher than the pressure in Figure 5-9 (b). But the opposite results appear in the hollow area. The pressure distribution without the spiral flow diverter is much more symmetrical, while the pressure for Figure 5-9 (a) highly depends on the angular

position of the point. Moreover, in Figure 5-9 (a), the pressure increases with the diameter of the point in the channel due to the existence of the spiral flow, which is shown by the streamlines in Figure 5-10. And it is also observed that the streamline without the spiral flow diverter changes sharply by the thickness of the channel wall at the channel entrance point.

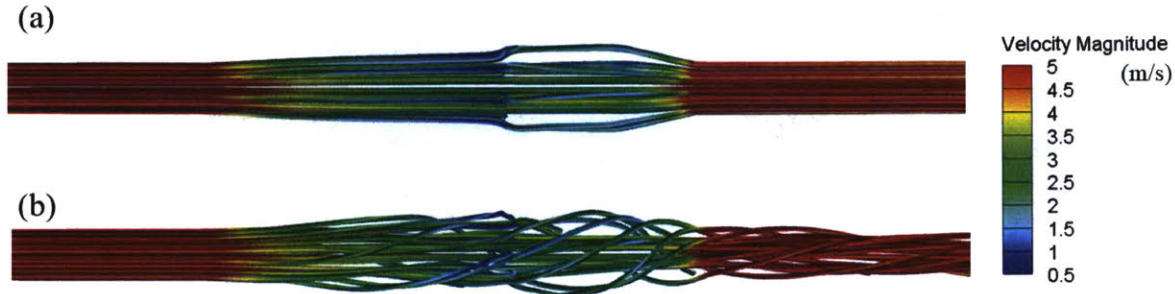


Figure 5-10: Streamline for the case (a) without spiral flow diverter; (b) with spiral flow diverter.

Thus, the effect of the spiral flow guide to cause the cyclone and higher pressure at the channel entrance is validated. According to this, the flow velocity within the channel should also be larger. The velocity contours at the slice $x = 0.39$ m from the energy harvester inlet are shown in Figure 5-11.

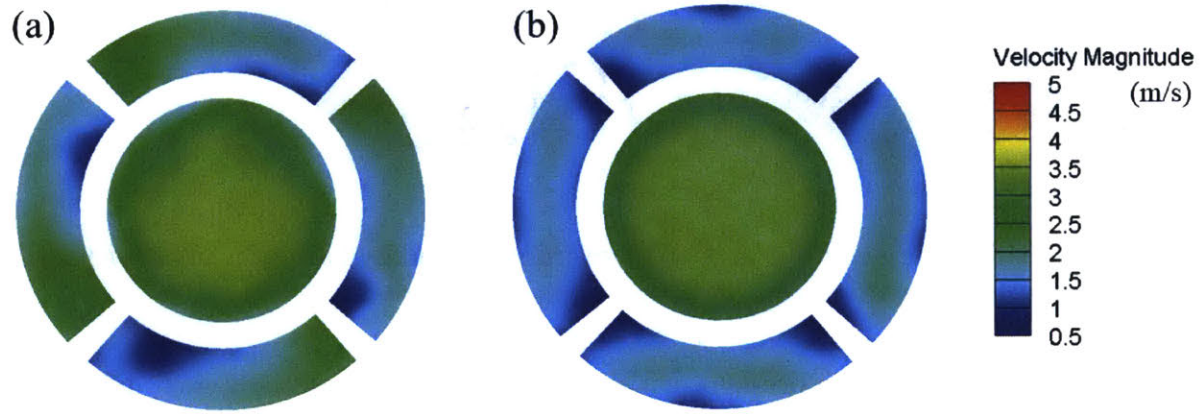


Figure 5-11: Velocity contour at the slice $x=0.39$ m from the energy harvester inlet for the case (a) with spiral flow diverter; (b) without spiral flow diverter.

The velocity in the channel with the spiral flow diverter is much higher. And the velocity magnitude also highly depends on the angular position of the point, which is very similar to the pressure results. Since the flow rotates counterclockwise, the velocity increases as a point moves counterclockwise within one specific channel. The max velocity in Figure 5-11 (a) reaches a 2.67 m/s, while the maximum velocity in Figure 5-11 (b) is only 1.86 m/s. This velocity distribution difference is much more obvious on slice $y=0$ m (middle plane), which is shown in Figure 5-12.

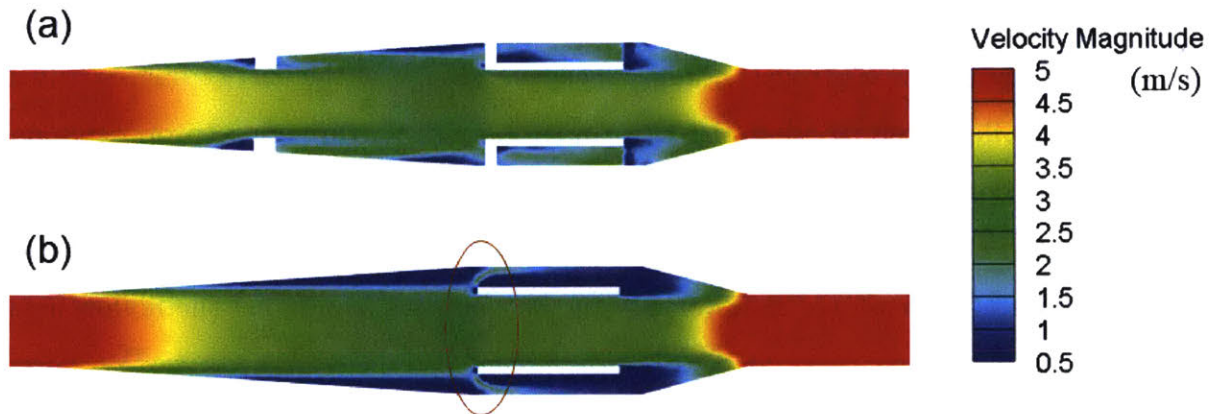


Figure 5-12: Velocity contour at the slice $y=0$ m (middle plane) for the case (a) with spiral flow diverter; (b) without spiral flow diverter.

In Figure 5-12 (b), flow without the spiral flow diverter separates sharply at the wall of the channel into two streams, which may cause a high form resistance on the flow. And the original flow pattern in the pipe remains in energy harvester, causing there's only a little part of the flow goes into the channel. On the contrary, the transition between the flow guide and the channel wall is completely smooth, and the original flow pattern is broken and a wider flow is quickly formed in Figure 5-12 (a).

The power output for this concept design is expected to be 238.3 nW, with the flow velocity of 2.0 m/s in the channel, the water conductivity of 0.810 S/m, the flow channel volume of 3.3×10^{-5} m³, and the magnetic flux density of 0.42 T with the use of the concentrator.

5.8 Summary

After the analysis in Chapter 2, 3, and 4, a final design with a 10 mm width concentrator loop, inner concentrators, a three-layer magnet, and two flow channels is proposed. A simplified version of the energy harvester without the concentrator is prototyped and tested in the experimental setup in the lab. And the maximum experimental power output is measured to be 442 nW occurring at 700Ω , which is very close to the theoretical results. With the use of the concentrators, the maximum power output can be expected to be 718.5 nW. The error source between the experimental results and the theoretical results, and the methods to further improve the power output are carefully discussed. Moreover, a new conceptual design of the energy harvester with a 2-inch hollow area to allow the flow and robots to go through is proposed. And the spiral flow diverter, including the spiral flow guide, turbulence inducer, and a spiral water channel, is come up with and validated to induce a cyclone in the energy harvester and increase the flow velocity in the channel surrounding the hollow area.

Chapter 6

Conclusion and Recommendations

6.1 Conclusion

In this thesis, an MHD energy harvester combining a magnetic concentrator is proposed and optimized based on theoretical modeling governing the power output and simulations in both magnetic field and flow field. The three-layer magnet structure and the mu-metal magnetic concentrator composed of a 10 mm width loop and inner concentrators are validated to optimally increase the magnetic flux density in the flow channel. In the flow field analysis, the channel height should balance the block effect on the flow and the distance between magnets. For a 2-inch pipe, a channel height of 7 mm is determined. A simplified version of the energy harvester without the concentrator is prototyped and tested in the lab. And the max power output is 442 nW occurring at around 700Ω , which is very close to the theoretical power output and optimal load resistance. Thus the theoretical model and the design methodology are both validated. The power output with the use of the concentrator can be expected to be 718.5 nW.

Another conceptual MHD energy harvester with a spiral flow diverter and a hollow area the same as the pipe cross section is proposed. It is validated with CFD simulations, that the spiral flow diverter can dramatically increase the flow velocity within the channel and break the original main flow pattern to make the flow quickly adapt and expand to the gradually increasing diameter.

The power output of the MHD energy harvester proposed and tested in this thesis shows great potential to fulfill the energy requirement of new wireless sensor nodes developed specifically for the intelligent pipe system. And the power output can be further amplified in practical use where the scale of the energy harvester is much larger. The methodology proposed and validated in this thesis can provide helpful guidance for future MHD energy harvester design for specific working conditions.

6.2 Recommendations

This thesis shows the huge potential of such an MHD energy harvester. But several recommendations are also proposed to further improve the results, adaptability, and feasibility of the idea.

Firstly, it is desired to develop the technique to increase the water conductivity without polluting the water. The energy harvester works in the water distribution system, thus it is difficult to seed the water. However, if the conductivity of water can be increased within a given region or the particle can be retrieved before the end user, it would greatly benefit the power output.

Thirdly, with the technique of room temperature superconductors, the magnetic flux can be further constrained, in addition to the guidance effect of high permeability material. And the power output can be greatly improved.

Appendix A

Effect of the Inner Concentrator

Since the inner concentrator is much closer to the flow channel. Thus the influence of the inner concentrators on the magntic flux density in the channel is investigated in this chapter. And several parameters of the inner concentrators are discussed.

A.1 Relevant Parameters

The concentrator can replace the wall between the magnets and the water channels since the metal we use here can also support the structure and protect the magnets. The geometry of one of the simulation cases and the parameters are shown in Figure A-1. c represents the width of one end of the concentrator, while the other end is connected to the magnets, and thus has the same length as the magnets. b is the width of the water channel. And the other two parameters are the height and the material of the concentrator.

In the series of the simulations, b varies from 5.0 mm to 35.0 mm with an interval of 5.0 mm; c varies from 4.0 mm to 19.0 mm with an interval of 3.0 mm; the height of the concentrator is set to be 2.0 mm or 8.5 mm; and the materials of the concentrator can be mu-metal, Permalloy, pure iron annealed, or air (without a concentrator).

The 2.0 mm concentrator height is the reasonable wall thickness to support a structural load, while 8.5 mm is the max possible wall thickness limited by the size of the pipe. The height of the concentrator can influence the results in two conflict

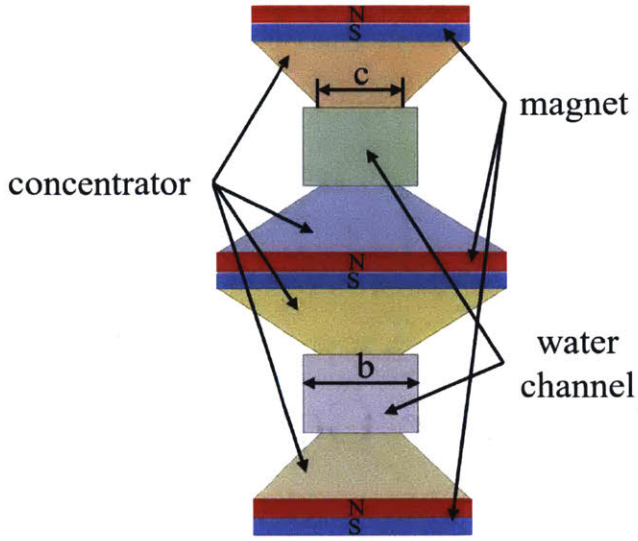


Figure A-1: Concentrator geometry and parameters.

ways so that this parameter is also varied in the simulation. On the one hand, the larger distance between magnets will decrease the magnetic field. While, on the other hand, the larger height allows a more gradual change of the width of the concentrator to reduce the flux leak from its side surface.

The property of different materials is illustrated by B-H curves. And the curves for the three metal materials are shown in Figure A-2. The saturation of different materials can be ranked clearly with (a), while the zoomed in view (b) shows more details on the permeability. At the reasonable H range, the permeability of mu-metal is the highest, followed by permalloy, and pure iron annealed in sequence.

A.2 Simulation setup

Simulations in this section are run on ANSYS Workbench R19.2 with the magnetostatic module and the design module. With the help of the design module, the parameters concerned can be changed automatically, and series simulations can be finished without manually changing the parameter or the geometry. Thus, the simulations are dramatically simplified. There are 266 cases run first, and 28 more special cases are run later to draw more comprehensive conclusions.

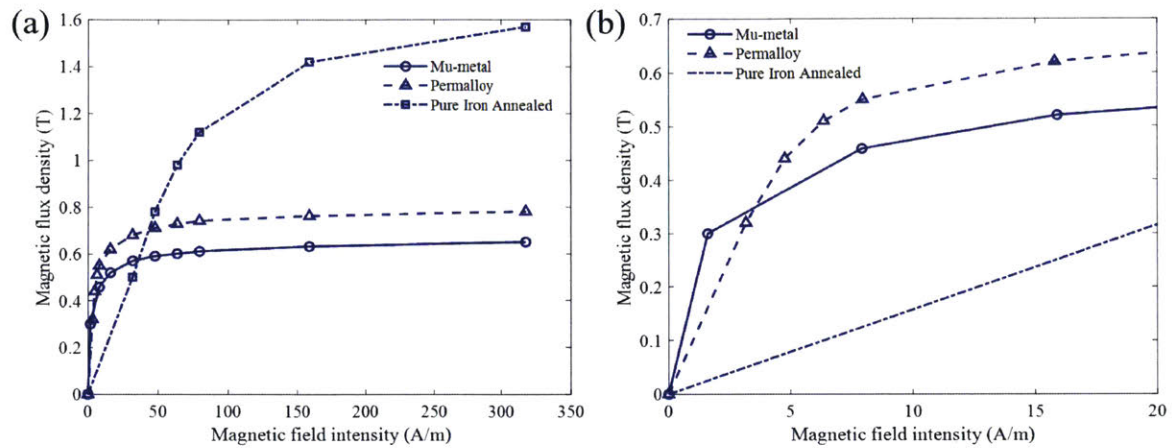


Figure A-2: B-H curve of the metarials.

The magnet material used for simulation here is the N42 grade Neodymium with the demagnetization curve shown in Figure A-3. A residual induction of 1.309 T is observed.

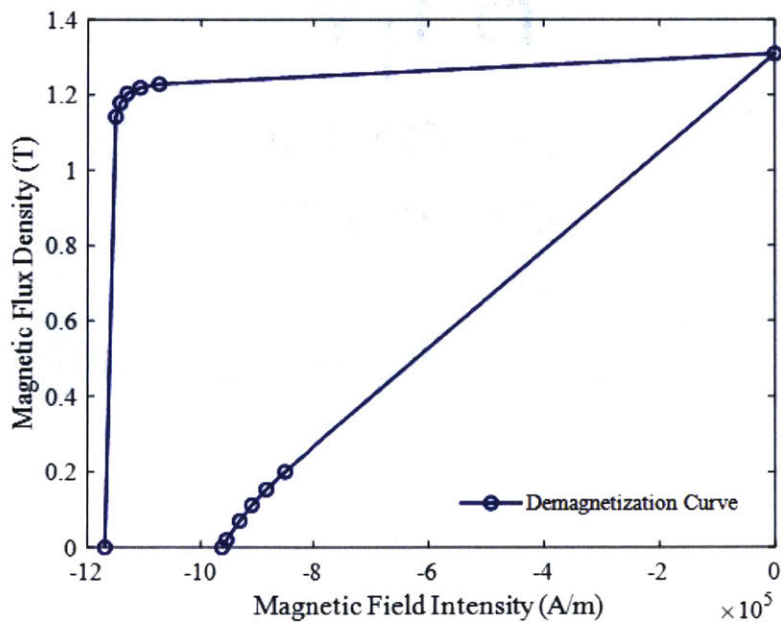


Figure A-3: Demagnetization curve for N42 grade Neodymium magnets.

A.3 Simulation results and discussions

The effect of the concentrator is first validated and then discussions about parameters are carried out based on the averaged B in the vertical direction within the water channel.

Validation

The contours of B magnitude from two cases with mu-metal concentrator and without a concentrator are shown in Figure A-4.

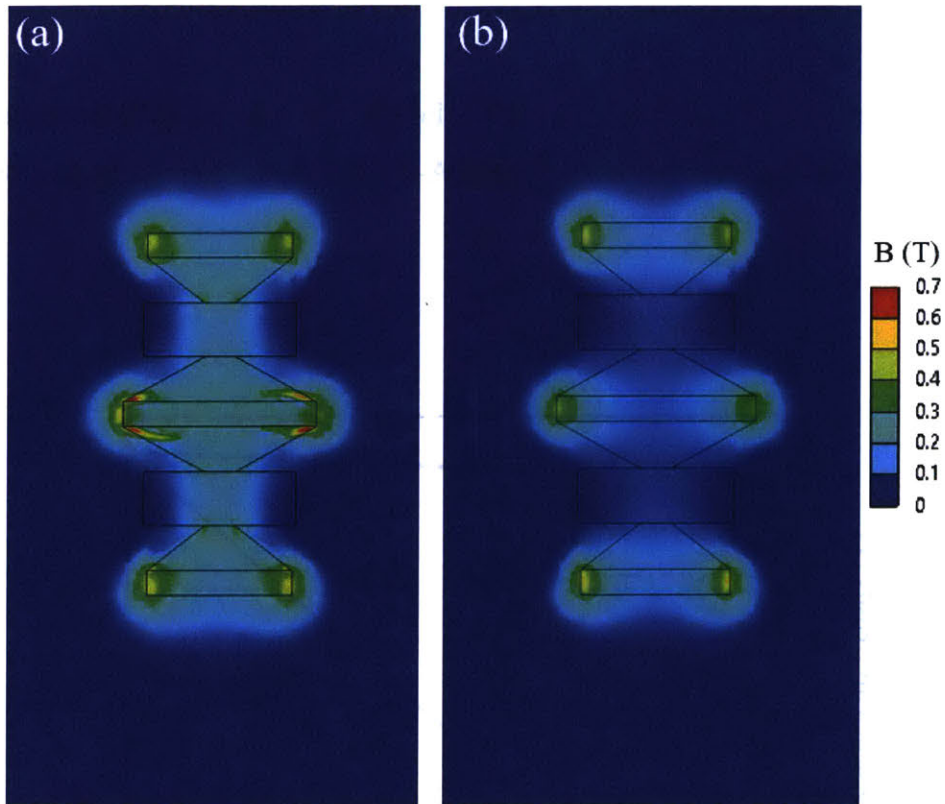


Figure A-4: Contour of B magnitude. (a) mu-metal concentrator; (b) without concentrator (material in the trapezoidal concentrator region assigned as air).

With the mu-metal concentrator, B in the background is smaller, and more magnetic flux is guided into the concentrator and the flow channel. B in the channel and the concentrator is much higher than the one without the concentrator. Moreover, it is also observed that some flux is leaked from the side surface of the concentrator,

which can be predicted. And thus the part of the channel that can be influenced is wider than c .

Since B in the direction perpendicular to both the flow and electrodes is what we concern the most, we define this direction in this section to be y -axis. And B in this direction is indicated as B_y . The contour of the two cases is presented in Figure A-5.

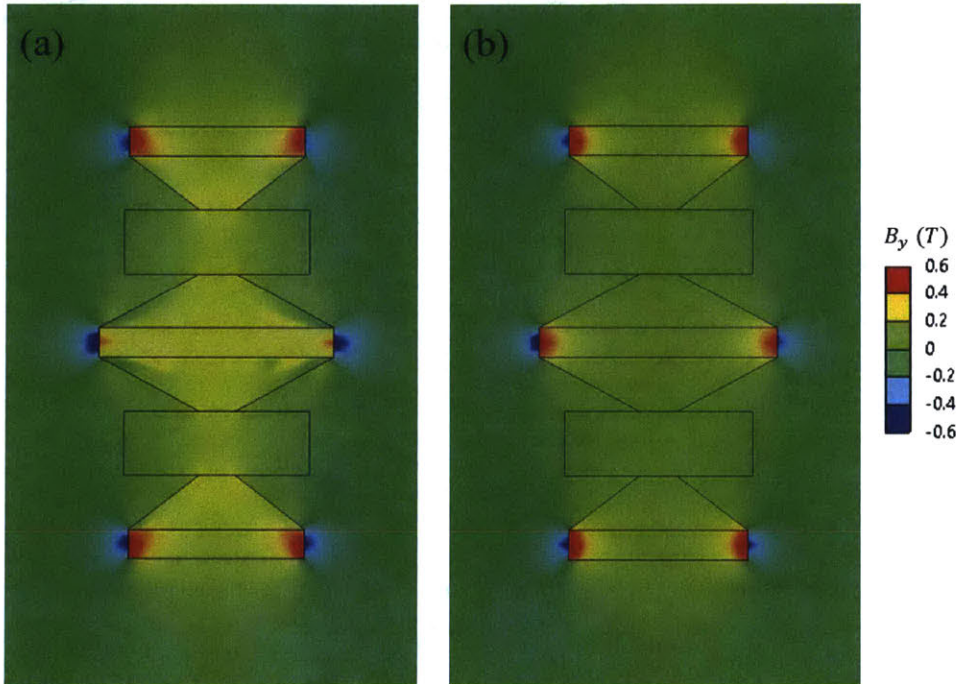


Figure A-5: Contour of directional B . (a) mu-metal concentrator; (b) without concentrator (material in the trapezoidal concentrator region assigned as air).

The same conclusion of the flux guidance and B magnification can also be drawn. Thus the effect of the inner concentrator is validated.

But it should be noticed that the working principle of the concentrator is to guide the magnetic flux. Thus if c is larger than the magnet width, B may even be weakened because of the flux conservation.

Result summary

The averaged B_y in the channel of the first series simulations are plotted in Figure A-6 for the future reference. Discussions to determine the best parameters will be conducted based on these results.

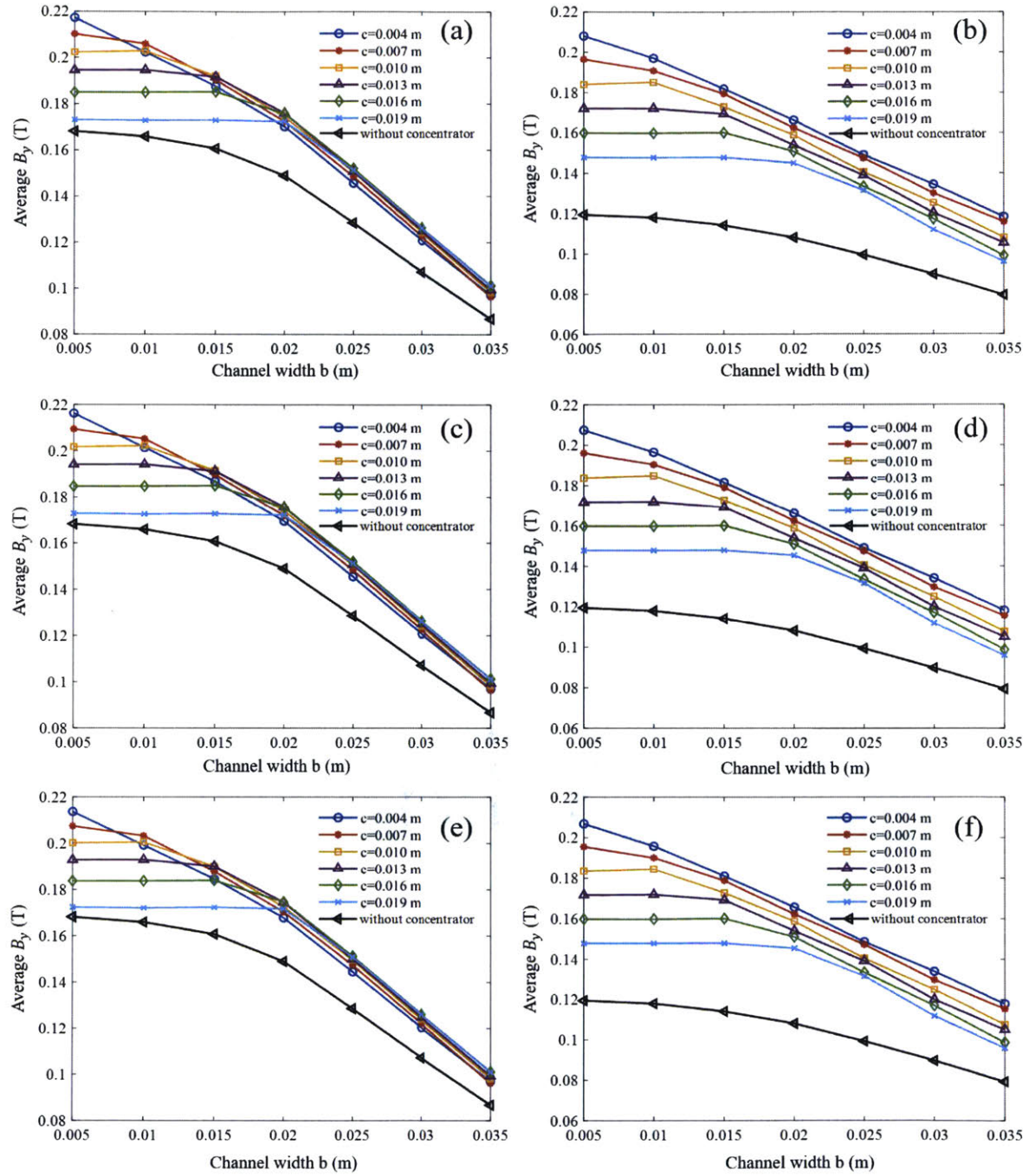


Figure A-6: Averaged B_y in the channel with the concentrator of (a) mu-metal with 2 mm height; (b) mu-metal with 8.5 mm height; (c) permalloy with 2 mm height; (d) permalloy with 8.5 mm height; (e) annealed pure iron with 2 mm height; (f) annealed pure iron with 8.5 mm height.

Averaged B_y decreases with the channel size, as B_y far away from the concentrators and the magnets is too weak. But it is also found that, when the channel size is smaller

or close to c , averaged B_y is almost the same, which means that the flux out of the concentrator is almost even along the far edge.

Moreover, the effect of the concentrator is validated again, since averaged B_y with any concentrator is bigger than the one without a concentrator, which is plotted with the black line in the figure. But in this figure, the threshold of c is 19 mm, which is the same as the width of the smaller magnet plate. When c exceeds 19 mm, the magnification may disappear.

Material selection

It can be predicted that mu-metal with a higher permeability should have a better magnification of B_y . To better illustrate the difference between various materials, the difference of averaged B_y between mu-metal and other materials are calculated and contoured in Figure A-7. The positive values mean mu-metal is better, while the negative values mean the other material can achieve higher B_y .

All the differences calculated are positive. Thus, mu-metal should be selected no matter what geometries of the concentrator and the flow channel are adopted. It can also be further predicted that material with higher permeability is always desired.

Concentrator height

After determining the material, the concentrator height should be determined next. In this part, only the results for mu-metal need to be processed and discussed.

For every channel size, the two max averaged B_y with 2 mm and 8.5 mm concentrator height are calculated and plotted in Figure A-8.

The line for 2 mm height concentrator drops faster, and the two lines coincide at around 0.025 m. Thus, 2 mm height concentrator should be adopted for small size channels, while the 8.5 mm height concentrator works better for big size channels.

And we could also calculate the difference between the results of 2 mm height and 8.5 mm height concentrators. And the results for channel sizes below 0.02 m are shown in Figure A-9. And all the value are positive, which means that when the

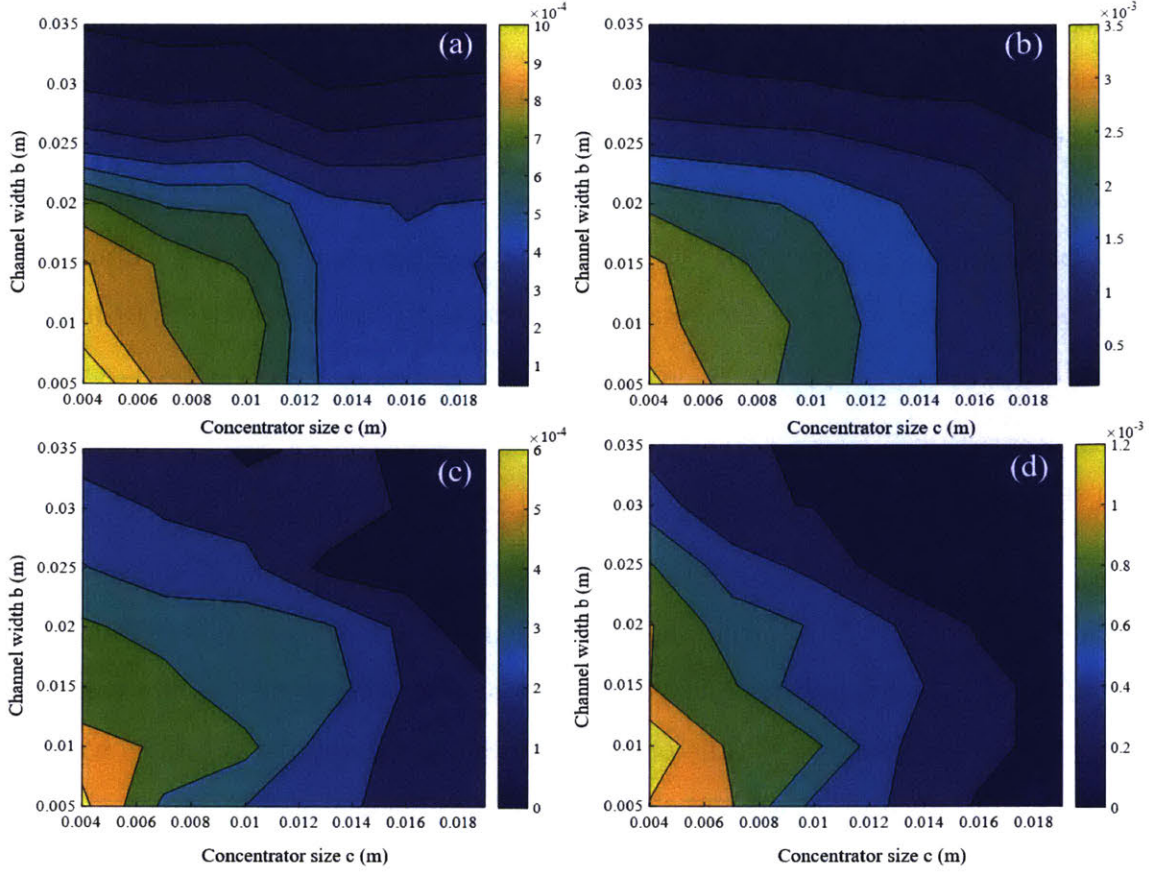


Figure A-7: Difference of averaged B_y between mu-metal and (a) permalloy with 2 mm height; (b) annealed pure iron with 2 mm height; (c) permalloy with 8.5 mm height; (d) annealed pure iron with 8.5 mm height.

channel size is small, the 2 mm height should be adopted no matter the concentrator size c .

Moreover, the concentrator size s for series simulation with 2 mm concentrator height is extended to 31 mm, still with an interval of 4 mm. And the whole results are plotted in Figure A-10.

When c exceeds 19 mm, the averaged B_y in the channel is even weaker than the cases without a concentrator for small size channels, since the flux near the center line is scattered widely. For large size channels, the effect for larger c is not as satisfying as that for smaller c . Thus, large c more than 19 mm shouldn't be adopted in any design. And the max averaged B_y for different channel sizes is plotted in Figure A-11.

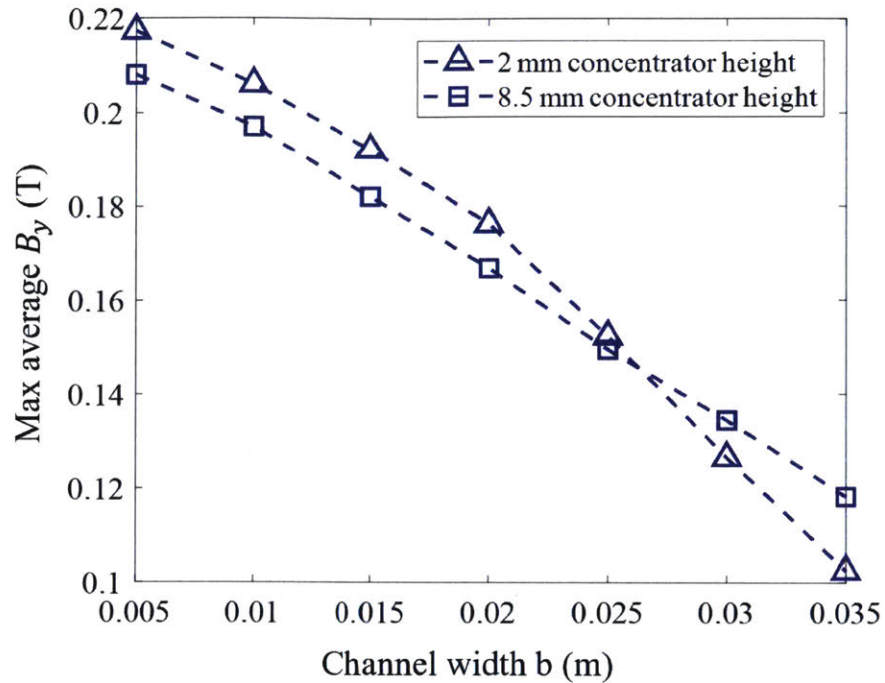


Figure A-8: Max averaged B_y for concentrators with height of (a) 2 mm; (b) 8.5 mm.

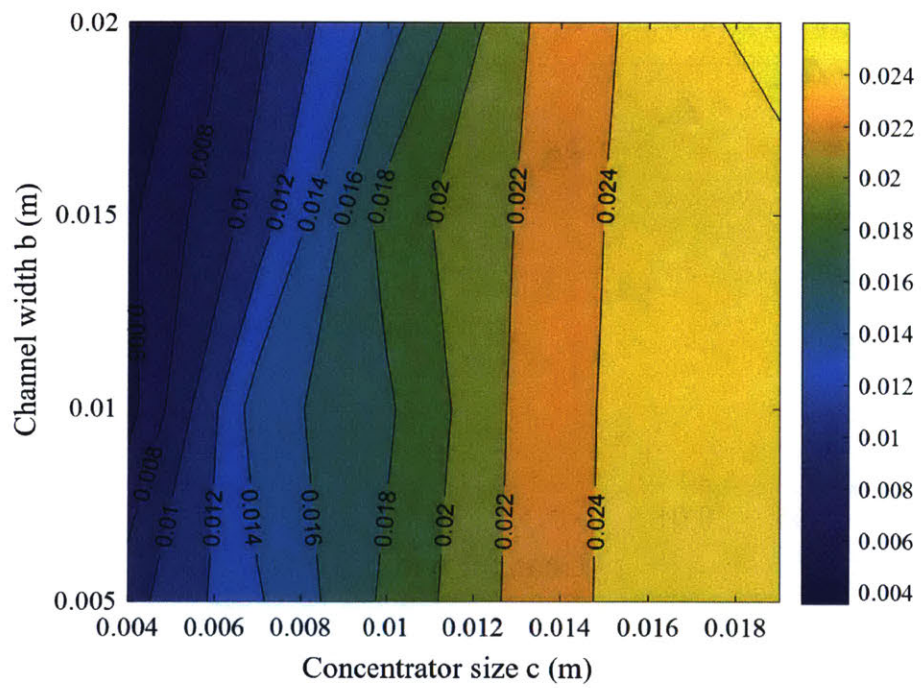


Figure A-9: Difference of averaged B_y between 2 mm and 8.5 mm height concentrators.

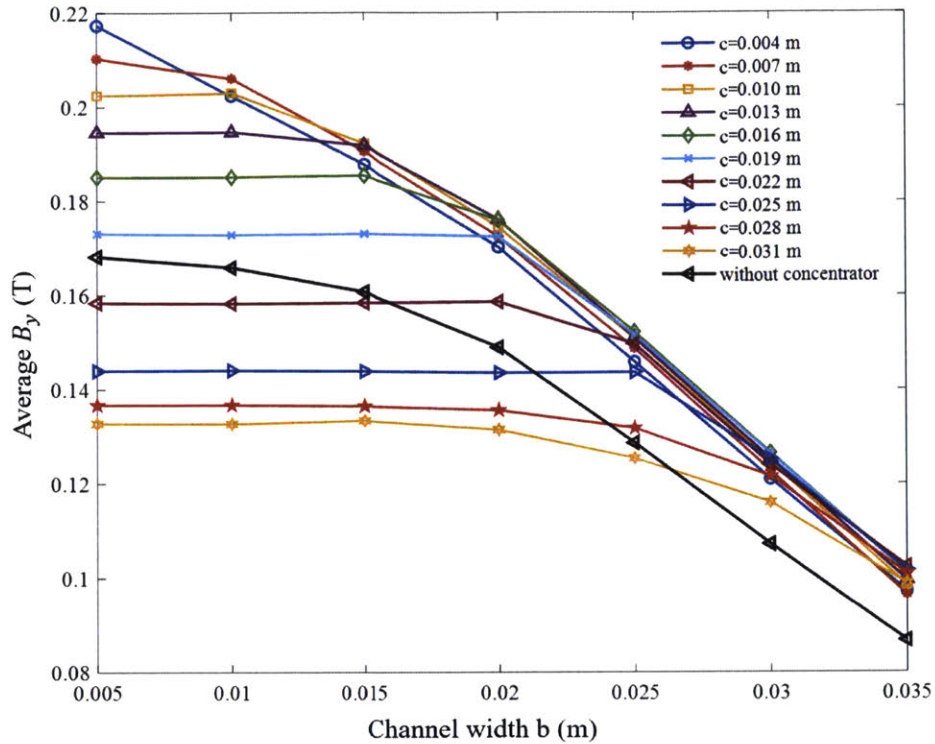


Figure A-10: Averaged B_y for 2 mm height concentrator with mu-metal.

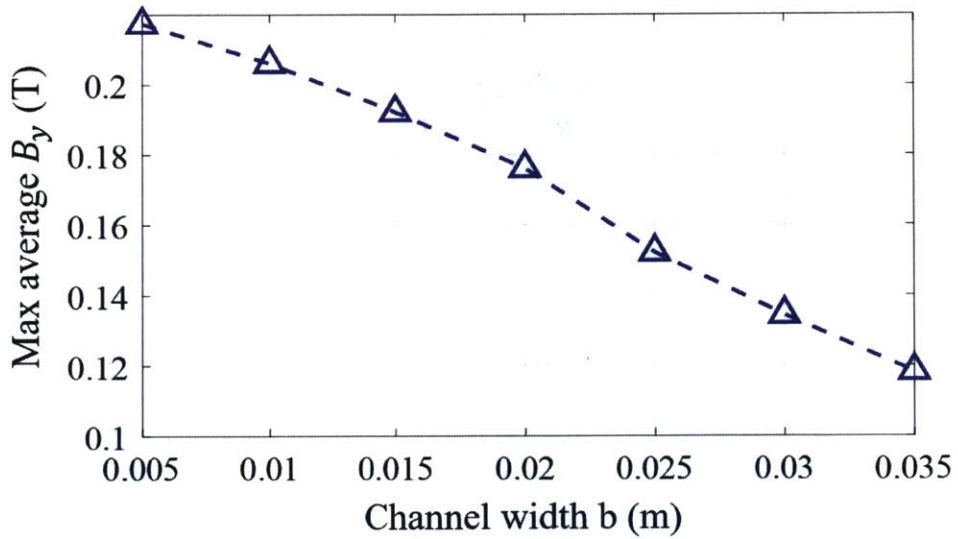


Figure A-11: Max B_y with various channel widths.

A.4 Summary

In this chapter, the concentrator without loop is analyzed carefully and simulated to investigate its influence on the averaged B_y in the channel. Several parameters,

including material, concentrator size c , and concentrator height, are discussed systematically under various channel sizes b based on simulation results. And it is found that the concentrator with high permeability can guide more flux before induction saturation, and the concentrator size c should be smaller than the magnets to amplify the magnetic flux density.

Appendix B

Concept and Validation of the New Microchannel Detector

Another contribution covered in this thesis is the concept design and validation of a new microchannel leak detector. The new kind of detector can conquer some shortcomings of the existing leak detectors. And it can also be used in not only plastic pipe network but also the metal one. The new detector works based on the same principle as the existing leak detector developed at MRL in MIT, that the leak on the pipe will cause a low pressure region. By taking advantage of this physics phenomenon, the detector can also achieve high precision localization of leaks along the perimeter of the pipe, which is crucial for the following leak repair task. This design can also dramatically increase its sensitivity and sensibility, which can be validated by CFD simulation with detecting modules still or moving. The CFD simulation with moving parts requires the OVERSET technique developed within ANSYS. Thanks to the success of this simulation case, we can easily achieve a similar simulation requiring parts to move in the future.

B.1 Previous Methods for Pipe Leak Detection

Pipe leaks can always cause severe damage and loss to the whole society. To detect and control pipe leaks in an early stage, and limit resource and economic loss, numerous

researches are focused on this problem. And lots of new technologies are developed not only for the robots moving within the pipes but also for the sensors placed on the smart pipe systems. These technologies can be categorized based on the principle it uses.

B.1.1 Acoustics Sensing

There has been a long history for human to use acoustics to detect and identify leaks above ground. A leak on the pipe will result in acoustic emission, which is especially observable for metal pipes. In the past, workers can handle an acoustic receiver and walk above the ground along the pipeline to determine where the leak is. But this method is greatly limited by the depth of the pipe and the size of the leak . Thus, in-pipe technologies based on acoustics are developed and systematically investigated in the past few years.

The signal received by the acoustic sensors on the pipeline is usually processed in two steps, where the signal feature is first extracted and then signal recognition is achieved based on that. Fourier transform, Linear Prediction Cepstrum Coefficient [24], and wavelet transform [25] can be helpful tools to extract the spectral feature of the signal. And the spectral regime features also make it possible to eliminate background noise for better leak recognition [26]. With the features obtained, a leak can be recognized by models, like maximum modulus [27], support vector machine [28, 29], neural network [30, 31], or Hidden Markov Machine [24]. And it is also possible to accomplish localization of the leaks by calculating the lag time of two signals with cross-correlation methods [32, 33].

Recently, with the advancement of MEMS technology, ultra-small hydrophones are also designed and prototyped on a small chip in the lab [34]. And the success of these sensors also demonstrates the feasibility to design a low-cost sensor network to monitor the health condition of the pipeline.

Besides fixed sensors or sensor networks, people also hope to mount these sensors on a moving robot or module to achieve a wider range covered along the pipeline. Firstly, the feasibility of using a moving hydrophone to detect the leaks is validated

with experiments [35]. And then, the influence of the line pressure, the position of sensors relative to the leak, surrounding medium, and flow velocity to the acoustic signature is investigated deeply and systematically. Based on these analysis, several leak detection modules or robots are proposed and tested. MIT MRL proposed an acoustics sensing robot in 2011 moving along the pipe system. And they also demonstrates that a “power metric” of the signal is a good indicator to trigger the leak alarm when compared with the reference signal without leaks after careful calibration [36]. SmartBall is another good example of such robots, which is already successfully commercialized. It is a passive robot driven by water flow and works with the help of acoustic sensors placed on the spherical body of the robot without service interruption. And it achieves a sensibility of 0.028 gallons per minute with a localization accuracy of 1.8 m [37].

However, the acoustics method face a big problem and challenge when used in plastic pipes where the signal-to-noise ratio can be dominant. And the acoustic signal is attenuated greatly within plastics material due to its damping. This acoustics method can be futile if the system contains a high ratio of plastic pipes.

B.1.2 Pressure Gradient Sensing

Given the material limitation of acoustics method, pressure gradient method becomes more and more popular and attracts lots of focus. A sensor developed by MIT MRL converts the pressure gradient into tensile force, and is very sensitive to the pressure gradient caused by the leaks [38]. And this kind of sensors is already installed on a soft body robot, which is also driven by water flow. This assembled robot successfully detected leaks in various lab and field tests. The sensor has the ability to work regardless of the pipe material since the pressure gradient is inherent of leaks.

B.1.3 Some Other Methods

Besides the above methods, GPR (Ground Penetrating Radar) [39], fiber optic sensing [40], or FSR sensor (Force Sensitive Resistor) [6] can also be used to monitor the health

condition of the pipeline. But they all have some problems to make them practical in a real scenario. The GPR method highly depends on the soil condition and depth of the pipes. Fiber optic sensing faces a really high cost to construct and maintain, while FSR suffers from a very low sensibility and sensitivity.

B.2 Problem Description

Previously, a new leak sensor has been developed and installed on a soft body robot by MIT MRL. The sensor with a rough surface is placed very close to the wall. And once there is a leak and thereby low-pressure region, the sensor can be stuck to the rough wall by the huge suction force. And then the big sensor will be stretched by the relative motion between the robot body and the membrane sensor. This deformation and tensile force can be collected by the conductive rubber and recorded by the micro-controller. The existence of the low pressure region, but with high pressure gradient, is validated by CFD simulation, and the result is shown in Fig. B-1.

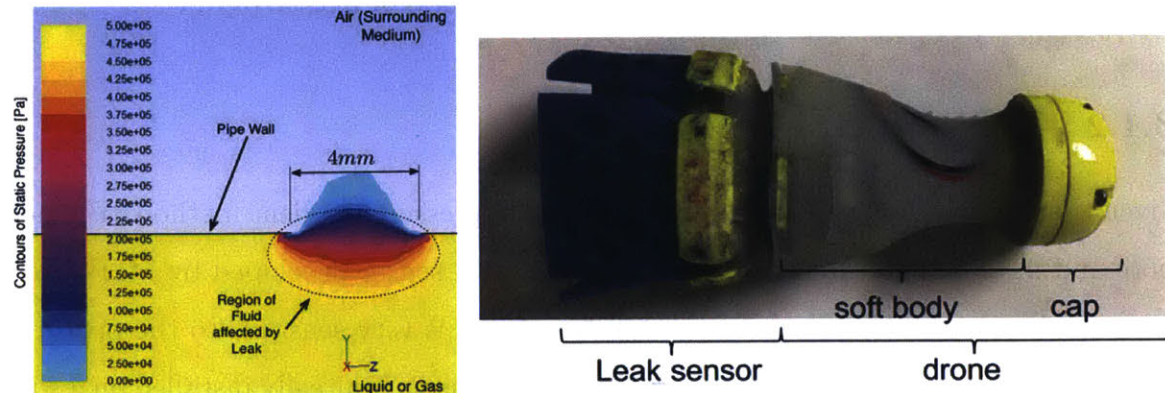


Figure B-1: Working principle and prototype of previously designed leak detection robot [38].

This robot design uses the pressure gradient method to eliminate the material limitation of the pipeline. And it also has the advantage of high sensitivity, low cost and high maneuverability. However, it also faces the following problems in practical lab and field test:

- 1) The low-pressure region is very small and very close to the pipe wall. As is

shown in Figure B-1, the distance between the pipe wall and the farthest point of low-pressure region caused by a 4 mm leak is only about 1 mm. This requires the sensor to be placed very close to the pipe wall.

2) Since the sensor is very close to the wall, it is difficult to avoid the noise caused by the attachment on the pipe and near-wall turbulence. Although the neutral surface of the sensor is specially designed so that the sensor can only bend to one direction theoretically, it is still hard to distinguish the leak signal and false alarm caused by the pipe tubercles under some extreme circumstances.

Thus, it is strongly demanded that we can find a new method to relocate the low-pressure region to somewhere else the sensor will not be influenced by the near wall effect and tubercles. Moreover, if the area of the low-pressure region can be magnified, it will be easier to place the sensors. In this chapter, a new concept with micro flow channels is proposed and validated with CFD simulation, and a concept design is also prototyped.

B.3 Theoretical Analysis

The static pressure of one point within flow is dominated by the Bernoulli equation that

$$p + \frac{1}{2}\rho V^2 + \rho gh = const \quad (B.1)$$

where p is the pressure, ρ is the density, V is the velocity, h is elevation and g is the gravitational acceleration. This equation describes the pressure head distribution on a single streamline with constant density and steady flow. And it also shows the possibility to obtain the desired pressure distribution with a proper design of the channel geometry. High flow velocity always corresponds to low static pressure. And the flow velocity is generally dominated by mass conservation, where the flow will speed up if the size of the water flow channel is narrowed down.

Based on the above analysis, a concept of the vertical micro flow channel is proposed. One end of the channel is placed inside the possible low-pressure region. And

once the channel encounters a leak, the flow running outside through the leak will be guided inside the flow channel. Since the size of the flow channel is relatively small, the flow in the channel will be speeded up and the static pressure will drop dramatically according to the Bernoulli equation. According to mass conservation principle, the flow velocity within the channel and the thereby static pressure should be relatively consistent, which means that the low-pressure region is guided to the other end of the channel, which is far away from the leak. And the channel also provides large space and high flexibility for us to place the sensor.

B.4 Numerical Simulation and Validation

Systematic 2D numerical simulation is conducted first to validate the idea. The simulation is performed on the platform of ANSYS with the Fluent module. The 2D setup dramatically simplifies the simulation and reduces the consumption of the computational power, and it also provides more generic results and demonstration. The simulation setup is shown in Figure B-2. The total computational region has a length of 2 m to allow the flow to fully develop after the entrance and after the leak, and a 0.051 m height to simulate the 2-inch pipe cross-section. The mesh is specifically refined near the pipe walls and the channel walls to capture more near wall characteristics and avoid unnatural turbulence dissipation. In all the simulation cases, the inlet is set to be pressure inlet with a 10,000 Pa fixed pressure, while the leak and the pipe outlet is set to be pressure outlet with 0 Pa fixed pressure, which is the gauge pressure in real experiments.

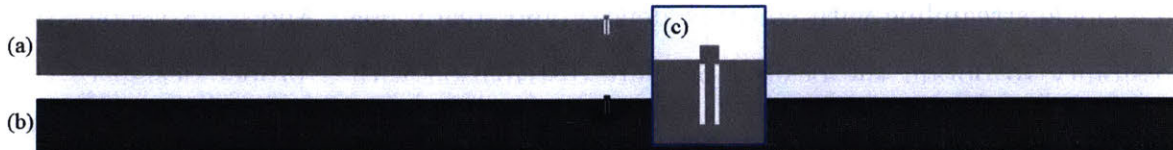


Figure B-2: Simulation setup. (a) geometry setup. (b) mesh setup and refinement. (c) geometry zoom-in at the leak and the channel.

In this section, factors, including the distance between the channel and the pipe

wall, the channel size, position of the channel relative to the leak, and the orientation angle of the channel, will all be discussed systematically.

B.4.1 Concept validation

To validate the theoretical analysis and the effect of the channel, a comparison simulation of two cases, with or without the channel respectively, is carried out. In these two cases, the leak is set to be 4 mm.

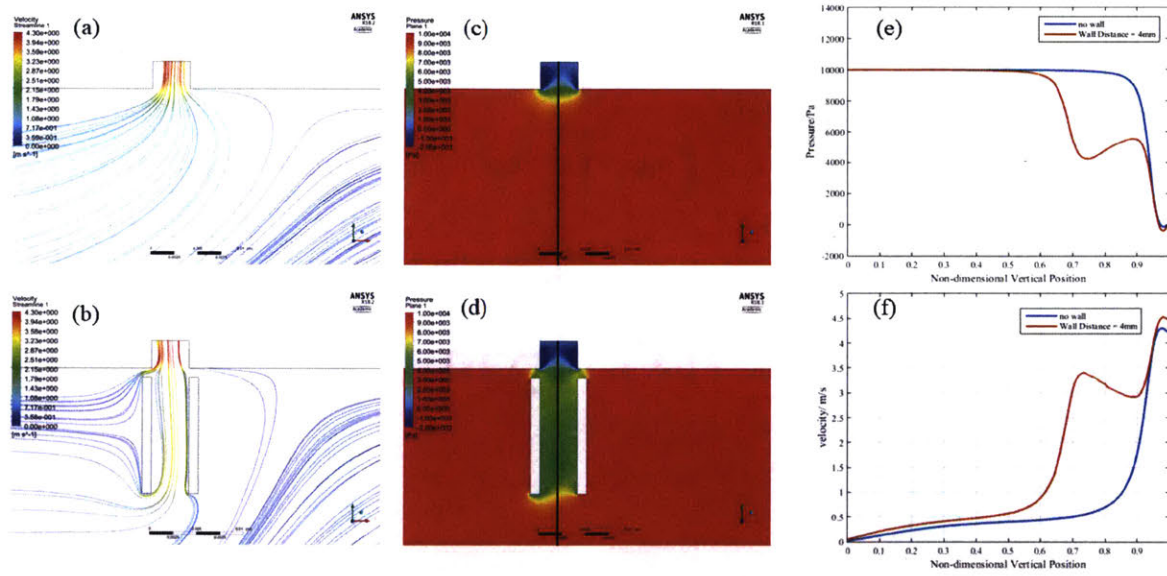


Figure B-3: Simulation result for validation. (a) streamline without channel. (b) streamline with channel. (c) pressure contour without channel. (d) pressure contour with channel. (e) pressure distribution along the center line of the channel. (f) velocity distribution along the center line of the channel.

During the simulations, pressure and velocity data along the center line (the black lines in the Figure B-3) are extracted and plotted in Figure B-3 (e) and (f). According to the simulation results, it is clearly shown that the streamlines are gathered at the leak from all the directions in the case without the channel, while the streamlines are most guided into the channel with the channel, although some streamlines go through the gap between the channel and the wall. In the pressure contour, the results are the same as the predicted ones that the pressure within the channel is much lower than its surrounding, and the low pressure spreads everywhere within the channel. And the

difference is more obvious when observing in Figure B-3 (e) and (f), where the channel starts from the non-dimensional vertical position of 75%. The velocity and pressure deviation within the channel are resulted from the streamline deformation caused by the right angle of the channel. But this does not influence the final conclusion that the channel can guide the low-pressure region to a different place.

B.4.2 Gap between the channel and the wall

The first factor which may have an impact on the effect of the microchannel is the gap between the channel and the wall. If the gap is too big, then the channel will not work as a flow guide. The channel size is first set to be 4 mm and the gaps are set to be 0 mm (connected), 1 mm, and 2 mm. The results are shown in Figure B-4.

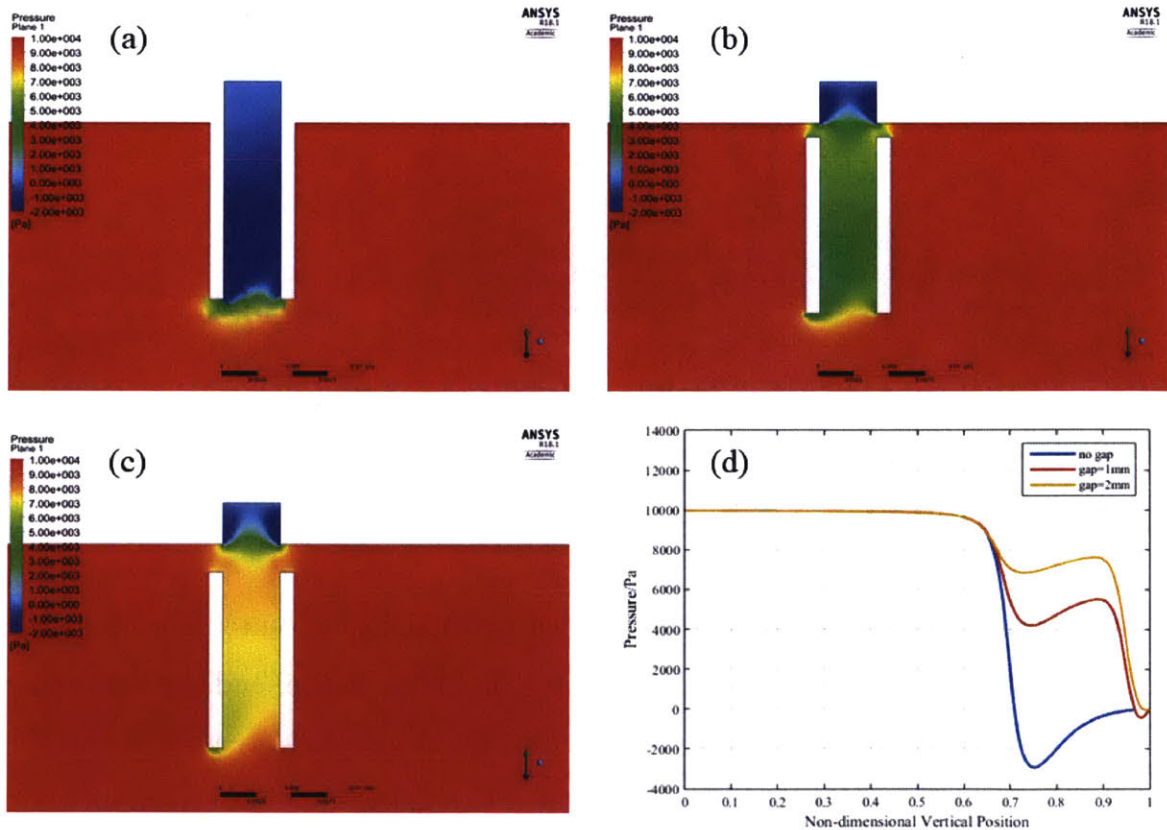


Figure B-4: 4 mm channel simulation result with various gaps. (a) no gap. (b) 1 mm gap. (c) 2 mm gap. (d) pressure distribution on the center lines of the channels.

When there is no gap, the pressure within the channel is extremely low, nearly

the same as the 0 Pa pressure outlet boundary condition. And the pressure within the channel increases with the gap, but the pressure is still much lower than the surrounding reference pressure. And the same conclusion can be easily drawn from the plot obviously. The simulation results with different channel sizes of 2 mm and 8 mm are shown in Figure B-5.

From the above results, all the cases show a quite similar trend that the static pressure increases with the gap. But when the gap is 2 mm for the 8 mm channel, the effect of the channel is already trivial.

B.4.3 Channel size

The channel size is defined as the distance between two channel walls. And the results of the cases with a size of 2 mm, 4 mm, 8 mm, and 16 mm are shown in Figure B-6. They are all with the same gap of 1 mm.

It is clearly shown that the pressure within the channel is very similar for the 2 mm and 4 mm channel size cases. But the pressure increases with the channel size when the channel is larger than the leak, namely the 8 mm and 16 mm channel size cases. And when the channel size is 16 mm, the effect of the channel is even hard to observe. Thus a small channel is recommended to increase the sensibility and sensitivity of the channel.

B.4.4 Relative position of the channel

The above analysis requires the channel size to be very small. But sometimes, the small channel may encounter a large leak, and then whether the small channel still works is another concern in our design process. Thus, simulations with 8 mm leak and 2 mm channel are performed. In these cases, the channels are placed at different places relative to the leak. The position of the channel and the simulation results are shown in Figure B-7.

From the above results, it is demonstrated that the small channel can also work well with large leaks at different positions. Using this characteristic, the size of the

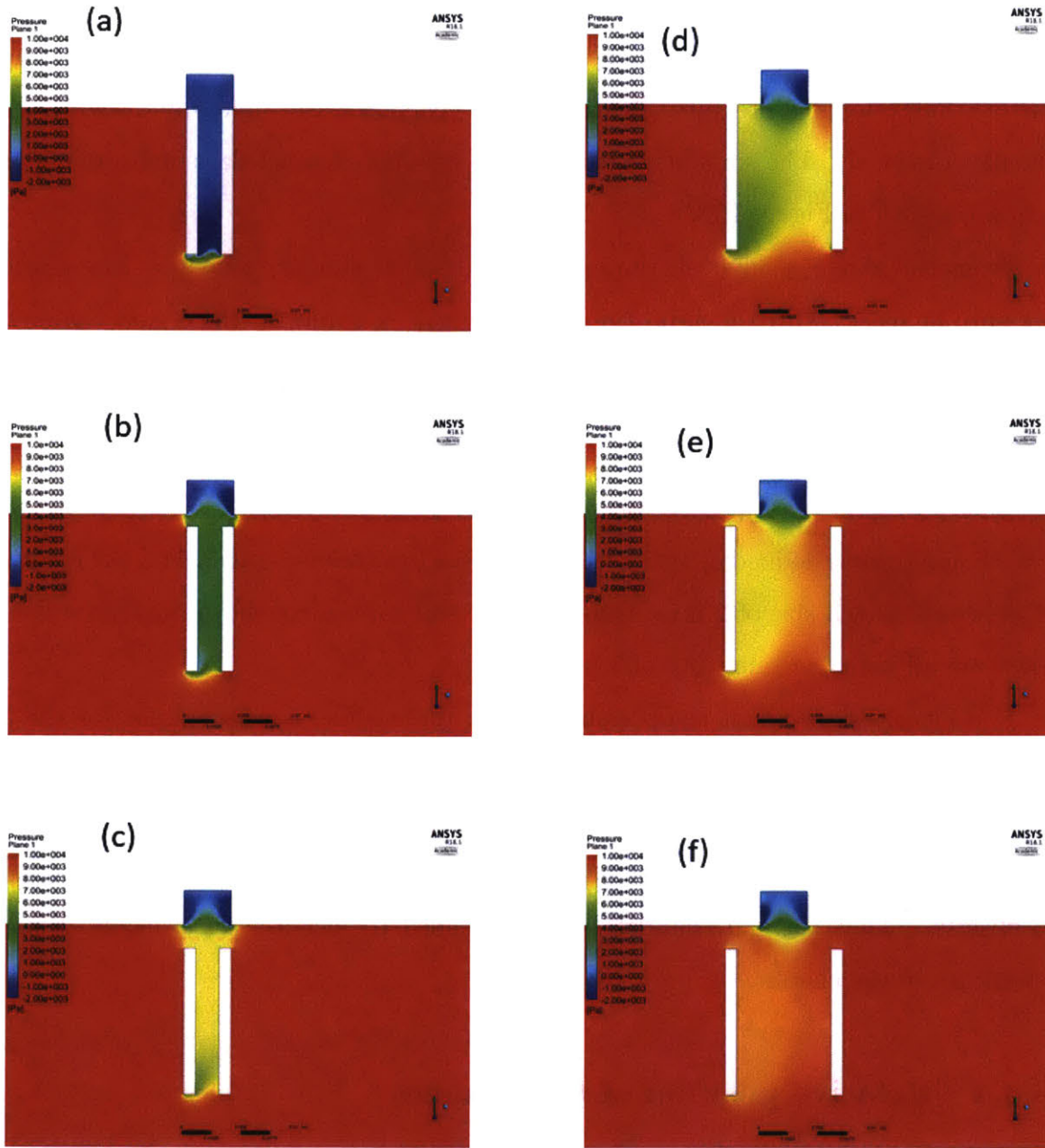


Figure B-5: 2 mm and 8 mm channel simulation result with various gaps. (a) 2 mm channel no gap . (b) 2 mm channel with 1 mm gap. (c) 2 mm channel with 2 mm gap. (d)8 mm channel with no gap. (e) 8 mm channel with 1 mm gap. (f) 8 mm channel with 2 mm gap.

leak can also be calculated with the flow pressure information recorded after careful calibration.

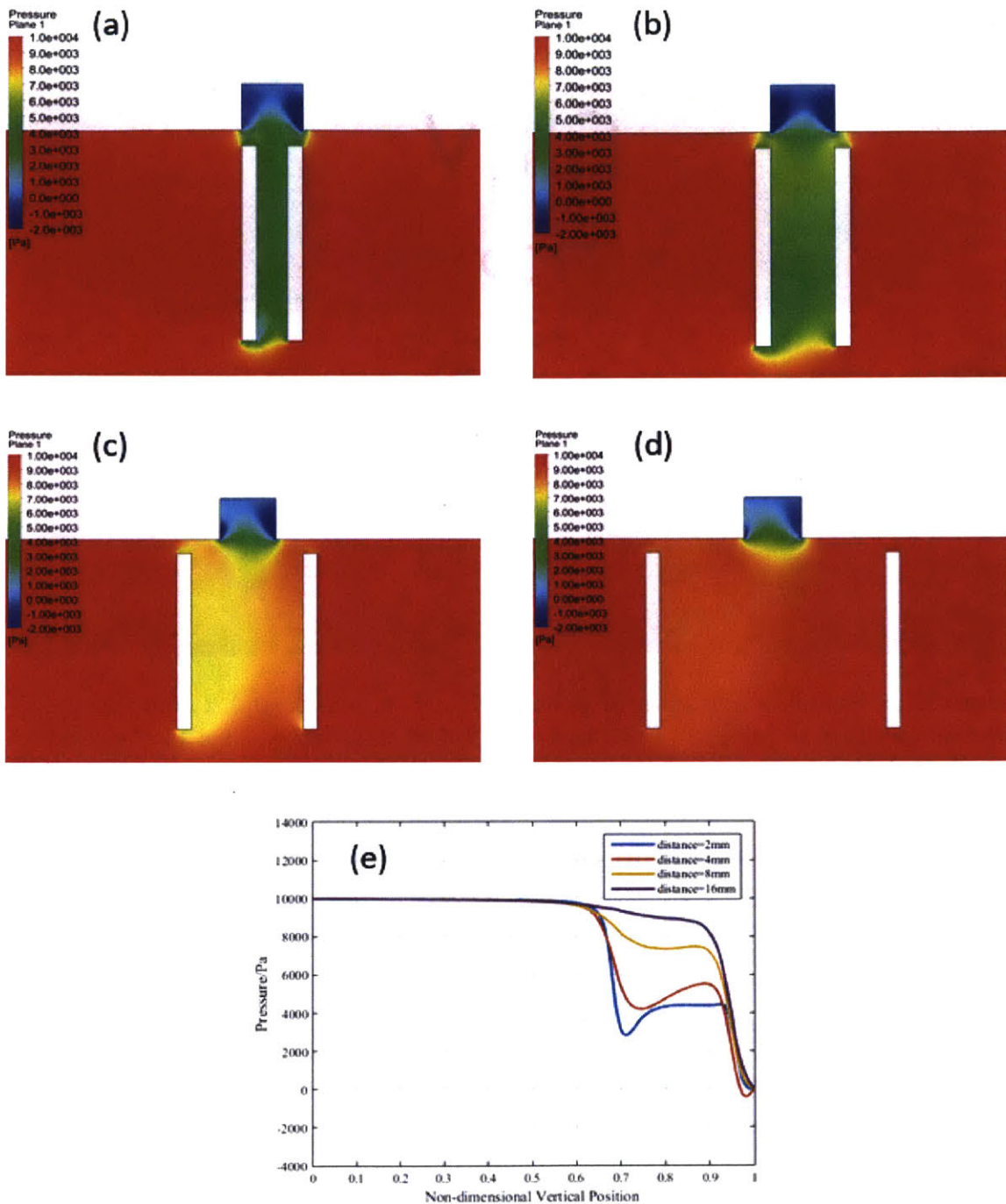


Figure B-6: 1 mm gap simulation result with various channel sizes of (a) 2 mm channel; (b) 4 mm channel; (c) 8 mm channel size; (d) 16 mm channel size. (e) plot of the pressure on center line.

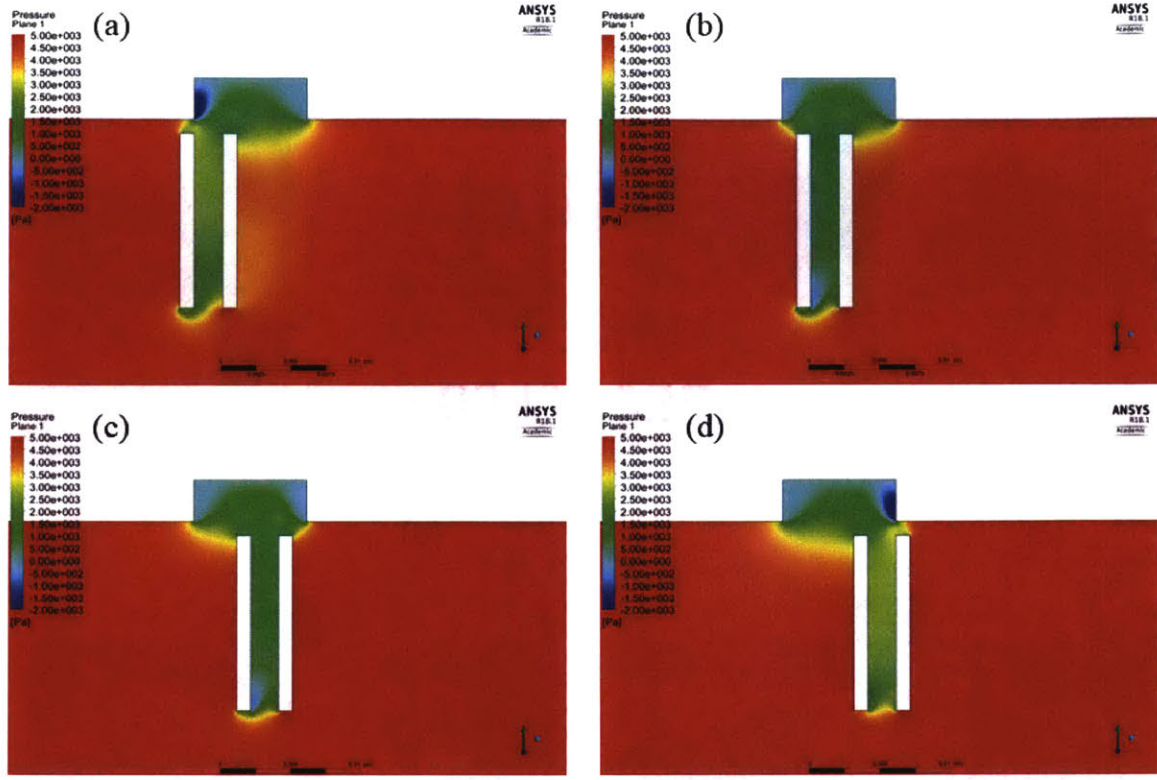


Figure B-7: Simulation results of cases with a 8 mm leak and 2 mm channel at different position of (a) 1/4 of the leak; (b) 2/4 of the leak; (c) 3/4 of the leak; (d) 4/4 of the leak.

B.4.5 Orientation angle of the channel

In the practical daily use of the leak detection sensor or robot, it is inevitable for the robot to turn at the elbow of the pipeline. Thus, in this case, it is also needed to verify that the channel can work with an orientation not vertical, but with an angle to the vertical axis. Results of cases with an 8 mm leak and a 2 mm channel with a 45° degree skewing to the right are shown in Figure B-8.

The results are quite similar to the discussion in B.4.4. Thus the effect under different orientation angles is also validated.

B.4.6 Overset moving part simulation

The effect of the channel to relocate the low-pressure region and magnify its area is already demonstrated and validated with simulations of stationary parts in the

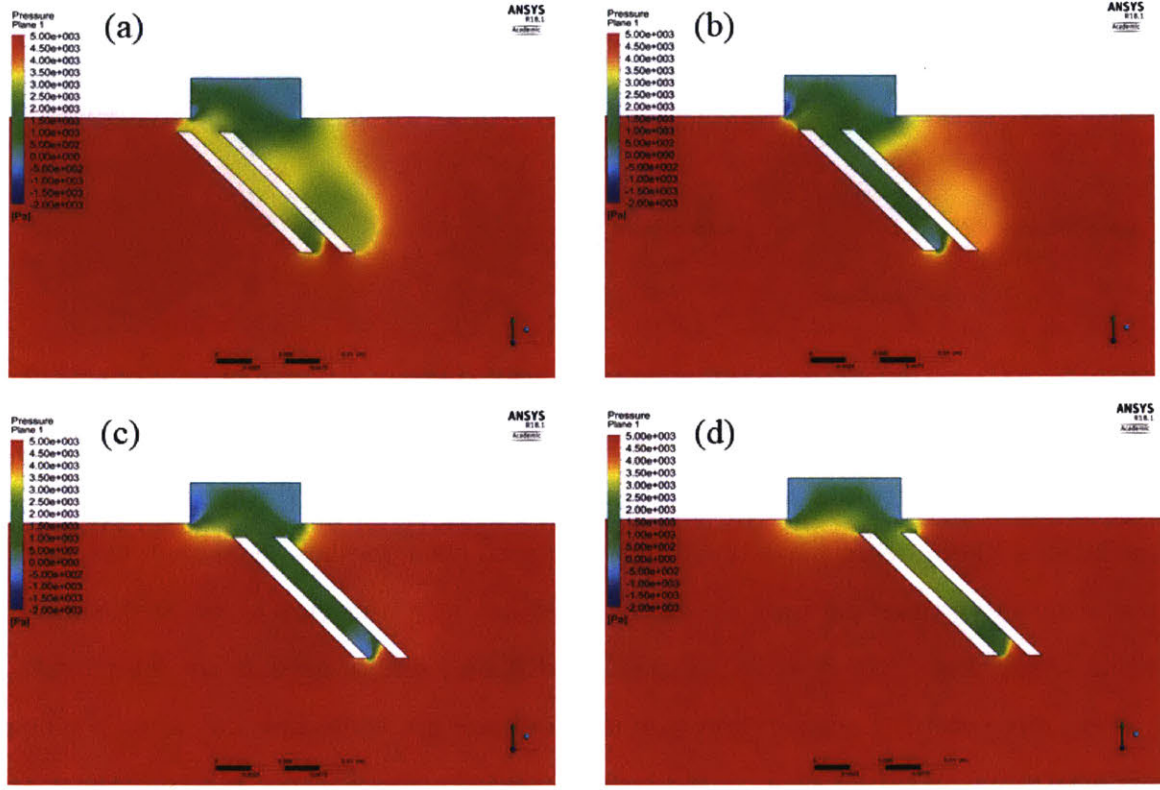


Figure B-8: Simulation results of cases with a 8 mm leak and 2 mm channel skewing 45° to the right at different position of (a) 1/4 of the leak; (b) 2/4 of the leak; (c) 3/4 of the leak; (d) 4/4 of the leak.

above subsections. But if the robot starts to move, the problem can be much more complicated, as water with inertia needs times to react to the suction force at the leak. In this case, the results can be different or the effect of the channel may be weakened. Thus it is necessary to conduct simulations with moving parts and discuss the results of these cases. There are several methods, which are capable to simulate moving parts, including Dynamic Mesh Method, Sliding Mesh Technique, Immersed Boundary Method, Meshless Particle Method, and Overset Mesh Method. The large translational moving range of the channel makes the Overset Mesh Method the most applicable in our application. The working principle of the Overset Mesh Method is illustrated in the below figure.

In the Overset Mesh Method, several sets of meshes are established for different parts of the bodies with relative motion. In the above demonstration, two sets

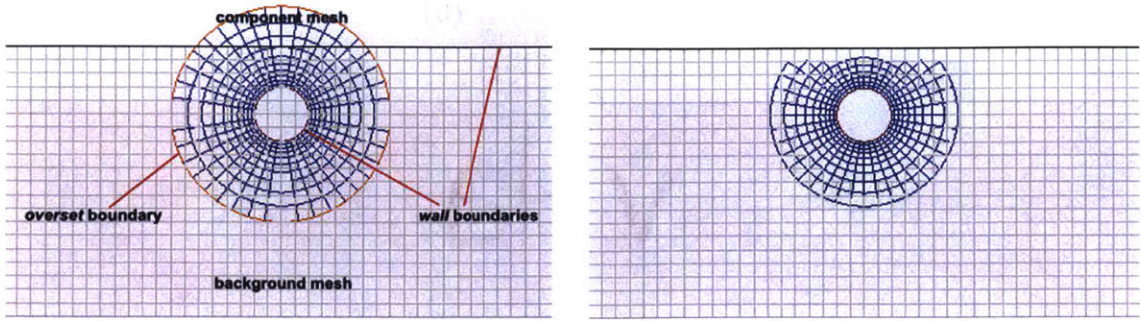


Figure B-9: Working Principle of the Overset Mesh Method.

of meshes for background and the moving circle are established separately. During simulations, the moving parts move together with their meshes. And then the background mesh and moving meshes are trimmed at every time step to fit the geometry layout. And finally, the flow information in different sets of meshes are interpolated at every time step to achieve flow connection among the meshes and form a whole flow map.

Overset Mesh Method embedded in the ANSYS Fluent R19.0 is adopted in our investigation and the moving channel is set to move at a fixed speed of 0.4 m/s. The results are shown in Figure B-10.

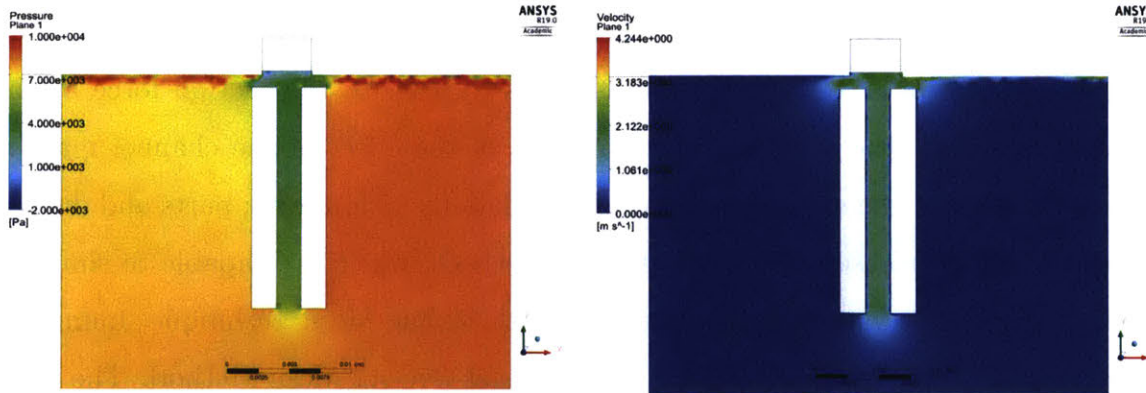


Figure B-10: Simulation results of moving channels using Overset Mesh Method.

The pressure and velocity contours are pretty similar to the cases with stationary channels. The pressure in the channel is much lower and the velocity of the flow is much higher. Thus the effect of the microchannels is finally validated.

However, it is also found that, with moving channels, the pressure after the channel is higher than the one before, which is caused by the pushing of the channel wall. And more turbulence near the pipe wall is observed.

B.5 Conceptual Design

With the effect validation of the microchannel, designs can be proposed based on this principle. The easiest way is to design a cylinder with microchannels mounted on its surface. And the pressure sensors can be placed in every channel to detect the pressure change. But this design has to tackle problems of the large number of channels and pressure sensors. And it is also very hard to place the sensors in such a micro-size channel. Furthermore, the channel also tends to vanish if the channel is very long.

Thus the vertical channels are changed into horizontal channels, which is formed naturally between the robot body and the pipe wall. The proposed conceptual design is illustrated in Figure B-11.

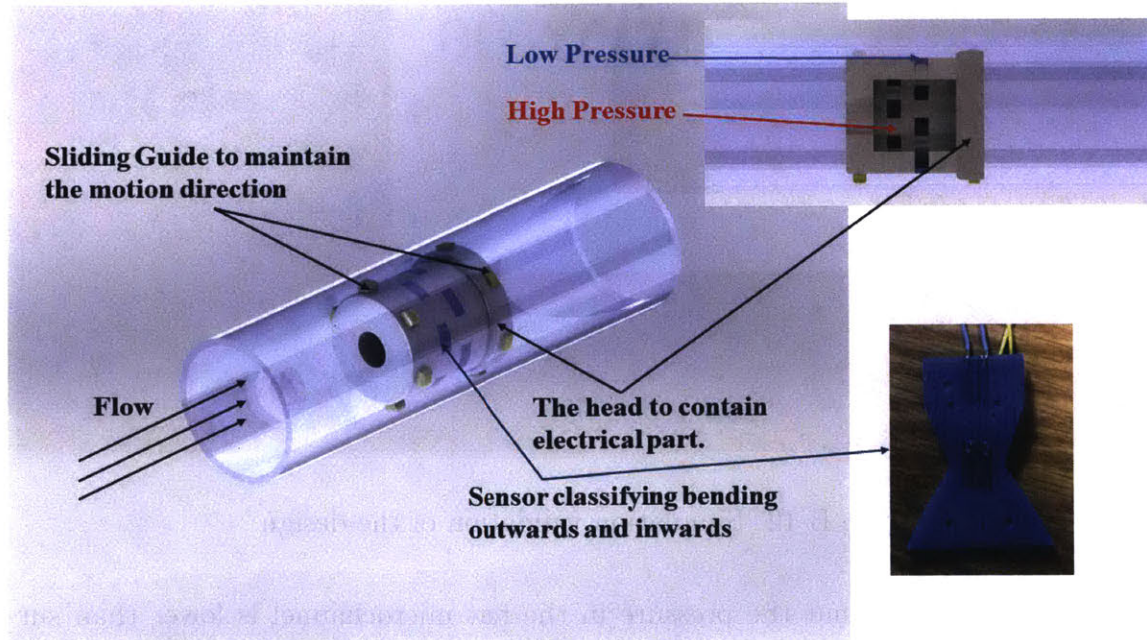


Figure B-11: Proposed conceptual design.

In this design, the robot is propelled by the water pressure behind. Thus the water

pressure within the robot is relatively high. When the robot encounters a leak, all the flow moving outside the leak are guided into the flat channel between the robot body and the pipe wall, where a region with high flow velocity and low pressure will be formed. And then the blue sensors for force sensing, bending sensing, or pressure sensing can function and record the flow condition change caused by the leak. The yellow part is made of plastics, working as a sliding guide to maintain the motion direction of the robot.

Since the channel direction is changed, a new simulation demonstration with this specific design is established and the results are shown in Figure B-12.

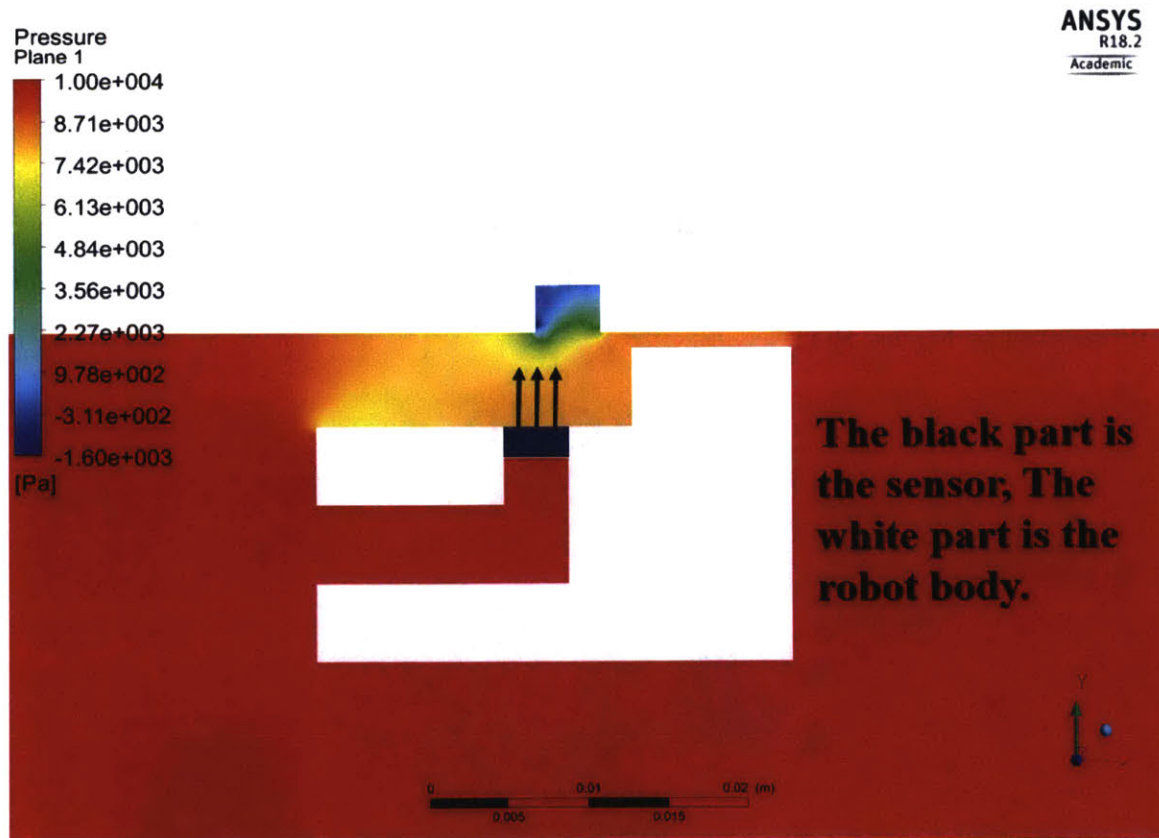


Figure B-12: Simulation validation of the design

It is clearly shown that the pressure in the flat microchannel is lower than surrounding, even though the channel size is relatively large. The large distance between the sensor and the pipe wall can eliminate most of the noise caused by the pipe wall tubercles and turbulence. Furthermore, the lift force coefficient acting on the blue

sensor can reach up to 12.41, which dramatically increases the sensitivity of the channel sensor.

B.6 Problems of the Design

Although the microchannel effect is validated in simulation, the concept still has a long way to go before practice.

- 1) This concept requires a huge number of sensors and channels to fully cover the pipe perimeter. It raises the high requirement for the fabrication process.
- 2) Signal from so many sensors requires a new algorithm to determine and localize the leak.
- 3) When the channel size is small, surface tension can become dominant, which requires special consideration on the structural design.

B.7 Summary

In this chapter, the concept of a micro flow channel is proposed to relocate the low-pressure region and magnify its area. The feasibility of the concept is validated with both theoretical analysis and CFD simulation for both stationary channels and moving channels. It is found that the channel works well under severe circumstances, like large-size leaks, or skewness of the channel to one direction. But it requires that the channel size should be comparable to or smaller than the leak, which is desired to be detected. After the validation, a conceptual design is proposed. Its effect and problems are also further discussed.

Appendix C

Materials and Components

C.1 Conductive Coating

Some properties of the conductive coating materials related to the design are listed in Table C.1 for the silver coating, Table C.2 for the nickel coating, and Table C.3 for the carbon coating respectively.

Table C.1: Properties of the silver conductive coating material [41].

Properties	Method	Value
Vendor		MG Chemicals
Model number		842AR-15ML
Touch dry or recoat time		3 min
Full cure at 22°C		24 h
Life		3 y
Constant service temperature		-40°C-120°C
Conductivity	Method 5011.5 in MIL-STD-883H	9337 S/cm
Relative permeability		<1.0
Color		Light grey
Water resistance		Yes
Adhesion on ABS	ASTM D 3359	5B

Table C.2: Properties of the nickle conductive coating material [42].

Properties	Method	Value
Vendor		MG Chemicals
Model number		841WB-15ML
Touch dry or recoat time		30 min
Full cure at 22°C		24 h
Life		2 y
Constant service temperature		-40°C-120°C
Conductivity	Method 5011.5 in MIL-STD-883H	37 S/cm
Relative permeability		≥100
Color		Grey
Water resistance		Yes
Adhesion on ABS	ASTM D 3359	5B

Table C.3: Properties of the carbon conductive coating material [43].

Properties	Method	Value
Vendor		MG Chemicals
Model number		838AR-15ML
Touch dry or recoat time		3 min
Full cure at 22°C		24 h
Life		3 y
Constant service temperature		-40°C-120°C
Conductivity	Method 5011.5 in MIL-STD-883H	3.1 S/cm
Relative permeability		<1.0
Color		Black
Water resistance		Yes
Adhesion on ABS	ASTM D 3359	5B

C.2 Smooth-on XTC-3D Coating

Some properties of the Smooth-on XTC-3D coating used in the design to reduce the friction of the channel walls are listed in Table C.4.

Table C.4: Properties of the Smooth-on XTC-3D coating material [44].

Properties	Value
Vendor	Smooth-On, Inc.
Model number	XTC-3D
Cure time in thin layer	3.5 hours
Color	Clear
Shore D hardness (ASTM D2240)	80D

Bibliography

- [1] Roland Liemberger, Philippe Marin, et al. The challenge of reducing non-revenue water in developing countries—how the private sector can help: A look at performance-based service contracting. 2006.
- [2] What is non-revenue water? how can we reduce it for better water service?
<https://blogs.worldbank.org/water/what-non-revenue-water-how-can-we-reduce-it-better-water-service>. [Online; accessed 16-May-2019].
- [3] ASCE. 2017 infrastructure report card. ASCE Reston, VA, 2017.
- [4] Masanobu Shinozuka, Pai H Chou, Sehwan Kim, Hong Rok Kim, Eunbae Yoon, Hadil Mustafa, Debasis Karmakar, and Selim Pul. Nondestructive monitoring of a pipe network using a mems-based wireless network. In *Nondestructive Characterization for Composite Materials, Aerospace Engineering, Civil Infrastructure, and Homeland Security 2010*, volume 7649, page 76490P. International Society for Optics and Photonics, 2010.
- [5] Nicole Metje, David N Chapman, David Cheneler, Michael Ward, and Andrew M Thomas. Smart pipes—instrumented water pipes, can this be made a reality? *Sensors*, 11(8):7455–7475, 2011.
- [6] Ali Sadeghioon, Nicole Metje, David Chapman, and Carl Anthony. Smartpipes: smart wireless sensor networks for leak detection in water pipelines. *Journal of sensor and Actuator Networks*, 3(1):64–78, 2014.
- [7] D Hoffmann, A Willmann, R Göpfert, P Becker, B Folkmer, and Y Manoli. Energy harvesting from fluid flow in water pipelines for smart metering applications. In *Journal of Physics: Conference Series*, volume 476, page 012104. IOP Publishing, 2013.
- [8] Marco Casini. Harvesting energy from in-pipe hydro systems at urban and building scale. *International Journal of Smart Grid and Clean Energy*, 4(4):316–327, 2015.
- [9] Steve P Beeby, RN Torah, MJ Tudor, P Glynne-Jones, T O'donnell, CR Saha, and S Roy. A micro electromagnetic generator for vibration energy harvesting. *Journal of Micromechanics and microengineering*, 17(7):1257, 2007.

- [10] Peter Glynne-Jones, Michael John Tudor, Stephen Paul Beeby, and Neil M White. An electromagnetic, vibration-powered generator for intelligent sensor systems. *Sensors and Actuators A: Physical*, 110(1-3):344–349, 2004.
- [11] CR Saha, T OâŽdonnell, N Wang, and P McCloskey. Electromagnetic generator for harvesting energy from human motion. *Sensors and Actuators A: Physical*, 147(1):248–253, 2008.
- [12] Kenneth A Cunefare, EA Skow, Alper Erturk, J Savor, N Verma, and MR Cacan. Energy harvesting from hydraulic pressure fluctuations. *Smart Materials and Structures*, 22(2):025036, 2013.
- [13] JJ Allen and AJ Smits. Energy harvesting eel. *Journal of fluids and structures*, 15(3-4):629–640, 2001.
- [14] George W Taylor, Joseph R Burns, SA Kammann, William B Powers, and Thomas R Welsh. The energy harvesting eel: a small subsurface ocean/river power generator. *IEEE journal of oceanic engineering*, 26(4):539–547, 2001.
- [15] Morton Mitchner and Charles H Kruger Jr. Partially ionized gases. 1973.
- [16] S al Way, SM DeCorso, RL Hundstad, GA Kemeny, W Stewart, and WE Young. Experiments with mhd power generation. *Journal of Engineering for Power*, 83(4):397–408, 1961.
- [17] R.E. Weistein and R.B. Boulay. 1000 mwe advanced coal-fired mhd/steam binary cycle power plant conceptual design. Technical Report 1989-EJ2738, 1989.
- [18] David Cébron, Sylvain Viroulet, Jérémie Vidal, Jean-Paul Masson, and Philippe Viroulet. Experimental and theoretical study of magnetohydrodynamic ship models. *PloS one*, 12(6):e0178599, 2017.
- [19] LG Yan, CW Sha, K Zhou, Y Peng, AH Yang, and JQ Qin. Progress of the mhd ship propulsion project in china. *IEEE transactions on applied superconductivity*, 10(1):951–954, 2000.
- [20] Wikipedia contributors. Permeability (electromagnetism) — Wikipedia, the free encyclopedia, 2019. [Online; accessed 16-May-2019].
- [21] Barmesa ia3h-40-2 opd end-suction centrifugal pump 40 hp 3ph.
<https://www.rcworst.com/Barmesa-IA3H-40-2-OPD-End-Suction-Centrifugal-Pump-40-HP-3PH-p12882.html>. [Online; accessed 16-May-2019].
- [22] H Herwig, D Gloss, and T Wenterodt. A new approach to understanding and modelling the influence of wall roughness on friction factors for pipe and channel flows. *Journal of Fluid Mechanics*, 613:35–53, 2008.

- [23] Yan Yu, Hyunwoo Yuk, German A Parada, You Wu, Xinyue Liu, Christoph S Nabzdyk, Kamal Youcef-Toumi, Jianfeng Zang, and Xuanhe Zhao. Multifunctional hydrogel skins on diverse polymers with arbitrary shapes. *Advanced Materials*, 31(7):1807101, 2019.
- [24] Changsheng Ai, Honghua Zhao, Ruijian Ma, and Xueren Dong. Pipeline damage and leak detection based on sound spectrum lpcc and hmm. In *Sixth International Conference on Intelligent Systems Design and Applications*, volume 1, pages 829–833. IEEE, 2006.
- [25] Marlene Daneti. A practical preprocessing treatment for pipeline leak locating improving. In *2008 IEEE International Conference on Emerging Technologies and Factory Automation*, pages 9–12. IEEE, 2008.
- [26] Bui Van Hieu, Seunghwan Choi, Young Uk Kim, Youngsuk Park, and Taikyeong Jeong. Wireless transmission of acoustic emission signals for real-time monitoring of leakage in underground pipes. *KSCE Journal of Civil Engineering*, 15(5):805, 2011.
- [27] Zhan-Hui Liu, Xiao-Dong Niu, Guang-Yu Mu, Xin Wang, Hong Zhang, and Yun-Jie Pang. Method for acoustic leak detection of fast reactor steam generator using maximum modulus based on wavelet transform. In *2005 International Conference on Machine Learning and Cybernetics*, volume 2, pages 737–741. IEEE, 2005.
- [28] Liu Na and Zhao Yanyan. Application of wavelet packet and support vector machine to leak detection in pipeline. In *2008 ISECS International Colloquium on Computing, Communication, Control, and Management*, volume 1, pages 66–69. IEEE, 2008.
- [29] Huali Chen, Hao Ye, LV Chen, and Hongyu Su. Application of support vector machine learning to leak detection and location in pipelines. In *Proceedings of the 21st IEEE Instrumentation and Measurement Technology Conference (IEEE Cat. No. 04CH37510)*, volume 3, pages 2273–2277. IEEE, 2004.
- [30] Danial Waleed, Syed Hamdan Mustafa, Shayok Mukhopadhyay, Mamoun F Abdel-Hafez, Mohammad Abdel Kareem Jaradat, Kevin Rose Dias, Fahad Arif, and Jawwad Imtiaz Ahmed. An in-pipe leak detection robot with a neural-network-based leak verification system. *IEEE Sensors Journal*, 19(3):1153–1165, 2018.
- [31] Jiao Yang, Yang Qingxin, Li Guanghai, and Zhang Jingyan. Acoustic emission source identification technique for buried gas pipeline leak. In *2006 9th International Conference on Control, Automation, Robotics and Vision*, pages 1–5. IEEE, 2006.
- [32] HV Fuchs and R Riehle. Ten years of experience with leak detection by acoustic signal analysis. *Applied acoustics*, 33(1):1–19, 1991.

- [33] Charles Knapp and Glifford Carter. The generalized correlation method for estimation of time delay. *IEEE transactions on acoustics, speech, and signal processing*, 24(4):320–327, 1976.
- [34] Jinghui Xu, Kevin Tshun-Chuan Chai, Guoqiang Wu, Beibei Han, Eva Leong-Ching Wai, Wei Li, Jason Yeo, Edwin Nijhof, and Yuandong Gu. Low cost, tiny sized mems hydrophone sensor for water pipeline leak detection. *IEEE Transactions on Industrial Electronics*, 2018.
- [35] YA Khulief, A Khalifa, R Ben Mansour, and MA Habib. Acoustic detection of leaks in water pipelines using measurements inside pipe. *Journal of Pipeline Systems Engineering and Practice*, 3(2):47–54, 2011.
- [36] Dimitris M Chatzigeorgiou, Atia E Khalifa, Kamal Youcef-Toumi, and Rached Ben-Mansour. An in-pipe leak detection sensor: Sensing capabilities and evaluation. In *ASME 2011 International Design Engineering Technical Conferences and Computers and Information in Engineering Conference*, pages 481–489. American Society of Mechanical Engineers, 2011.
- [37] Richard Fletcher and Muthu Chandrasekaran. Smartballâ€: a new approach in pipeline leak detection. In *2008 7th International Pipeline Conference*, pages 117–133. American Society of Mechanical Engineers, 2008.
- [38] You Wu, Kristina Kim, Michael Finn Henry, and Kamal Youcef-Toumi. Design of a leak sensor for operating water pipe systems. In *2017 IEEE/RSJ International Conference on Intelligent Robots and Systems (IROS)*, pages 6075–6082. IEEE, 2017.
- [39] Mansor Nakhkash and Mohammad R Mahmood-Zadeh. Water leak detection using ground penetrating radar. In *Proceedings of the Tenth International Conference on Grounds Penetrating Radar, 2004. GPR 2004.*, pages 525–528. IEEE, 2004.
- [40] Marc Nikles. Long-distance fiber optic sensing solutions for pipeline leakage, intrusion, and ground movement detection. In *Fiber optic sensors and applications VI*, volume 7316, page 731602. International Society for Optics and Photonics, 2009.
- [41] MG Chemicals. *Silver Conductive Print*, 2 2019. Ver. 1.00.
- [42] MG Chemicals. *Super Shield Water Based Nickel Conductive Coating*, 1 2019. Ver. 3.00.
- [43] MG Chemicals. *Total Ground Carbon Conductive Coating*, 11 2018. Ver. 3.00.
- [44] Smooth-On, Inc. *XTC-3D High Performance 3D Print Coating*.